Hybrid Semiconductor Detectors for High Spatial Resolution Phase-contrast X-ray Imaging

by

Christopher Charles Scott

A thesis
presented to the University of Waterloo
in fulfillment of the
thesis requirement for the degree of
Doctor of Philosophy
in
Electrical and Computer Engineering

Waterloo, Ontario, Canada, 2019

Examining Committee Membership

The following served on the Examining Committee for this thesis. The decision of the Examining Committee is by majority vote.

External Examiner:	Alessandro Olivo Professor, Dept. of Medical Physics and Biomedical Engineering, University College London
Supervisor:	Karim S. Karim Professor, Dept. of Electrical and Computer Engineering, University of Waterloo
Internal Member:	Peter M. Levine Associate Professor, Dept. of Electrical and Computer Engineering, University of Waterloo
Internal Member:	Simarjeet Saini Associate Professor, Dept. of Electrical and Computer Engineering, University of Waterloo
Internal-External Member:	Alexander Wong Associate Professor, Dept. of System Design Engineering, University of Waterloo

Author's Declaration

I hereby declare that I am the sole author of this thesis. This is a true copy of the thesis, including any required final revisions, as accepted by my examiners.

I understand that my thesis may be made electronically available to the public.

Abstract

When conventional x-ray radiography presents inadequate absorption-contrast, higher sensitivity can be achieved using phase-contrast methods. The implementation of phase-contrast x-ray imaging using propagation-based techniques requires stringent spatial resolution requirements that necessitate lengthy propagation distances and thin (and hence low detection efficiency) scintillator-based detectors. Thus, imaging throughput is limited, and the absorbed dose in the sample can be unacceptable for radiation sensitive life science and biomedical applications.

This work develops hybrid amorphous selenium and complementary metal-oxide-semiconductor detectors with a unique combination of high spatial resolution and detection efficiency for hard x-rays. A semiconductor fabrication process was developed for large-area compatible vertical detector integration by back-end processing. Characterization of signal and noise performance using Fourier-based methods was performed by modulation transfer function, noise power spectrum, and detective quantum efficiency experiments using radiography and microfocus x-ray sources.

The measured spatial resolution at each stage of detector development was one of the highest, if not *the* highest reported for hard x-rays. In fact, charge carrier spreading from x-ray interactions with amorphous selenium was shown physically larger than the pixel pitch for the first time. A simultaneous factor of four improvement in detection efficiency compared to thin gadolinium oxysulfide-based scintillator detectors was also achieved, despite the detector being a relatively unoptimized prototype.

Fast propagation-based phase-contrast x-ray imaging in compact geometries is demonstrated using a conventional microfocus source. This simple implementation of the phase-contrast technique was applied to imaging the mouse stifle joint. Using propagation-based edge-enhancement the articular cartilage was delineated, opening the possibility of studying diseases such as osteoarthritis using a compact, relatively simple laboratory setup.

This research suggests that hybrid semiconductor technology offers the potential to fill the large performance deficit in high spatial resolution scintillator-based detectors for propagation-based phase-contrast x-ray imaging.

Acknowledgements

First and foremost, I would like to thank Dr. Karim S. Karim for his guidance, encouragement, and trust, throughout this academic endeavor.

I would like to show appreciation to my examining committee, Dr. Alessandro Olivo, Dr. Peter M. Levine, Dr. Simarjeet Saini, and Dr. Alexander Wong, for accepting to review my work. I am also highly grateful to Dr. Ian A. Cunningham who provided invaluable guidance and discussion on x-ray detector performance metrics.

I am highly indebted to my colleagues, Hummer Li, Dr. Celal Con, Alireza Parsafar, Abdollah El-Falou, Jerry Liang, and Xu Di, who supported this work. I would also like to express thanks to my senior colleagues, Dr. Nicholas Allec, Dr. Shiva Abbaszadeh, Dr. Hasib Majid, and Dr. Amir Goldan, who assisted early in this academic endeavor.

I would like to thank Richard Barber and the Giga-to-Nanoelectronics Center at the University of Waterloo. I also would like to thank the generous Rick Forgett, and the highly skilled Robert Kaptein, Fred Bakker, Charlie Boyle, Mark Kuntz, Phil Laycock, and Jorge Cruz, of the University of Waterloo Engineering Machine Shop. Finally, I would like to thank the Dr. Robin E. Duncan Lipid Enzyme Discovery Lab, in particular Dr. Maria F. Fernandes, for providing biological samples.

Collaboration with Teledyne DALSA Inc., and KA Imaging Inc. was instrumental to the success of this work.

Dedication

To my parents,

with love and gratitude.

To my grandfather,

my early mentor in mathematics and engineering.

Table of Contents

List of Tables

List of Figures

Chapter 1

Introduction

Imaging using x-ray radiation plays a significant role in many fields including medicine, industry, and fundamental research. Conventional radiography utilizes the highly penetrating nature of x-rays to study the internal composition of objects by observing absorption variations. Its utility is limited when materials are effectively non-absorbing or when absorption gradients are small, and the resulting absorption contrast is poor. Phase variations due to the object's electron density are also present in the x-ray wavefront exiting the object (described by the real part of the complex refractive index) and can be visualized using phase-contrast techniques [1, 2]. In this paradigm, objects that conventionally present little contrast (e.g. soft biological tissue or other low-density materials such as polymers) can be imaged with higher sensitivity.

Phase-contrast x-ray imaging techniques include those using specialized optical elements such as crystal analyzers [1, 3], crystal [4, 5] or grating interferometers [6], and coded-apertures [7], but can also be implemented simply by using free-space propagation [8]. If phase variations in the x-ray wavefront due to the presence of the object are permitted to propagate a sufficient distance before detection, they give rise to Fresnel diffraction fringes. The dependency of the fringes on the Laplacian of the phase front results in a characteristic edge-enhancement effect at material boundaries where the refractive index changes abruptly. The final image structure has no significant temporal coherence requirement, enabling the use of polychromatic x-ray sources. In fact, the only

requirement for edge-enhancement is sufficient transverse spatial coherence length, given by $l_t = \lambda z_1/\sigma_f$, where z_1 is the source-to-object distance, λ is the x-ray wavelength, and σ_f is the x-ray source focal spot size.

Propagation-based phase-contrast x-ray imaging has been demonstrated with monochromatic synchrotron sources [9, 10] as well as using polychromatic microfocus sources [8]. The size and cost of synchrotron facilities, and limited throughput of low power conventional microfocus sources, have constrained proliferation of the technique. High power sources such as liquid-metal jet [11] and laser-based [12] methods are being developed for this reason. Despite these potential improvements, a large propagation distance and poor detector quantum efficiency can result in an x-ray exposure to the object, e.g. in biomedical applications [13], that is unacceptably high.

Conventional high spatial resolution scintillator-based detectors with complementary metal-oxide-semiconductor (CMOS), amorphous silicon (a-Si), or charge coupled device (CCD) readout have poor absorption efficiency at high spatial resolutions due to thinning of the scintillator to minimize secondary optical scatter. There may also be losses in optical coupling and magnifying lenses. This work investigates a hybrid semiconductor detector approach by integrating amorphous selenium (a-Se) photoconductor material and a CMOS readout integrated circuit. Unlike the optical scatter in scintillators, the spread of absorbed energy from x-ray interactions in the photoconductor, and subsequent diffusion of photogenerated charge carriers during transport, does not significantly degrade spatial resolution as the photoconductor thickness is increased [14].

Photoconductive a-Se was first introduced commercially in the 1960s when Xerox developed the material for xerographic photoreceptors [15] and xeroradiography [16]. In the 1990s there was renewed interest in a-Se for digital x-ray applications [17, 18]. Compatible with direct physical vapor deposition of uniform thick layers over large area, a-Se has since been employed in commercial flat-panel detectors for clinical diagnostic x-ray imaging [19]. Flat-panel detectors perform image readout using an active matrix consisting of a two-dimensional array of a-Si thin film transistors [20] and are limited to relatively large ($\geq$50 μm) pixel sizes.

This work develops hybrid a-Se/CMOS x-ray detector prototypes ($\leq$25 μm pixel) to

take advantage of the inherent resolution of a-Se [21] and achieve a unique combination of high spatial resolution and high quantum efficiency for hard x-rays [22, 23, 24]. The most recent iteration utilizes a custom one-megapixel array at 7.8 μm pixel pitch. Signal and noise performance was characterized by measuring the modulation transfer function (MTF), Wiener noise power spectrum (NPS), and ultimately the detective quantum efficiency (DQE). These Fourier-based metrics are widely accepted as the primary measures of x-ray detector imaging performance [25, 26, 27]. The DQE describes image quality degradation not only from quantum efficiency of the detector, but also additional factors including incomplete absorption of x-ray energy, and secondary quanta such as light in a scintillator or charge carriers in a photoconductor. The relationship between x-ray interactions with a-Se and the Fourier-based metrics was investigated using cascaded-systems analysis where the detector was modeled as a cascade elementary physical processes [17, 27, 28, 29, 30].

Besides enabling a compact phase-contrast x-ray imaging system, the rapid and efficient acquisition of high spatial resolution phase-contrast data may also be applied to micro computed tomography for radiation sensitive life sciences and biomedical applications.

Thesis organization

The primary focus of this thesis is the development of high spatial resolution hybrid a-Se/CMOS detectors for application to propagation-based phase-contrast x-ray imaging. The thesis chapters are organized as follows:

- Chapter 2 provides background on fundamental x-ray interactions with matter and free-space propagation. This includes the mechanisms involved in conventional absorption-contrast imaging as well as those for phase-contrast imaging. This chapter also provides a basis for the discussion of x-ray interactions with a-Se photoconductors in Ch. 5.

- Chapter 3 provides background on x-ray imaging, including x-ray generation and detection. Conventional absorption-contrast radiography is discussed before introducing propagation-based phase-contrast.

- Chapter 4 provides background on metrics of detector performance. This includes Fourier-based metrics for spatial resolution, noise, and detection efficiency. Experimental methods for determining these metrics are verified using simulated images.

- Chapter 5 covers background on a-Se photoconductors. Properties such as x-ray sensitivity and dark current are defined. An a-Se/CMOS detector model is developed based on cascaded systems analysis.

- Chapter 6 develops the necessary CMOS back-end processing for integration with a-Se. The pixel pitch was 25 μm. Spatial resolution is characterized by measuring the MTF using a conventional radiography source. Absorption-contrast images are acquired as a qualitative demonstration of spatial resolution.

- Chapter 7 investigates the signal and noise performance of an in-house developed small-area 5.6 μm pixel pitch a-Se/CMOS detector using a radiography source. The experimental results are compared to predictions based on the cascaded systems analysis of Ch. 5. A new imaging apparatus was constructed to include a microfocus source in order to observe propagation-based edge-enhancement from simple object geometries.

- Chapter 8 investigates the current one-megapixel a-Se/CMOS detectors with 7.8 μm pixel pitch. Using the larger area than Ch. 7, the feasibility of commercialization is investigated by signal and noise analysis performed using a microfocus source. The experimental results are compared to predictions based on the cascaded systems analysis of Ch. 5. Phase-contrast images of plant seeds and the mouse stifle joint are acquired and analyzed.

- Chapter 9 provides the main conclusions and contributions of this work to x-ray detector development and phase-contrast x-ray imaging. Suggestions for future work are also discussed.

Chapter 2

X-ray Interactions and Free-space Propagation

2.1 Interactions of x-rays with matter

In the hard x-ray energy regime of 10–70 keV used in this work, x-ray photons will penetrate, scatter, or be absorbed when traversing matter. The primary interaction processes involved are the photoelectric effect, incoherent Compton scattering, and coherent Rayleigh scattering. In general, x-ray interactions can result in the local deposition of energy in the medium, as well as non-local transport of energy as scattered or fluorescent photons. The mechanisms of absorption and scattering combined cause the loss in strength of an x-ray beam as it traverses the medium.

2.1.1 Absorption-contrast

Both the photoelectric effect and Compton scattering contribute to the absorption of energy in matter. Rayleigh scattering is an elastic process where there is no exchange of energy from the photon to atomic electrons. The photoelectric effect results in the ionization of a tightly bound (inner shell) atomic electron by complete absorption of the x-ray photon,

and the subsequent production of a fluorescent photon as the atom relaxes. Compton scattering, on the other, hand causes the ionization of a quasi-free (outer shell) electron by nonelastic scattering of the x-ray photon. For an x-ray photon with energy E and a medium with effective atomic number Z, the photoelectric effect has an interaction cross section proportional to Z^3/E^3, while the Compton scattering cross-section is nearly independent of E and independent of Z (quasi-free electron).

All interaction mechanisms contribute to the removal of x-ray photons from the beam, producing *attenuation* as it passes through the medium. For a monoenergetic x-ray beam of energy E and number of photons N incident on a thin slab of material of thickness dz, the reduction in number of photons dN from the beam for a probability of attenuation per unit length α is given by $dN = -\alpha N\ dz$. Solving for a total slab thickness L and number of incident photons N_0 gives,

$$N(E) = N_0(E)e^{-\alpha(E)L}. \tag{2.1}$$

This result is often referred to as the Lambert–Beers law. The associated attenuation coefficient is given by the sum of all interaction contributions, $\alpha(E) = \tau_{pe}(E) + \sigma_C(E) + \sigma_R(E)$, including the photoelectric effect, Compton scattering, and Rayleigh scattering, respectively.

The fact that x-ray photons exchange energy in interactions with electrons of the medium is the basis of *absorption-contrast*. If a medium is comprised of materials with different density and thickness there are attenuation variations produced in the x-ray beam that can be used to generate contrast. Wilhelm Röntgen, who discovered x-rays in 1895, rapidly harnessed this phenomenon.

2.1.2 Phase-contrast

Visible light changes direction, or refracts, when passing from one transparent medium to another. This phenomenon is fundamental to the physics of lenses and is described by Snell's law where the material property, the refractive index n, is between 1.2–2. In the x-ray regime, the deviation of the refractive index from unity is due to Rayleigh scattering.

In this interaction an x-ray photon excites all electrons of an atom, opposed to individual electrons in the photoelectric effect and Compton scattering. The coherent oscillation of all electrons re-radiates a photon of the same energy in a new trajectory. X-ray photon frequencies are often above all electronic transition frequencies of the medium resulting in n being less than one. The convention is adopted where the refractive index is written in terms of the refractive index decrement δ,

$$n = 1 - \delta. \tag{2.2}$$

The small deviation of the refractive index from unity for water indicates the relatively small refraction angles of x-rays compared to visible light (Fig. 2.1). At 30 keV it is shown that $\delta \approx 10^{-7}$. Using Snell's law, the angle of refraction θ_r for a single degree of incidence $\theta_i = 1$ degree is simply $\theta_r \approx -\theta_i \delta = -10^{-7}$ degrees. This is many orders of magnitude smaller than the angular deviations of visible light, and is negative because the refractive index is less than unity.

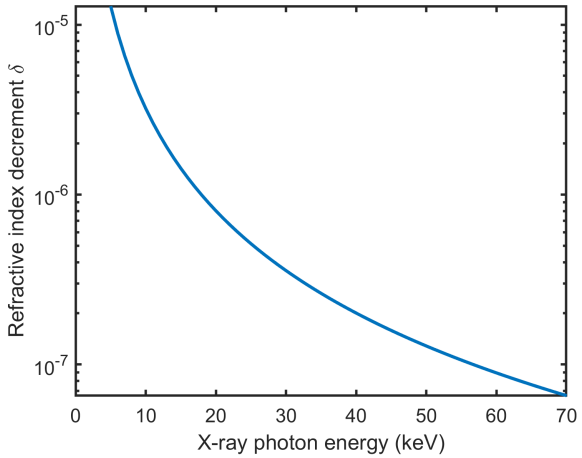

Figure 2.1: The refractive index decrement δ for water.

Phase-contrast arises as variations in refractive index and thickness of matter comprising the medium alter the shape of the beam wavefront. If the propagation direction is the z-axis, the phase shift ϕ relative to vacuum is given by,

$$\phi(x, y;\ k) = -k \int_0^L \delta(x, y; z, k)\ dz, \tag{2.3}$$

where $k = |\mathbf{k}| = 2\pi/\lambda$ is the norm of the wave vector (i.e. the wave number) for x-ray wavelength λ. The phase cannot be directly measured using a conventional x-ray detector, but instead specific phase-contrast techniques must be implemented [31, 32].

2.1.3 Complex refractive index

The attenuation and phase shift of the x-ray beam can be described using a complex-valued index of refraction n. For a homogeneous medium the index of refraction can be written in the form $n = 1 - \delta + i\beta$. The refractive index decrement is defined by [33],

$$\delta = \frac{2\pi\rho_a f^0(0) r_0}{k^2}, \tag{2.4}$$

where ρ_a is the atomic number density, $f^0(0)$ is the forward scattering factor, and $r_0 = 2.82 \times 10^{-15}$ m is the Thomas scattering length (i.e. classic electron radius). At energies sufficiently far from electron transition energies (i.e absorption edges), $f^0(0) = Z$. Now consider the plane wave $\Psi(\mathbf{r})$ at position $\mathbf{r} = (x, y, z)$ propagating through a medium with complex refractive index,

$$\Psi(\mathbf{r}) = e^{in\mathbf{k}\cdot\mathbf{r}} = e^{i(1-\delta)\mathbf{k}\cdot\mathbf{r}} e^{-\beta\mathbf{k}\cdot\mathbf{r}}. \tag{2.5}$$

If the direction of propagation is the z-axis and the plane wave is incident on the medium from vacuum, the phase shift ϕ and the attenuation of x-ray intensity I (related to the number of photons N) is given by,

$$\phi = \delta\mathbf{k}\cdot\mathbf{r} = \delta k z, \tag{2.6}$$

$$I \propto |\Psi(\mathbf{r})|^2 = e^{-2\beta k z} = e^{-\alpha z}. \tag{2.7}$$

The complex refractive index is then related to the attenuation coefficient by,

$$\beta = \frac{\alpha}{2k}. \tag{2.8}$$

2.2 Free-space propagation

The vector wave equation, which follows from Maxwell's equations, is obeyed by both the electric field $\mathbf{E}$ and magnetic field $\mathbf{H}$ at position $\mathbf{r} = (x, y, z)$ and time t for electromagnetic radiation,

$$\left(\frac{n^2}{c^2}\frac{\partial^2}{\partial t^2} - \nabla^2\right)\mathbf{E}(\mathbf{r}, t) = \mathbf{0}, \tag{2.9}$$

$$\left(\frac{n^2}{c^2}\frac{\partial^2}{\partial t^2} - \nabla^2\right)\mathbf{H}(\mathbf{r}, t) = \mathbf{0}, \tag{2.10}$$

where c is the speed of light and n is the refractive index. Each vector component follows the equivalent scalar wave equation. In this way, the behavior of the electric and magnetic fields can be simplified using a single scalar wave equation,

$$\left(\frac{n^2}{c^2}\frac{\partial^2}{\partial t^2} - \nabla^2\right)\Psi(\mathbf{r}, t) = 0. \tag{2.11}$$

The scalar field for a monochromatic wave must obey Eq. 2.11. It can be written in the familiar form,

$$\Psi(\mathbf{r}, t) = \psi(\mathbf{r})e^{-i\omega t}, \tag{2.12}$$

.

where the complex function of position, or phasor, $\psi(\mathbf{r}) = \psi_0(\mathbf{r})e^{-i\phi(\mathbf{r})}$ has amplitude $\psi_0(\mathbf{r})$ and phase $\phi(\mathbf{r})$. If Eq. 2.12 is substituted into Eq. 2.11, it is found that the phasor must obey the time-independent Helmholtz equation,

$$(\nabla^2 + k^2)\psi(\mathbf{r}) = 0. \tag{2.13}$$

The result shows that the phasor $\psi(\mathbf{r})$ is a complete description of the wave-field given that the time dependence was preconceived based on the monochromatic case. Solutions to the Helmholtz equation for free-space propagation of $\psi(\mathbf{r})$ include the Kirchhoff and Rayleigh-Sommerfield theories of diffraction. The solution to propagation, for example along the z-axis from initial position $z = 0$ to position $z = z_2$, can also be formulated in terms of the angular spectrum [2, 34],

$$\phi(x, y, z = z_2) = \mathcal{F}^{-1} \exp\left[iz_2\sqrt{k^2 - k_x^2 - k_y^2}\ \right] \mathcal{F}\psi(x, y, z = 0), \quad z_2 \geq 0. \tag{2.14}$$

Here it is expressed in terms of the diffraction operator,

$$\mathcal{D} \equiv \mathcal{F}^{-1} \exp\left[iz_2(k^2 - k_x^2 - k_y^2)^{1/2}\ \right] \mathcal{F}, \tag{2.15}$$

which acts on the unpropagated phasor from right to left: (1) Take the Fourier transform of the unpropagated scalar field $\psi(x, y, z = 0)$. (2) Multiply it by the free-space propagator function $\exp\left[iz_2(k^2 - k_x^2 - k_y^2)^{1/2}\right]$. (3) Take the inverse Fourier transform of the final expression. To simplify the solution, the paraxial assumption is made, where $|k_x|$ and $|k_y|$ are small compared to k_z. This is geometrically equivalent to small propagation angles relative to the z-axis. Using the binomial expansion of the square root in Eq. 2.14, the simplified result is the Fresnel diffraction integral for near-field diffraction [2].

$$\psi(x, y, z = z_2) = \exp(ikz_2)\ \mathcal{F}^{-1} \exp\left[\frac{-iz_2(k_x^2 - k_y^2)}{2k} \right] \mathcal{F}\psi(x, y, z = 0), \quad z_2 \geq 0, \tag{2.16}$$

$$\mathcal{D}_{Fresnel} \equiv \exp(ikz_2)\ \mathcal{F}^{-1} \exp\left[\frac{-iz_2(k_x^2 - k_y^2)}{2k} \right] \mathcal{F}. \tag{2.17}$$

Chapter 3

X-ray Imaging

Projection x-ray imaging is the most fundamental x-ray imaging modality. It involves the acquisition of a two-dimensional representation of the three-dimensional structure of an object. X-rays emitted from a source are transmitted through an object and are detected in a pixelated detector area. Differences in material complex refractive index and thickness leads to a variation in attenuation and phase as the x-ray beam traverses the medium, and therefore a corresponding two-dimensional image is produced where all information in the x-ray path is overlapping, or projected along the x-ray path.

3.1 X-ray sources

A typical x-ray source uses a vacuum tube (Fig. 3.1) to generate x-rays by bombarding a chosen target material with high energy electrons. The source of electrons at the cathode is a helical filament undergoing thermionic emission, and at the anode the electrons are focused into a spot on the target. A small number of electrons produce x-rays via bremsstrahlung and characteristic radiation mechanisms (Sec. 3.1.1). The majority of electrons interact in collisional transfer where a fraction of the electron kinetic energy is transferred to a target electron. As the target atom relaxes infrared radiation is produced which generates heat. This heat is the source of the practical limit on power density of

the focal spot size, and has ramifications for spatial resolution and (Sec. 3.1.4) and phase-contrast imaging (Sec. 3.3). High power radiography sources typically have a focal spot size on the order of 10^2–10^3 μm, and low power microfocus x-ray sources have a spot size on the order of 1–10 μm.

The output of an x-ray source can be characterized by the tube potential (kV) which controls the electron energy, tube current (mA) which controls the number of electrons flowing from the cathode to anode, and current-time product (mAs) which is proportional to the quantity of x-rays produced. The tube potential and added filtration (Sec. 3.1.2) control the effective energy of the beam, or beam quality. A hard x-ray beam has a higher mean energy than a soft x-ray beam.

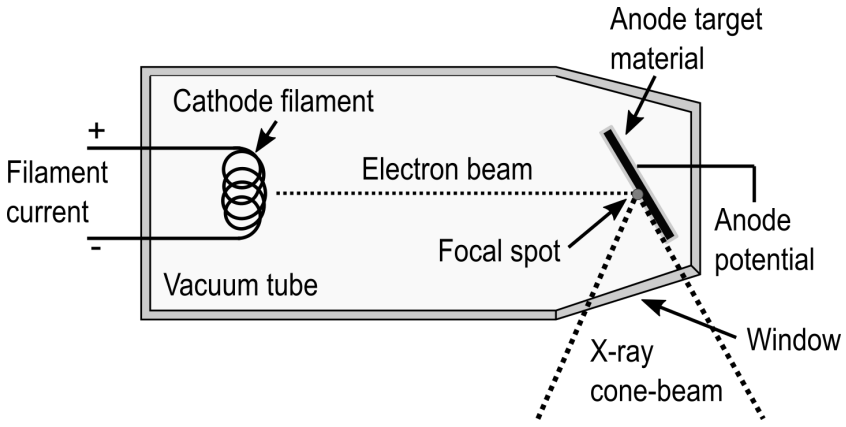

Figure 3.1: Schematic diagram of an x-ray tube.

3.1.1 Characteristic and bremsstrahlung radiation

Electron interactions with the x-ray source target atoms generate x-rays in radiative transfer. In the case of "breaking radiation," or bremsstrahlung radiation, impinging electrons accelerate near the nuclei of a target atoms, causing a reduction in energy and production of photons (Fig. 3.2a). In rare cases an electron may collide with the nucleus and be annihilated to produce a photon of equal energy. Otherwise, the photon produced must have an energy lower than the electron. The combination of many electron interactions with

target nuclei produces the continuous bremsstrahlung spectrum shown in Fig. 3.2b, with a maximum energy given by the tube potential used to accelerate the electrons at the target.

The second type of radiative transfer is generated when the bombarding electrons are above the binding energy of the target atom electrons. The energetic electrons interact with and transfer a fraction of their kinetic energy to a bound electron which is ejected from the atom. To minimize its energy state the atom fills the electron vacancy with an electron from a higher energy state, creating a photon in the process (Sec. 3.2a). For inner electron shells (e.g. K-shell and L-shell) the photons produced may have energies corresponding to x-ray radiation. Because these x-ray photon energies depend on the target atomic structure they are referred to as characteristic radiation. The discrete spectral lines of characteristic radiation are shown in Fig. 3.2b. Each line produced is the vacancy being filled using an electron from a specific energy state, for example from an L-shell (K_α) or M-shell (K_β).

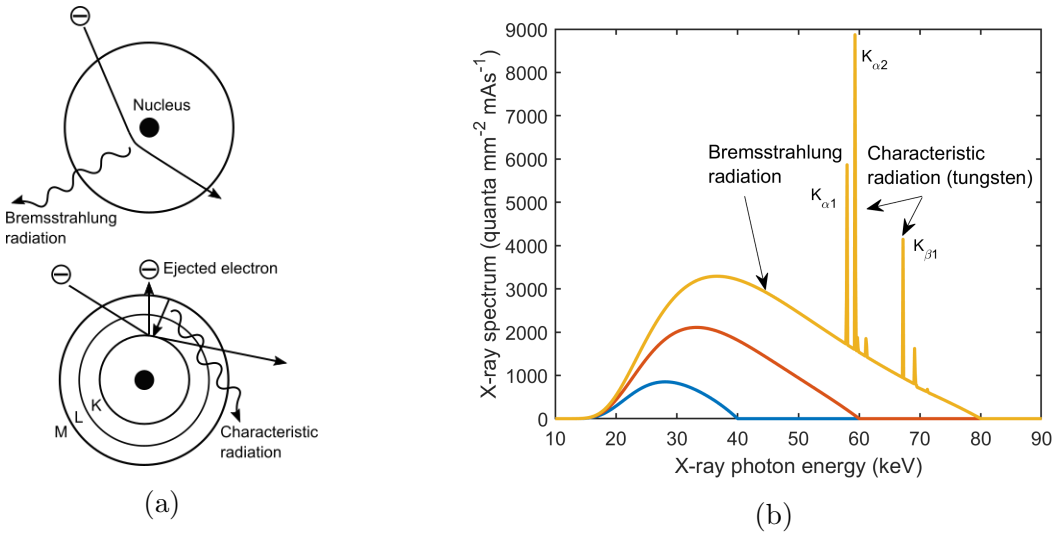

Figure 3.2: (a) Energetic electrons interacting with the x-ray source anode target material generate radiation by acceleration near the nucleus, generating bremsstrahlung radiation (top), or by ejecting an inner-shell electron, generating a characteristic x-ray photon (bottom). (b) X-ray spectra for a tungsten target anode. Characteristic radiation lines are visible above the tungsten K-edge of 69.5 keV. Calculated using [35, 36].

.

3.1.2 Filtration

Beam quality can be adjusted by adding x-ray attenuators in the beam path to "shape" the x-ray spectrum. This beam filtration is most commonly implemented in the form of adding sheets or blocks of material (e.g. aluminum) between the source and the object. The filter material preferentially removes lower energy photons from the beam, which is referred to as beam hardening. Beam hardening may be done to reduce the x-ray dose absorbed by the object, since low energy photons will be completely absorbed in the object and have no role in image formation. It can also be done to remove low energy characteristic radiation.

The effect of beam hardening is shown in Fig. 3.3. The 40 keV and 80 keV monoenergetic beams have an exponential loss in exposure (linear on a semi-log plot) with the a more rapid decrease in exposure for the lower energy, less penetrating beam. The 100 kV x-ray spectrum exhibits a curvature associated with the change in attenuation of the beam as lower energy photons are removed. Initially attenuation is more rapid than the 40 keV beam, but becomes similar to the 80 keV beam after hardening using 9 mm of aluminum.

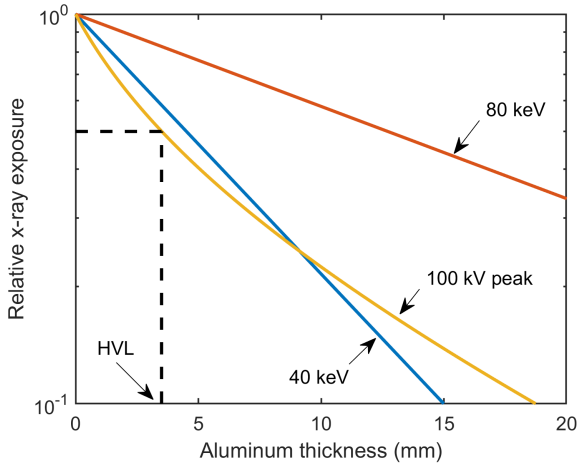

Figure 3.3: Attenuation profiles of aluminum for two monoenergetic x-ray beams and one x-ray spectrum. The 40 keV and 80 keV monoenergetic beams have an exponential loss of exposure (linear on this semi-log plot) that is more rapid at lower energy. The 100 kV spectrum has a curvature from beam hardening. Adapted from [28]. Calculated using [37].

3.1.3 Half-value layer

Beam quality of an x-ray source can be determined directly by measuring the x-ray spectrum using a photon counting detector (Sec. 3.2.2). With such a device, individual photons are counted and assigned to calibrated energy bins. Without such a spectrometer, the half-value layer (HVL) can be used as an indirect measure of beam quality. A known attenuator material (e.g aluminum) in the beam is incrementally increased in thickness until the measured exposure decreases by a factor of two. For a monoenergetic beam with attenuation coefficient α, the relationship to HVL is given by HVL $= \ln(2)/\alpha$. For the 100 kV x-ray spectrum in Fig. 3.3 the HVL is 3.5 mm of aluminum.

3.1.4 Geometric unsharpness

The spatial resolution of an x-ray source is limited by the focal spot size σ_f. Geometric magnification $M = (z_1 + z_2)/z_1$ by the cone-beam imaging geometry, shown in Fig 3.4, results in certain amount of geometric unsharpness σ_g. By the geometry of similar triangles, the focal spot size at the detector increases by a factor $(M-1)$, which reflects the fact that σ_f is projected to the detector plane through a point in the object plane. If this penumbral blurring $\sigma_f(M-1)$ is then projected back to the object plane (i.e. de-magnified) the geometric unsharpness is given by,

$$\sigma_g = \sigma_f \left(\frac{M-1}{M} \right). \tag{3.1}$$

The extreme cases are $M \to \infty$ where spatial resolution is limited by the x-ray source, and $M = 1$ where it is limited by the detector. The imaging apparatus x-ray source, detector, and geometric magnification should be optimized such that the system resolution is simultaneously higher than both the detector spatial resolution and the x-ray source spatial resolution.

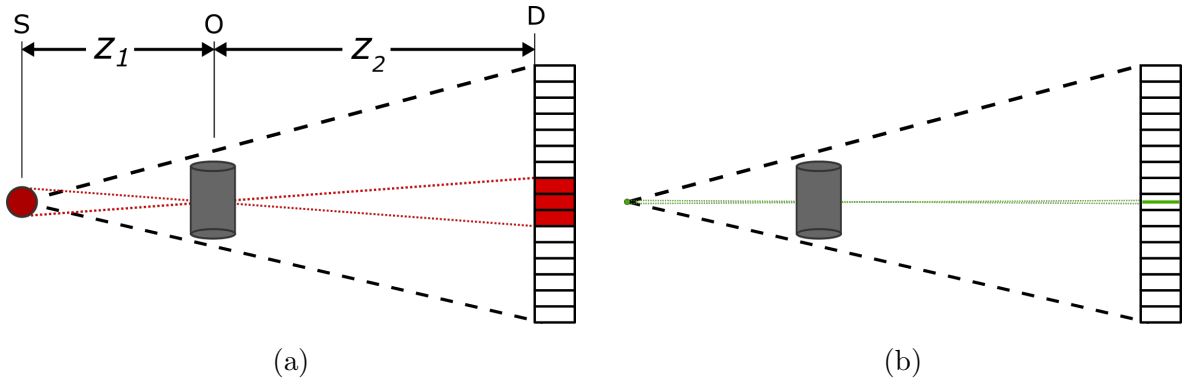

Figure 3.4: (a) Schematic of the cone-beam imaging geometry (black dashed lines) including the x-ray source focal spot (S), object (O), pixelated detector (D), and geometric unsharpness or penumbral blurring (red dashed lines). (b) When the focal spot size is reduced geometric unsharpness is minimized (green dashed lines).

3.2 X-ray detection

For more than 100 years since the discovery of x-rays by Wilhelm Röntgen in 1895, radiological examinations have been permanently recorded on film consisting of a thin sheet of plastic coated with a photosensitive emulsion. To acquire an image the film must be temporarily fixed in a cassette between two x-ray intensifying screens made of a phosphor. When this screen-film cassette is exposed to x-rays the screens produce optical light causing a degree of darkening of the film based on exposure, after it is developed. The advantages of acquiring digital x-ray images were quickly apparent following the introduction of computed tomography (CT) by Hounsfield in 1973 [38]. These advantages include rapid acquisition and digital storage, and access to image processing and communication networks. Despite the chronology, CT is a relatively sophisticated application of digital radiography, and now more recently, digital approaches to simpler imaging techniques such as projection radiography have been developed. The reason that CT was immediately accepted was the obvious benefits of tomography, a technique in which images (slices) throughout the object are reconstructed using x-ray projections taken at many points-of-view. Slices do not contain the overlap of information that plagues conventional radiography and gives CT

the ability to display subtle differences in attenuation. This benefit outweighed the desire for high spatial resolution which could not be achieved with the coarse CT detectors and limited computational capacity of the time, but which could be obtained with screen-film projection x-ray imaging. Further progress of digital radiography was impeded until the development of new detector technologies, greater computational power, high resolution digital displays, and lasers.

3.2.1 Direct and indirect conversion

Digital x-ray detectors can be classified into either direct conversion or indirect conversion techniques, referring to the direct conversion of x-rays to charge carriers or the inclusion of intermediate conversion to optical light, respectively. In either case, the digital image readout is conducted in one of three silicon (Si) semiconductor technologies: (1) crystalline Si (c-Si) charge-coupled device (CCD), (2) amorphous silicon (a-Si) thin-film transistor (TFT), or (3) c-Si complementary metal-oxide-semiconductor (CMOS). CCD detectors were developed by Boyle and Smith (1970) [39] followed much later by a-Si flat-panel detectors (FPDs) [40] in the 1990s. Both platforms have been significantly refined since their inception and have advantages and disadvantages based on the chosen imaging task. CCD detectors are capable of real-time frame rates (i.e. 30 frames per second) with relatively low noise and a pixel size that has been able to be scaled to the order of micrometers, but are limited in imaging area (order of centimeters). The a-Si detector is able to be fabricated over large area, a capability adopted from the flat-panel display industry, which permits applications such as full-field clinical radiography with an imaging area on the order of tens of centimeters (e.g. chest radiography). However, a-Si material properties results in higher noise and pixels limited to a relatively large size (> 50 μm). In the same time-frame as FPDs, CMOS imaging technology has emerged as a competitor to CCD detectors [41]. CMOS detectors have comparably low noise, a similar ability to scale to very small pixel sizes, in addition to advantages including higher frame rates, tiling capability, and compatibility with standard CMOS processing allowing high levels of integration.

In the indirect conversion method either a pixel-level a-Si/CMOS photodiode or CCD potential well is used to collect optical light generated by a scintillator such as CsI or

Gd_2O_2S (Fig. 3.5a). The direct conversion method uses a photoconductor (e.g. a-Se, CdZnTe, HgI_2, or PbO) to generate charge carriers by the photoelectric effect which are then collected under applied electric field (Fig. 3.5b).

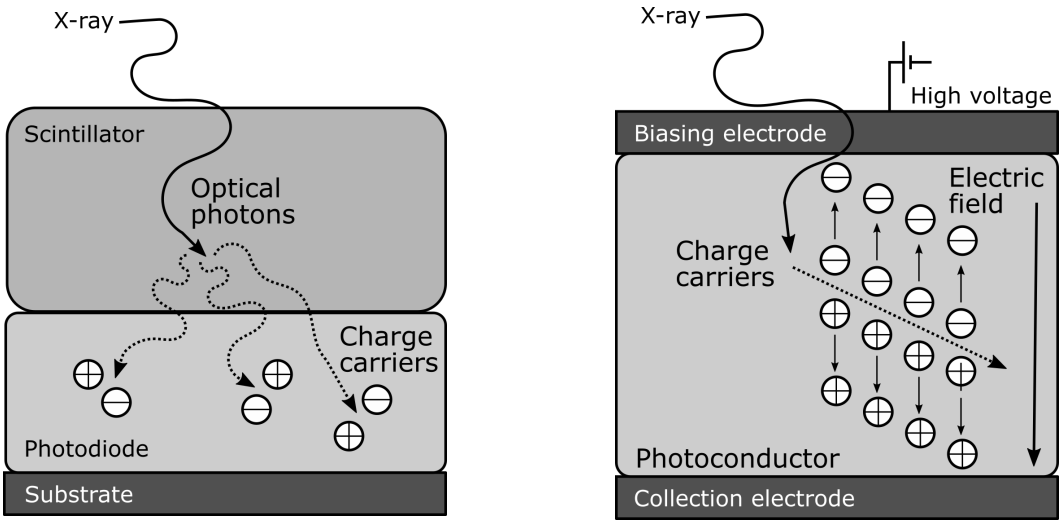

(a) (b)

Figure 3.5: (a) Indirect conversion of x-rays using a scintillator material which first converts x-ray photons into optical photons before detection using photodiodes. (b) Direct conversion of x-rays using a biased photoconductor which directly converts x-rays to charge carriers for collection.

Conventional high spatial resolution scintillator-based detectors have poor absorption efficiency at high spatial resolutions due to thinning of the scintillator to minimize secondary optical scatter. Unlike the optical scatter in scintillators, the spread of absorbed energy from x-ray interactions in the photoconductor, and subsequent diffusion of photogenerated charge carriers during transport, does not significantly degrade spatial resolution as the photoconductor thickness is increased [14].

3.2.2 Energy integration and photon counting

Photon counting detectors differentiate single photon interaction events. The charge generated by an individual photon produces a current pulse. The current pulse is passed into a shaping circuit before a comparator circuit determines if the pulse is above a certain threshold. When many thresholds are set, photons of different energies can be counted. The result is a histogram of the number of photons per energy bin. The energy bins can be calibrated using a known gamma ray source. Because of the additional complexity of the counting circuit, the x-ray flux must be limited so no two current pulses from independent photons overlap in time. It also means that large area, small pixel photon counting detectors are difficult to achieve. Photon counting detectors were discussed briefly in the context of measuring the energy spectrum of an x-ray source in Sec. 3.1.3.

Energy integrating detectors, the type used in this work, do not differentiate single photon events. This simplification means that all charge generated from many photon interactions during the integration time is collected onto some pixel-level capacitance. The collected charge may be read out using CCD, a-Si TFT, or c-Si CMOS technology. The conventional pixel architecture for a-Si is the passive pixel sensor (PPS) [42], shown in Fig. 3.6a for a direct-conversion detector. A PPS has a single storage capacitor and selection transistor. At the end of the integration time, charge stored on the capacitor is passed to an off-pixel circuit. For CMOS technology, the active pixel sensor (APS) was adopted [41]. An APS typically incorporates three transistors (3T), a reset transistor that resets the storage capacitor, a source-follower that converts collected charge to voltage, and a pixel select transistor (Fig. 3.6b). The term active originates from how the source-follower acts as an active amplifier within each pixel.

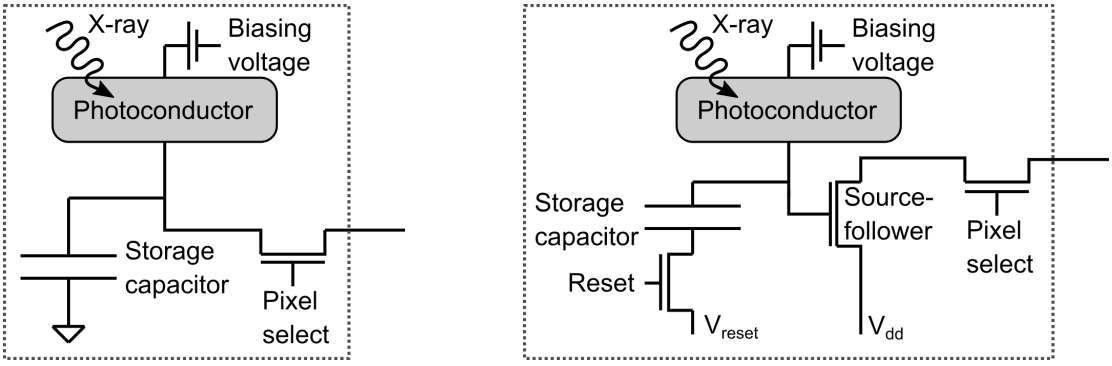

(a) (b)

Figure 3.6: (a) A PPS energy integrating pixel for photoconductor charge collection and storage before readout. (b) A 3T APS energy integrating pixel for photoconductor charge collection and storage before readout.

3.3 Phase-contrast imaging

The primary advantage of the phase-contrast paradigm is that when an object presents poor conventional absorption-contrast (e.g. soft biological tissue or other low-density materials such as polymers), contrast can instead be generated with higher sensitivity using a variety of phase-contrast modalities [31, 32]. Fundamentally this can be shown by the ratio of the refractive index decrement δ describing phase shifts, and the imaginary part of the refractive index β describing attenuation. The ratio δ/β, shown in Fig. 3.7, can exceed 10^3.

The phase of the x-ray wavefront cannot be measured directly using a conventional x-ray detector which measures x-ray intensity (Eq. 2.7). As a result, specialized optical elements have been implemented to convert the phase shifts to intensity. These phase-contrast imaging modalities include crystal analyzers [1, 3], crystal [4, 5] or grating interferometers [6], and coded-apertures [7]. In this work, phase-contrast imaging is implemented simply using free-space propagation [9, 10, 8].

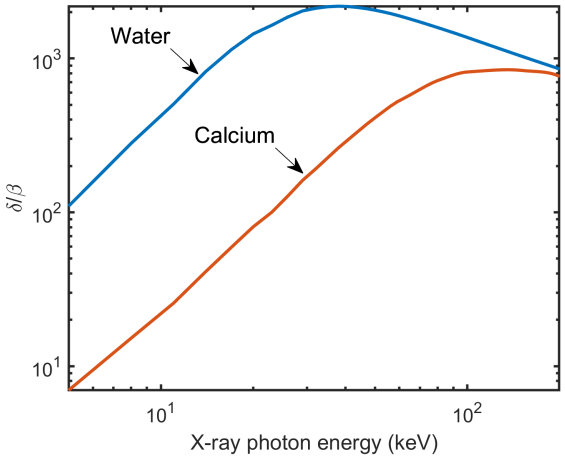

Figure 3.7: The ratio between the refractive index decrement δ and the imaginary part of the refractive index β, for water calcium. Calculated using [37].

3.3.1 Propagation-based phase-contrast

Free-space propagation can be used as a technique to render phase variations in the x-ray wavefront (due to the presence of the object) visible as intensity fluctuations at the detector. The only requirement for propagation-based phase-contrast is sufficient transverse spatial coherence length l_t, given by $l_t = \lambda z_1/\sigma_f$. Here z_1 is the source-to-object distance, λ is the x-ray wavelength, and σ_f is the x-ray source focal spot size (Fig. 3.4 for reference). The actual physical beam does not propagate in an exactly defined direction like an ideal plane wave. The transverse coherence length provides the upper limit on the separation of two object features if they are to induce interference effects. Without using a large z_1, a microfocus source (Sec. 3.1) must be used to achieve sufficient l_t for propagation-based imaging.

In the near-field regime propagation is governed by Fresnel diffraction (Sec. 2.2). The Fresnel diffraction integral (Eq. 2.16) for $\psi(x, y, z = z_2)$, which denotes the wavefront fluctuations $\psi(x, y, z = 0)$ that have been propagated a distance $z_2 > 0$, is given by,

$$\psi(x,y,z=z_2) = \exp(ikz_2)\ \mathcal{F}^{-1} \exp\left[\frac{-iz_2(k_x^2+k_y^2)}{2k}\right] \mathcal{F}\psi(x,y,z=0), \qquad z_2 > 0. \tag{3.2}$$

If the propagation distance is sufficiently small, the Fresnel free-space propagator (the second exponential factor) can be approximated by Taylor expansion as,

$$\exp\left[\frac{-iz_2(k_x^2+k_y^2)}{2k}\right] \approx 1 - \frac{-iz_2(k_x^2+k_y^2)}{2k}. \tag{3.3}$$

The intensity $I(x,y,z=z_2) = |\psi(x,y,z=z_2)|^2$ after propagation can be manipulated using mathematical simplifications into the form [2],

$$I(x,y,z=z_2) = I(x,y,z=0) - \frac{z_2}{k}\nabla_\perp \cdot \left[I(x,y,z=0)\nabla_\perp \phi(x,y,z=0)\right], \tag{3.4}$$

where $\nabla_\perp = \partial/\partial x + \partial/\partial y$ is the x and y gradient. If the intensity of the unpropagated wavefield has a sufficiently small gradient then its x and y gradient may be neglected and the so-called transport-of-intensity equation (TIE) may be expressed as,

$$I(x,y,z=z_2) \approx I(x,y,z=0)\left[1 - \frac{\lambda z_2}{2\pi}\nabla_\perp^2 \phi(x,y,z=0)\right]. \tag{3.5}$$

This result shows that the x-ray intensity profile, I, after propagating along the z-axis a distance z_2, is a function of the Laplacian of the phase-front $\phi(x,y)$ in the plane perpendicular to propagation, and is independent of wavelength (i.e. the wavelength can be replaced by a spectrally weighted sum). This produces an edge-enhancement effect (i.e. enhanced contrast) at material boundaries where the refractive index changes abruptly [8].

Chapter 4

Metrics of Detector Performance

There has been a dramatic change in technology and increase in complexity of x-ray detection since the early days of screen-film radiography. With these changes, the fundamental relationships that govern image quality and the key metrics used to compare different imaging technologies have continued to develop. Initially, first-order mean-level relationships between input and output of detector systems were studied. For example, the characteristic curve of a screen-film system was used to relate film optical density to x-ray exposure. As time progressed there was a realization that further system improvements required an understanding of higher-order relationships between the input and output of the system.

4.1 Rose model

A deterministic system presented with identical inputs will produce the same output for every such input. Alternatively, a stochastic system presented with identical inputs may produce similar, but not identical, outputs. Such is the case for detector systems due to a variety of reasons. For example, some systems may use secondary image quanta (e.g. light from a scintillator, or charge carriers in a photoconductor) to transfer the input to output, and the statistical properties of these quanta introduce a random or noisy component in the output. Therefore, detector systems are fundamentally stochastic, independent of the input statistical properties of the incident x-ray quanta.

The significance of the fundamental statistical nature of image quanta was first recognized in 1948 by Rose [43, 44], an early pioneer of imaging science. In his work, the relationship between image quanta and perception of detail is described using a differential signal-to-noise ratio (SNR). If $\bar{q}_o$ is the mean number of quanta per unit area representing a uniform object, and $\bar{q}_b$ is the mean number of quanta per unit area of the uniform background, the local contrast C can be defined as,

$$C = (\bar{q}_b - \bar{q}_o) \ / \ \bar{q}_b. \tag{4.1}$$

The differential signal for object area A was defined by Rose as, $A(\bar{q}_b - \bar{q}_o)$, and the signal noise was defined as the standard deviation of the background image quanta. In the special case of uncorrelated background quanta, noise is governed by Poisson statistics. The Rose differential SNR can then be written as,

$$\mathrm{SNR}_{Rose} = \frac{A(\bar{q}_b - \bar{q}_o)}{\sqrt{A\bar{q}_b}} = C\sqrt{A\bar{q}_b}, \tag{4.2}$$

which is always positive by assuming the background maintains a higher number of quanta per unit area relative to the x-ray attenuating object.

This relation, the *Rose model*, states that object detectability is proportional to its contrast, and the square root of the quantity of radiation. However, the conditions of Poisson-distributed noise on a uniform background and object can not be generally satisfied in practice. This is most restrictive for detector systems where noise is neither uncorrelated nor Poisson-distributed. For example, noise from readout electronics and statistical correlations from x-ray scatter or secondary image quanta. For this reason, the Rose model must be extended using Fourier-based metrics of signal and noise.

4.2 Fourier-based metrics

4.2.1 Linear and shift-invariant systems

In Fourier-based analysis of an x-ray detector system two simplifying assumptions must be made: (1) linearity, and (2) shift-invariance. This means that a system S with single spatial coordinate x (one-dimension will be used in derivations for brevity) must have an output $d(x) = \mathrm{S}\{h(x)\}$ for an input $h(x)$ that obeys,

$$\mathrm{S}\left\{\sum_i a_i \; h_i(x)\right\} = \sum_i a_i \; \mathrm{S}\{h_i(x)\}, \text{ and} \tag{4.3}$$

$$d(x - x_0) = \mathrm{S}\{h(x - x_0)\}, \tag{4.4}$$

respectively, where a_i and x_0 are constants. This can be interpreted as: (1) the system output is proportional to the input, and (2) the system output is identical regardless of where the input is located in space. The system output, or response, to a Dirac delta function $\delta(x - x_0)$ is referred to as the impulse response function (IRF),

$$\mathrm{irf}(x, x_0) = \mathrm{S}\{\delta(x - x_0)\}. \tag{4.5}$$

In two dimensions the IRF is referred to as the point-spread function (PSF). For the special case of a linear and shift-invariant (LSI) system we can write,

$$\mathrm{S}\left\{\sum_i a_i \; \delta(x - x_i)\right\} = \sum_i a_i \; \mathrm{irf}(x, x_i), \text{ and} \tag{4.6}$$

$$\mathrm{irf}(x, x_i) = \mathrm{irf}(x - x_i). \tag{4.7}$$

This result indicates not only that a superposition of Direct delta function inputs results in a superposition of the IRF, but also that the IRF is independent of position. The input function $h(x)$ can be approximated using discrete rectangles with width Δx, centered at

$x = i\Delta x$ (for index i), and area $h(i\Delta x) \times \Delta x$. If Δx is small compared to the IRF, each rectangle can be represented as a delta function at that position scaled by $h(i\Delta x)\ \Delta x$, and using Eq. 4.6 the system output can be approximated as a superposition of the scaled IRF for each delta function [28],

$$\mathrm{S}\{h(x)\} \approx \sum_i h(i\Delta x)\ \mathrm{irf}(x, i\Delta x)\ \Delta x. \tag{4.8}$$

In the limit of a continuous domain $\Delta x \to 0$, the result is the superposition integral,

$$\mathrm{S}\{h(x)\} = \int h(x')\ \mathrm{irf}(x, x')\ dx'. \tag{4.9}$$

With the addition of IRF shift-invariance (Eq. 4.7), the simplifying assumptions of an LSI result in the convolution integral,

$$\mathrm{S}\{h(x)\} = \int h(x')\ \mathrm{irf}(x - x')\ dx' \tag{4.10}$$

$$= h(x) \circledast \mathrm{irf}(x), \tag{4.11}$$

which says the IRF (or PSF) of a LSI system is unique and contains all information regarding the system required to determine the response $d(x)$ given an arbitrary input $h(x)$.

4.2.2 Modulation transfer function

To interpret the convolution integral (Eq. 4.11) in terms of the size of structures within an image we consider the special case of a spatial sinusoidal input signal $h(x) = e^{i2\pi ux}$ where u is the spatial frequency. The LSI system output is given by,

$$
\begin{aligned}
d(x) = \mathrm{S}\{e^{i2\pi ux}\} &= \int \mathrm{irf}(x')e^{i2\pi u(x-x')}\,dx' && (4.12)\\
&= e^{i2\pi ux}\int \mathrm{irf}(x')e^{-i2\pi ux'}\,dx' && (4.13)\\
&= \mathrm{T}(u)e^{i2\pi ux}, && (4.14)
\end{aligned}
$$

where we define $\mathrm{T}(u) = \mathcal{F}\{\mathrm{irf}(x)\}$ as the Fourier transform of the IRF. This Fourier-pair is the reason it is convenient to describe the system input in terms of sinusoids. Given that the Fourier transform expresses a any given function in terms of its complex sinusoidal basis functions, if input $h(x)$ has the Fourier transform $H(u)$ then,

$$
\begin{aligned}
d(x) = \mathrm{S}\{h(x)\} &= \mathrm{S}\left\{\int H(u)e^{i2\pi ux}\,du\right\}\\
&= \int H(u)\mathrm{T}(u)e^{i2\pi ux}\,du. && (4.15)
\end{aligned}
$$

If the output $d(x)$ is also expressed as a Fourier transform pair with $D(u)$, the system relationship is $D(u) = H(u)\mathrm{T}(u)$. Thus, while in the spatial domain the signal-transfer characteristics of an LSI system can be defined by a convolution with the IRF, the equivalent relationship in the spatial-frequency domain is described by a multiplication with $\mathrm{T}(u)$, the characteristic function. Given the assumed sinusoidal nature of the signal, for an input with offset a and amplitude b,

$$
h(x) = a + be^{i2\pi ux} \quad (a \geq b), \tag{4.16}
$$

it is more meaningful to characterize in terms of input modulation M_{in}, rather than Rose contrast,

$$
M_{in} = \frac{(|h_{max}| - |h_{min}|)/2}{(|h_{max}| + |h_{min}|)/2} = \frac{(a+b)-(a-b)}{(a+b)+(a-b)} = \frac{b}{a}. \tag{4.17}
$$

The modulation quantifies the relative amount the amplitude stands out from the offset, or background. The output signal using Eq. 4.14 is given by,

$$
\begin{aligned}
d(x) &= \mathrm{S}\{h(x)\} \\
&= \mathrm{S}\{a + be^{i2\pi ux}\} \\
&= a\mathrm{S}\{e^{i2\pi(u=0)x}\} + b\mathrm{S}\{e^{i2\pi ux}\} \\
&= aT(0) + bT(u)e^{i2\pi ux}, \qquad (4.18)
\end{aligned}
$$

with output modulation M_{out},

$$
M_{out} = \frac{|d_{max}| - |d_{min}|}{|d_{max}| + |d_{min}|} = \frac{a}{b}\frac{|T(u)|}{T(0)} = M_{in}\frac{|T(u)|}{T(0)}. \qquad (4.19)
$$

The ratio M_{out}/M_{in} can then be defined as the modulation transfer function (MTF),

$$
\mathrm{MTF}(u) = \frac{|T(u)|}{T(0)}. \qquad (4.20)
$$

Using this definition of MTF, spatial resolution can be defined as the relative loss of modulation as a function of sinusoidal spatial frequency (Fig. 4.1). The MTF is always unity at $u = 0$, a consequence of how modulation is defined (Eq. 4.17). In general, because of the loss in scaling information and phase information (by taking the absolute value of $T(u)$) means the MTF is not a complete description of the detector system like the characteristic function $T(u)$. For the detector systems in this work the IRF is real, which means that both $\mathrm{T}(u)$ and $\mathrm{MTF}(u)$ are even functions and positive frequencies can be used without loss of generalization. In fact, the IRF is a real *and* even function, which means $\mathrm{T}(u)$ is also real and no phase information is lost.

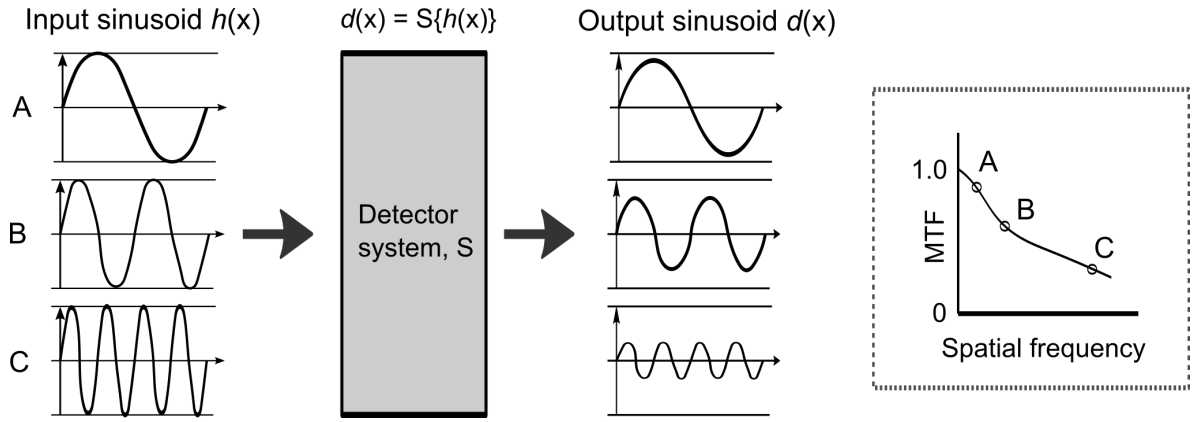

Figure 4.1: A sinusoidal input signal to a LSI system will produce a sinusoidal output signal with a modulation scaled by the MTF. Adapted from [45]

.

4.2.3 Sampling and aliasing

As with any digital system, in order to electronically detect, store and process continuous signals they must be discretized by sampling. In the case of pixelated digital detector systems the sampling pitch is naturally equal to the pixel pitch p. The signal collection area of the pixel, the pixel *aperture* a (e.g. a photodiode or electrode), is some fraction of p. If the aperture IRF is represented by the rect-function,

$$\Pi(x) = \begin{cases} 0, & \text{for } |x| > \frac{a}{2} \\ \frac{1}{2}, & \text{for } |x| = \frac{a}{2} \\ 1, & \text{for } |x| < \frac{a}{2} \end{cases}, \tag{4.21}$$

then the pixel aperture MTF is given by the sinc-function,

$$\text{MTF}_a(u) = |\mathcal{F}\{\Pi(x)\}| = \left|\frac{\sin(\pi a u)}{\pi a u}\right| = |\text{sinc}(a,u)|. \tag{4.22}$$

According to the Nyquist theorem, the highest spatial frequency accurately discretized by

the sampling pitch is $f_N = 1/2p$. Frequencies higher than f_N are aliased, i.e. "folded" to a lower frequency.

The *pre-sampling* MTF of the detector system will include blurring from the pixel aperture and other sources. The relationship between pre-sampling MTF (MTF_{pre}) and sampling MTF (MTF_{samp}) is a convolution with the sampling comb-function,

$$\begin{aligned} \mathrm{MTF}_{samp}(u) &= \mathrm{MTF}_{pre} \circledast \mathrm{comb}(u\Delta x) \\ &= \mathrm{MTF}_{pre} \circledast \left[\sum_n \delta(u\Delta x - n) \right] \\ &= \frac{1}{\Delta x} \sum_n \mathrm{MTF}_{pre}(u - n/\Delta x). \end{aligned} \tag{4.23}$$

This shows that during sampling the MTF becomes a summation of many copies of MTF_{pre} that are shifted for all n by $n/\Delta x$. All frequencies above f_N will overlap in the summation resulting in aliasing. X-ray detector systems are often under-sampled, including those in this work, and undesired aliasing is present. This with have implications for the experimental methods in Sec. 4.3.3.

4.2.4 Noise power spectrum

The deterministic transfer of signal (i.e. modulation) from Sec. 4.2.2 provides no description of the noise content of the system. One basic characterization of noise in some region of interest (ROI) with uniform expected value $\mathrm{E}\{\}$ is the variance in measurements of the detector signal d,

$$\sigma_d^2 = \mathrm{E}\{|\Delta d|^2\} \tag{4.24}$$

$$= \mathrm{E}\left\{|d - \mathrm{E}\{d\}|^2\right\} \tag{4.25}$$

$$= \mathrm{E}\{d^2\} - |\mathrm{E}\{d\}|^2, \tag{4.26}$$

where $\Delta d = d - \mathrm{E}\{d\}$. The variance can be determined by ensemble average using many images (i.e realizations) and a single pixel location, or more practically (if the system is ergodic) using a spatial average of many pixels as an estimation of the true ensemble average. If the variance at the input and output is known, the noise-variance transfer can provide some metric of noise performance. However, the concept of noise-variance transfer is not suitable for x-ray detector systems as, in general, the input variance (i.e. input image) is unknown, and the description is inadequate in the presence of noise correlations (e.g. from x-ray scatter or secondary detector quanta).

If d is expressed as a function of the spatial coordinate x, $d(x)$, the autocorrelation and autocovariance can be defined. The autocorrelation R_d describes the correlation of $d(x')$ with itself at a displacement of x,

$$\mathrm{R}_d(x', x' + x) = \mathrm{E}\{d(x')d(x' + x)\}. \tag{4.27}$$

Similarly, the autocovariance K_d describes the correlation of $d(x')$ with itself at displacement x relative to the expected values,

$$\mathrm{K}_d(x', x' + x) = \mathrm{E}\{\Delta d(x')\Delta d(x' + x)\}. \tag{4.28}$$

Its value on the diagonal ($x = 0$) is the variance of $d(x)$. The system is simplified using the assumption that the input and output can be treated as a ergodic, wide-sense stationary (WSS) stochastic processes. Many random processes in detector systems are, or can be approximated as such [28]. A random process is ergodic if every member of the process carries with it the complete statistics of the whole process and the ensemble averages can be determined equivalently from spatial averaging. The first requirement for ergodicity are moments that are stationary in space. For a WSS process, the expected value, autocorrelation, and autocovariance are stationary. [46]. When stationary, K_d will depend on the separation x but not on the position x',

$$\mathrm{K}_d(x', x' + x) = \mathrm{K}_d(x). \tag{4.29}$$

The autocovariance is a complete description of the second order statistics of a WSS process in the spatial domain [28]. In the spatial frequency domain an equally complete description of the process is provided by the Wiener spectrum, or noise power spectrum (NPS), equal to the Fourier transform of the autocovariance,

$$\mathrm{NPS}_d(u) = \mathcal{F}\{\mathrm{K}_d(x)\}. \tag{4.30}$$

Thus, like the IRF and MTF of Sec. 4.2.2, the K_d and NPS are Fourier transform pairs. An estimate of the autocovariance is given by the sample autocovariance $\mathrm{K}_{d,X}$,

$$\mathrm{K}_{d,X}(x) = \frac{1}{X}\int_0^X \Delta d(x')\Delta d(x'+x)\ dx'. \tag{4.31}$$

From Eq. 4.30, the NPS can be expressed as [28],

$$\mathrm{NPS}_d(u) = \lim_{X\to\infty}\frac{1}{X}\mathrm{E}\left\{\left|\int_X \Delta d(x)e^{-i2\pi ux}\ dx\right|^2\right\}. \tag{4.32}$$

That is, the NPS of the system can be estimated by taking a finite spatial average over X. The units of $\mathrm{NPS}_d(u)$ are $d^2 \times x$ (d^2x^2 in two dimensions). The variance, expressed in terms of the autocovarince,

$$\begin{aligned}\sigma_d^2 &= \mathrm{E}\{d(x)d(x)\} - \mathrm{E}\{d(x)\}\mathrm{E}\{d(x)\}\\ &= \mathrm{E}\{\Delta d(x)\Delta d(x)\}\\ &= \mathrm{K}_d|_{x=0},\end{aligned} \tag{4.33}$$

can be used to define the relationship between the variance and NPS using Parsaval's theorem,

$$\sigma_d^2 = \int_{-\infty}^{\infty}\mathrm{NPS}_d(u)\ du. \tag{4.34}$$

Thus, the NPS is the spectral decomposition of the noise variance. Such a relationship provides a link between the Rose model of Sec. 4.1 and the Fourier-based metrics.

4.2.5 Detective quantum efficiency

The measured NPS from Sec. 4.2.4 will have a scaling particular to the system and its parameters at the time of the measurement. For example, the pixel values reported in units of digital numbers (DN) by a digital system are variable based on factors such as the the pixel reset voltage or analog-to-digital conversion. This arbitrary scaling of noise makes it difficult to compare performance system-to-system or even measurement-to-measurement. However, the noise can be expressed in terms of the number of Poisson-distributed input photons per unit area $\bar{q}$ at each spatial frequency. In this way an absolute scaling of noise is obtained, referred to as the noise-equivalent quanta (NEQ),

$$\mathrm{NEQ}(\bar{q}, u) = \frac{|\bar{q}\mathrm{T}(u)|^2}{\mathrm{NPS}(u)} \tag{4.35}$$

The units of NEQ are that of $\bar{q}$. Further, since the MTF describes signal in Fourier analysis the SNR can be defined using the NEQ,

$$\mathrm{SNR}^2(\bar{q}, u) = \mathrm{NEQ}(\bar{q}, u). \tag{4.36}$$

By equating this definition of SNR to the Rose SNR from Sec 4.1, the NEQ can be interpreted as the effective number of Poisson-distributed x-ray quanta contributing to image SNR, or alternatively the number of quanta required to produce identical image SNR as an ideal detector. NEQ quantifies image quality on an absolute scale. In a final step, the detective quantum efficiency (DQE) can be defined as the effective fraction of Poisson-distributed quanta contributing to image SNR, or in other words the effective quantum efficiency,

$$\mathrm{DQE}(u) = \frac{\mathrm{NEQ}(\bar{q}, u)}{\bar{q}} = \frac{\bar{q}|\mathrm{T}(u)|^2}{\mathrm{NPS}(u)}. \tag{4.37}$$

As such, DQE is measure of system performance rather than image quality. Independent of $\bar{q}$, it describes detector efficiency as a function of spatial frequency, taking into account the complete signal and noise description of the system. The DQE at zero spatial frequency has

an upper bound given by the combination of quantum efficiency and Swank noise [47, 48]. Swank noise is associated with the stochastic nature of competing mechanisms that occur as an x-ray photon deposits energy in a medium. For a quantum efficiency η and Swank factor A_s, the DQE(0) is given by,

$$\mathrm{DQE}(0) = \eta A_s. \tag{4.38}$$

4.3 Experimental methods

4.3.1 Pre-processing of raw image data

Digital detector readout noise is defined as any noise source that is independent of the x-ray signal, and includes a pixel-level (spatial) dark-signal non-uniformity. Similarly, there is a pixel-level photo-response non-uniformity which is a function of signal but not stochastic. This detector fixed pattern noise (FPN) is a correlated noise with a spatial structure that is unchanged in time from image-to-image. FPN can be corrected by dark field subtraction and flat field correction. By averaging a sufficient number of dark field D (no x-ray exposure) and flat field F (uniform x-ray exposure) frames, only the nonrandom pixel-to-pixel dark current and gain variation FPN remains. A correction is applied by offset removal and gain normalization at the pixel level,

$$C_{i,j} = (R_{i,j} - D_{i,j}) \times \frac{\langle F - D \rangle}{F_{i,j} - D_{i,j}}, \tag{4.39}$$

where the subscript refers to the pixel value at location (i, j), C is the corrected image, R is the raw image, and $\langle\ \rangle$ is the two-dimensional mean operator. The first factor removes the offset and the second factor normalizes the gain.

4.3.2 Signal transfer property

The sensitivity, or overall gain, of the detector is represented using the signal transfer property (STP). The STP is expressed as the mean pixel value in an image of as a function

of exposure. To be accurate, the exposure must be uniform over the chosen region-of-interest and the FPN corrections must be applied. Exposure should be measured using a calibrated ionization chamber. The linearity of the detector can be determined from the STP by linear regression.

4.3.3 Determining MTF using the slanted-edge technique

In theory the MTF can be rapidly computed from the PSF using the discrete Fourier transform (DFT). An experiment to determine an accurate representation of the PSF, on the other hand, is not so narrowly defined [49]. For simplicity, the number of dimensions of the experiment can be reduced if instead of the PSF we work with the detector line-spread function (LSF) [50],

$$\mathrm{LSF}(x) = \int \mathrm{PSF}(x, y')\ dy', \tag{4.40}$$

In this way the MTF for the rows and columns of the detector can be determined separately,

$$\mathrm{MTF}(u, 0) = \mathcal{F}\{\mathrm{LSF}(x)\}. \tag{4.41}$$

In practice, implementing a narrow slit test device to measure the LSF requires high precision fabrication and sufficient x-ray exposure to generate image contrast. Alternatively, a straight edge can be used to measure the detector edge-spread function (ESF). This alleviates both challenges and the result can be related to the LSF simply,

$$\frac{d}{dx}\mathrm{ESF}(x) = \mathrm{LSF}(x). \tag{4.42}$$

A fundamental problem remains, which is the digital detector "false" response from aliasing due to discrete under-sampling of signals (Sec. 4.2.3) [51]. This was originally overcome by using a slanted slit which decreases the effective sampling pitch of the detector to eliminate aliasing and provide a measurement of the *pre-sampling* MTF [52]. This method of using some degree of angulation can be equivalently applied to the edge technique [53].

The "slanted-edge technique" developed for this work is based on the method by Samei *et al.* [54]. In this method a relatively x-ray opaque straight edge is slanted relative to the rows (or columns) to determine the pre-sampling MTF (for brevity, referred to as "MTF" from now on) along the columns (or rows). The experimentally acquired edge image was used to calculate a sub-pixel sampled ESF from which the LSF is determined by finite differences with a small correction [55], followed by the DFT to get the MTF. If pixels are projected using the correct edge angle (Fig. 4.2) then the true continuous ESF of the detector as a function of the distance s from the edge, ESF(s), is sampled by [54],

$$E_{i,j} = \int \mathrm{ESF}(s)\delta(s + ip\sin\theta - jp\cos\theta)\ ds, \tag{4.43}$$

where $E_{i,j}$ are a set of discrete samples at sub-pixel locations $s(i,j) = p(j\cos\theta - i\sin\theta)$ from the edge.

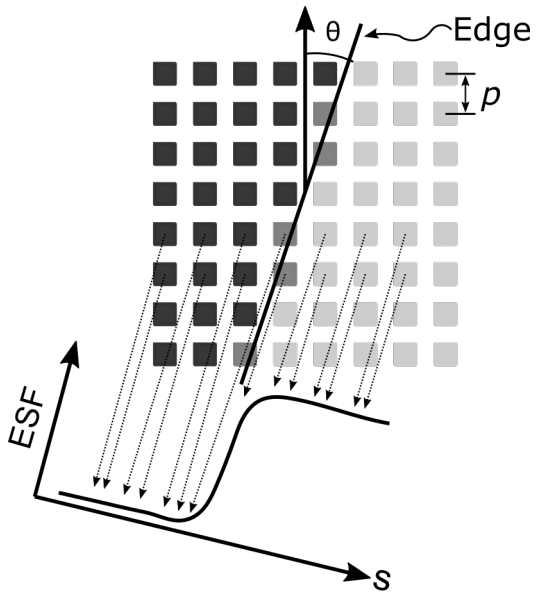

Figure 4.2: Projection of all pixel values (two rows shown) along the edge to determine the oversampled ESF. Adapted from [54].

To accurately determine the edge angle, the x-ray gray-scale image was converted to a binary image using Canny edge detection, which denotes the edge transition in white and

everything else in black. The Hough transform was then used to determine the parametric representation of the edge line $\rho = x\cos\phi + y\sin\phi$, where ρ is the distance from the origin to the closest point on the line, and ϕ is the angle from the positive x-axis to that point. A unit vector $\hat{\mathbf{u}}$ defined by ϕ (i.e. perpendicular to the edge) was used to project all pixel location vectors $\mathbf{v} = (i, j)$, $v_{edge} = \mathbf{v} \cdot \hat{\mathbf{u}}$. The scalar projections v_{edge} can then be used to order all pixel values $E_{i,j}$ into a one-dimensional oversampled edge profile along the s-axis. The sample locations s are not uniform and will have a distribution based on the pixel pitch, size of the array and edge angle. To create regular sampling for the DFT, N_k samples of $E_{i,j}$ which fall between $(k \pm \frac{1}{2})\Delta s$ are averaged into spatial bins ESF_k of size Δs,

$$\mathrm{ESF}_k = \frac{1}{N_k} \sum_{i,j} E_{i,j} \mathrm{bin}\left[s(i,j), k\Delta s\right]. \tag{4.44}$$

The bins ESF_k are smoothed using Savitzky-Golay filtering with a moving fourth-order polynomial and Gaussian weighting to reduce noise before finite differences to obtain the LSF,

$$\mathrm{LSF}_k = \frac{\mathrm{ESF}_{k+1} - \mathrm{ESF}_{k-1}}{2\Delta s}. \tag{4.45}$$

The method of local smoothing significantly reduces noise in the LSF without assuming a functional form *a priori* (e.g. fitting an error-function to the ESF which forces the MTF as a Gaussian function). A Hanning filter can be used on the LSF to reduce high frequency noise content if necessary. The MTF was calculated by DFT and corrected for finite differences using the Nyquist frequency f_N [55],

$$\mathrm{MTF}(u, 0) = \frac{1}{\mathrm{sinc}(\pi u / 2 f_N)} \mathrm{DFT}\{\mathrm{LSF}_k\}, \tag{4.46}$$

.

In order to compare spatial resolution performance of the detector, two single-valued figures-of-merit were used. The first was the spatial frequency at which the modulation, as quantified by the MTF, degrades by 50%. The second was the full width at half maximum (FWHM) of the LSF.

4.3.4 Determining NPS and DQE for digital detectors

The DQE of an LSI detector describes SNR transfer, or alternatively it describes the equivalent quantum efficiency that an ideal detector would require to produce the same image SNR as the detector under test. Using the result from Eq. 4.37 and the fact that $|\mathrm{T}(u)| = G\ \mathrm{MTF}(u)$ for detector gain G, the DQE for a single dimension can be written as,

$$\mathrm{DQE}(u) = \frac{\bar{q}G^2\mathrm{MTF}^2(u)}{\mathrm{NPS}(u)}, \tag{4.47}$$

where u are the spatial frequencies, $\bar{q}$ is the mean x-ray fluence incident at the detector plane, and $\mathrm{NPS}(u)$ is the Wiener noise power spectrum. Given that a linear detector has a mean pixel value $\bar{d}$ related to the input by $\bar{d} = \bar{q}G$, it is convenient for experiment to express DQE in the form,

$$\mathrm{DQE}(u) = \frac{\bar{d}^2\mathrm{MTF}(u)}{XQ_0\ \mathrm{NPS}(u)}, \tag{4.48}$$

where the incident x-ray fluence $\bar{q}$ is given by the product of the measured exposure X and the total x-ray fluence per unit exposure Q_0. Without a spectrometer, Q_0 can estimated using calibrated semi-empirical models [35, 36, 56, 57, 58]. Exposure should be measured at the detector plane using a calibrated dosimeter or ionization chamber.

The Wiener NPS, the spectral decomposition of the noise variance, for a digital system is given by,

$$\mathrm{NPS}(u,v) = \frac{x_0 y_0}{N_x N_y}\langle|\mathrm{DFT}\{\Delta d_{i,j}\}|\rangle \tag{4.49}$$

where $x_0 = y_0$ is the pixel pitch in the (x,y) directions of the pixel plane, N_x and N_y are the number of pixels, respectively, $\langle\ \rangle$ denotes the expectation operator, and $\Delta d(i,j)$ is the pixel value at location (i,j) with the expected value subtracted. Images are subdivided into 256-pixel $\times$ 256-pixel ROIs with 128 pixel overlap in the (x,y) directions to reduce noise. A total of four million pixels are required by IEC standards [59] to ensure an accuracy of

5%. To determine a one-dimensional cut of the NPS, 7 columns (or rows) on each side of the central axis are averaged. To compare the experimental NPS to other detectors the normalized NPS (NNPS) is calculated,

$$\mathrm{NNPS}(u) = \frac{\mathrm{NPS}(u)}{\bar{d}^2}. \tag{4.50}$$

This section follows many of the IEC standard guidelines for determining the radiographic DQE [59].

4.3.5 Verification of experimental methods

To verify the accuracy of the slanted-edge technique implementation (Sec. 4.3.3), first a noiseless 250-pixel × 250-pixel edge image with a known five degree edge angle is considered (Fig. 4.3a). A 10% transmission through the edge is assumed [54]. The edge was first constructed using a 0.2 μm simulation pitch and then blurred by a 5 μm pixel sinc-function MTF by multiplication in the Fourier-domain. Linear interpolation was then used to construct the final image at $p = 5$ μm detector pixel pitch. The sub-pixel sampled ESF is determined by projecting the image data along the edge, and a regular sub-pixel sampling pitch is created by binning at $0.1p$ intervals. The expected ramp-function ESF is shown in Fig. 4.3b before and after binning.

Naturally, no smoothing step after binning or Hanning filtering of the LSF is required to reduce noise. It is shown that from the calculated MTF (Fig. 4.4a), that when the edge angle is known exactly, the expected sinc-function MTF can be retrieved from the noiseless image with high accuracy (Fig. 4.4b). Below the 100 cycles/mm Nyquist frequency of the 5 μm pixel pitch, the relative error in MTF from the slanted-edge technique compared to the theoretical sinc-function prediction is below 2%.

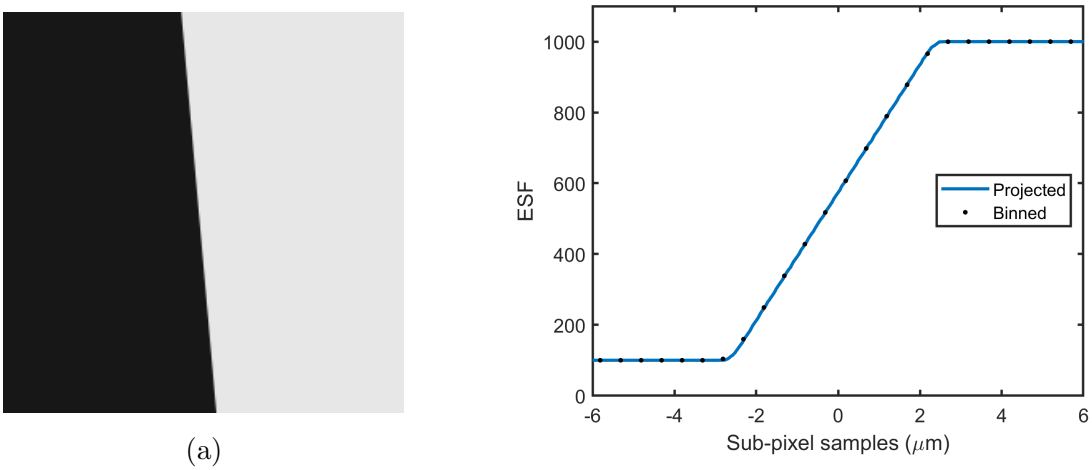

(a) (b)

Figure 4.3: (a) The constructed noiseless edge image. (b) The expected ramp-function ESF from projecting all pixel values, and binning to a regular sampling pitch.

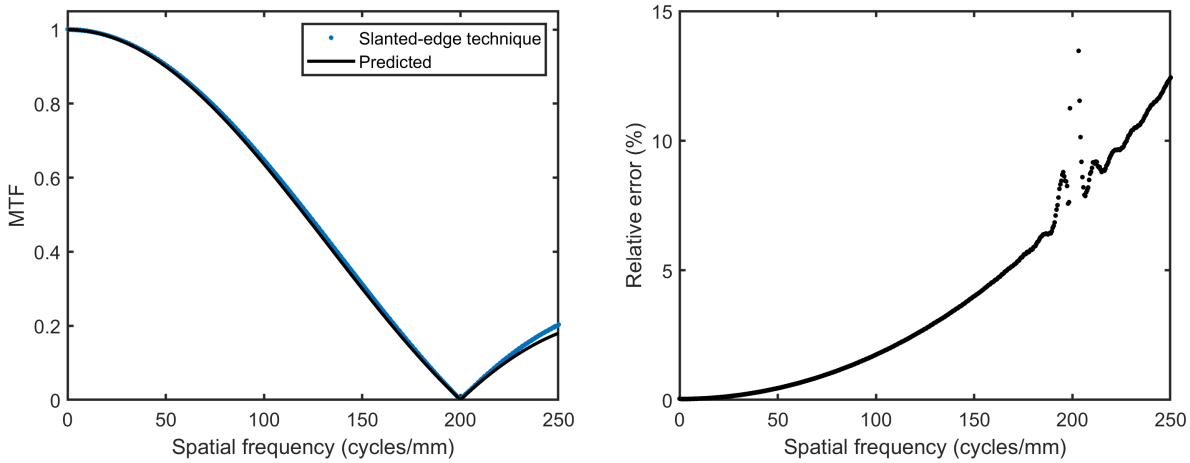

(a) (b)

Figure 4.4: (a) The sinc-function MTF retrieved from a noiseless image using the slanted-edge technique. (b) The relative error of the slanted-edge technique compared to theoretical prediction.

In the slanted-edge technique image noise is amplified by finite differences when determining the LSF. To verify accuracy in this case, Poisson noise was added to the original noiseless edge image (Fig. 4.5a). Again, the edge angle is known. The projected ESF has noise first reduced by binning, again at $0.1p$ (Fig. 4.5b). Filtering to further reduce ESF noise appears unnecessary in Fig. 4.6a, but not after noise is amplified by finite differences (Fig. 4.6b). Before the DFT a Hanning filter is applied to the LSF with a window size of 512 μm which establishes a sampling rate of 1.95 cycles/mm and eliminates high frequency content that is not associated with th edge transient. The MTF retrieved from the noisy image is shown in Fig. 4.7a. It has fluctuations not present for the noiseless image, the sampling rate has reduced by a quarter due to the Hanning window, and the relative error compared to the theoretical prediction has increased to 7% below the Nyquist frequency (Fig. 4.7b). By using the fact that the MTF is defined based on noiseless sinusoidal signal transfer, averaging a number of edge images to improve image SNR will significantly improve the result.

Until now the edge angle has been assumed known. Fig. 4.8a shows that when determining an unknown edge angle, an error of ± 0.1 degrees will begin to significantly affect the MTF result for this size image. An example of MTF results from the slanted-edge technique for random angles is shown in Fig. 4.8b.

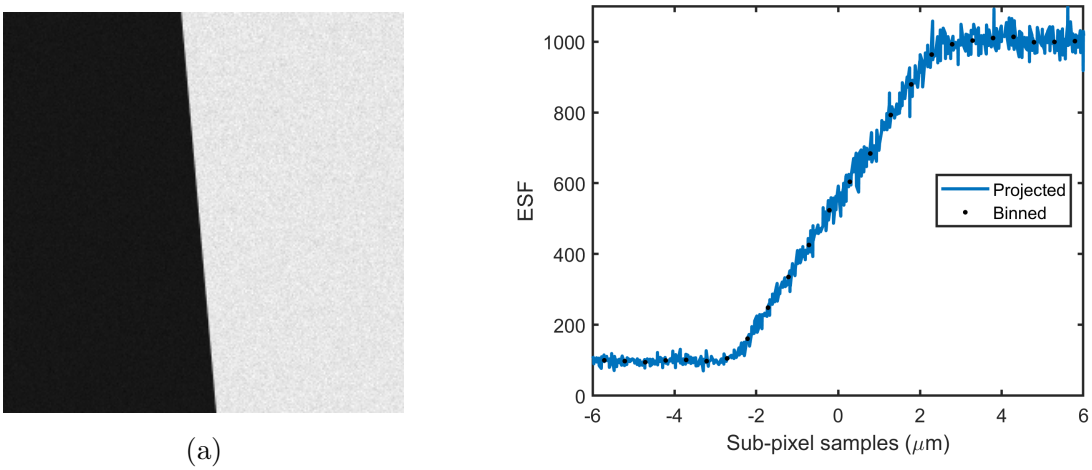

(a) (b)

Figure 4.5: (a) The constructed 250-pixel $\times$ 250-pixel edge image with added Poisson noise. (b) The expected ramp-function ESF from projecting all pixel values, and binning to a regular sampling pitch.

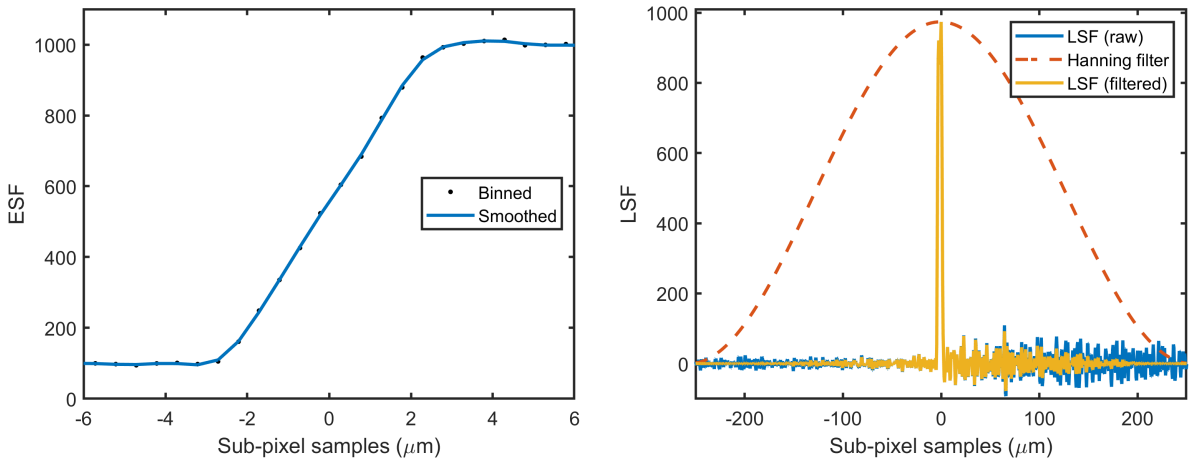

(a) (b)

Figure 4.6: (a) The ESF after binning and smoothing. (b) The LSF before and after a Hanning filter to reduce high frequency noise content not associated with the edge transient.

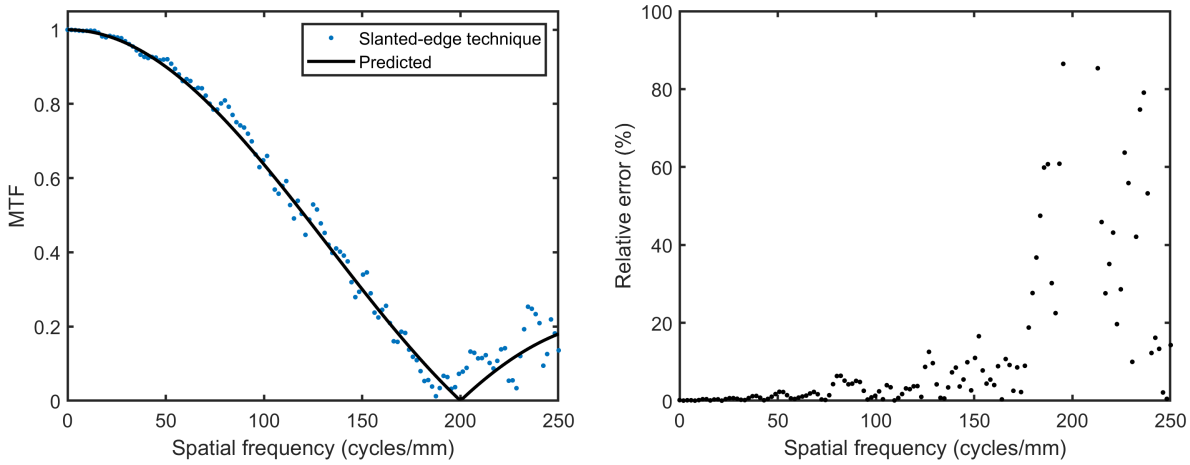

(a) (b)

Figure 4.7: (a) The sinc-function MTF retrieved from an image with added Poisson noise using the slanted-edge technique. (b) The relative error of the slanted-edge technique compared to theoretical prediction.

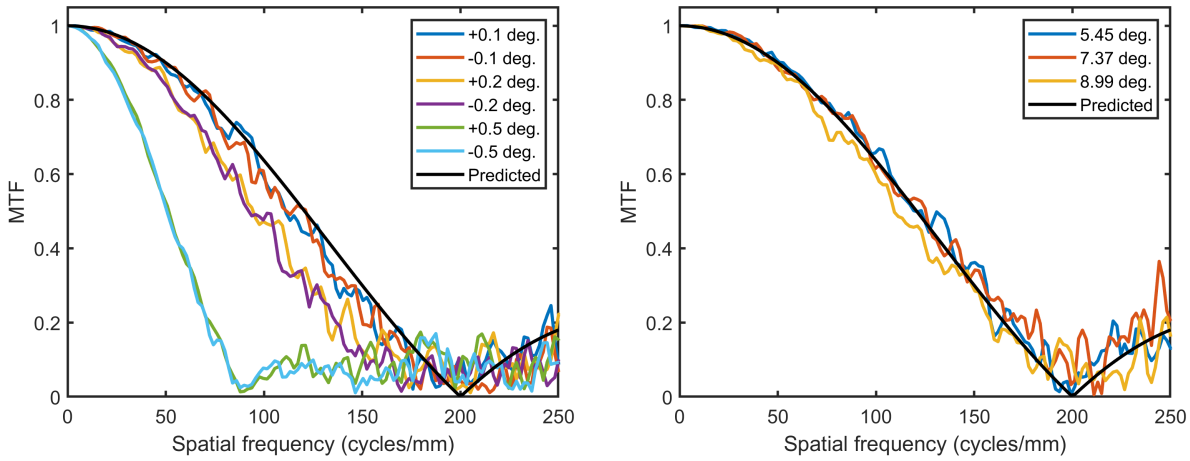

(a) (b)

Figure 4.8: (a) Deviation of the MTF from the theoretical prediction due to error in edge angle. (b) The slanted-edge technique tested for arbitrary unknown edge angles.

Chapter 5

Photoconductive Amorphous Selenium

Photoconductors for x-ray imaging are selected based on a variety of criteria including sensitivity, dark current, and fabrication constraints. Amorphous selenium (a-Se) is a preferred photoconductor in x-ray imaging because of its maturity [60], ability to be quickly and easily deposited as a uniform thick film over large area at low substrate temperatures ($60 - 70°C$), good absorption efficiency for hard x-rays, and low dark current due to its amorphous structure [61]. There has been active research to find potential x-ray photoconductors to replace a-Se due to its relatively low x-ray sensitivity. Various polycrystalline semiconductors such as CdZnTe [62], PbI_2 [63] and HgI_2 [64, 65, 66] can feasibly be deposited over large area. However, most of these photoconductors currently suffer from too high dark current or not having sufficient charge collection efficiency, and in some cases there are technological problems in manufacturing a uniform and homogeneous layer over a large area [19]. Material properties of these photoconductors are summarized in Table. 5.1.

Table 5.1: Material properties of selected photoconductors [67]. †At 10 V/μm.

Photoconductor	Absorption depth $1/\alpha$ at 30 keV (μm)	$W_{\pm}$ (eV)	Resistivity (Ω cm)	e^- mobility-lifetime $\mu_n\tau_n$ (cm^2/Vs)	Hole mobility-lifetime $\mu_p\tau_p$ (cm^2/Vs)
a-Se	149	50†	$10^{14} - 10^{15}$	$0.3 \times 10^{-6} - 10^{-5}$	$10^{-6} - 6 \times 10^{-5}$
CdZnTe	81	5	10^{11}	2×10^{-4}	3×10^{-6}
HgI_2	91	5	4×10^{13}	$10^{-5} - 10^{-4}$	10^{-6}
PbI_2	137	5	$10^{11} - 10^{12}$	7×10^{-8}	2×10^{-6}

5.1 X-ray interactions

High Z photoconductors such as a-Se ($Z = 34$) primarily attenuate hard x-rays up to ≈ 100 keV through photoelectric interactions, as shown in Fig. 5.1a. When an x-ray photon is absorbed in a photoconductive medium as a result of the photoelectric effect, an energetic primary electron is ejected from an inner electron shell. The primary electron has a large kinetic energy $E - E_{binding}$, where E is the x-ray photon energy and $E_{binding}$ is the binding energy of the electron (e.g. the K-shell binding energy, or K-edge, of a-Se is 12.66 keV). As the energetic primary electron travels within the photoconductor it transfers kinetic energy resulting in the local generation of many mobile electron-hole pairs. Additionally, the re-absorption of fluorescent photons results in non-local transport of energy. A diagram of the cross-section of a rudimentary a-Se detector is shown in Fig. 5.1b. It is a vertical structure that consists of a photoconductor layer between bottom pixel electrodes and a common top biasing electrode. Charge carriers are generated in the photoconductor bulk by x-rays incident on the common electrode, and an applied electric field causes the carriers to drift in opposite directions for collection. In this work, the higher mobility holes generated in a-Se are collected at the pixel electrodes.

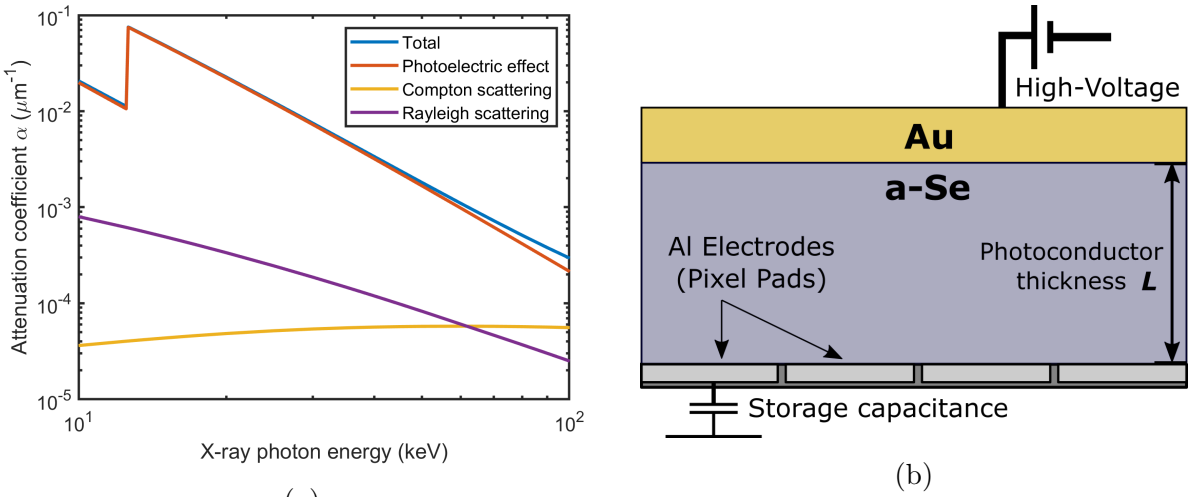

(a) (b)

Figure 5.1: (a) The contributions to the total x-ray attenuation coefficient of a-Se. Calculated using [68]. (b) A schematic of the cross-section of a rudimentary a-Se detector. The vertical structure consists of the a-Se photoconductor, bottom pixel electrodes (aluminum in this case), and a common top electrode (gold in this case).

5.2 Sensitivity

Photoconductor sensitivity is a measure of the overall conversion efficiency of incident radiation energy to charge stored on the pixel storage capacitance, and depends on three stages: (1) attenuation, (2) conversion gain, and (3) charge collection. First, the incident x-ray beam is attenuated by a fraction given by the quantum efficiency, which can be determined using Eq. 2.1,

$$\eta = 1 - e^{-\alpha(E)L}, \tag{5.1}$$

where L is the photoconductor thickness. For high quantum efficiency the photoconductor thickness should be much larger than the attenuation depth, $L \gg 1/\alpha(E)$. Figure 5.2 shows the attenuation coefficient as a function of energy for a selection of photoconductors. In

comparison to a-Se, the higher Z polycrystalline photoconductors have the advantage of superior quantum efficiency at energies greater than 30 keV. For each attenuated photon of energy E an amount of energy $E_{abs} = (\alpha_{en}/\alpha)E$ is absorbed, where α_{en} is the energy absorption coefficient.

The second stage is the conversion of the absorbed energy to electron-hole pairs. The number of electron-hole pairs $E_{abs}/W_{\pm}$ is determined using the conversion factor $W_{\pm}$ referred to as the electron-hole pair creation energy. For many crystalline semiconductors $W_{\pm}$ is proportional to the band gap E_g, as given by the Klein rule $W_{\pm} \approx 3E_g$ [69], resulting in narrow band gap photoconductors having higher sensitivity, but also higher thermal generation of carriers. The $W_{\pm}$ of low-mobility solids such as a-Se are an exception to the Klein rule, with inverse dependence on applied electric field F [70, 71],

$$W_{\pm} \approx W_{\pm}^{0} + \frac{B}{F}, \tag{5.2}$$

where $W_{\pm}^{0}$ is the intrinsic electron-hole pair creation energy, and B is a constant. The $W_{\pm}^{0}$ is 6 eV, B is weakly dependent on x-ray energy, and for the energy range 20–40 keV, $B \approx 4.4 \times 10^2$ eV V μm^{-1}. The standard electric field range is 10–20 V/μm. Consequently, the value of $W_{\pm}$ varies between 28–50 eV. In comparison, the polycrystalline alternatives have much smaller $W_{\pm}$ (Table 5.1). While smaller $W_{\pm}$ is an advantage due to generating more electron-hole pairs from the absorbed photon energy, these charge carriers must still be collected in the final stage.

As shown in Fig. 3.5b, the electrons and holes will drift in opposite directions to their respective electrodes. The drift range is given by $s = \mu\tau F$, where μ is the drift mobility, and τ is the lifetime (i.e. the mean time before the carrier is captured in a trap state). Despite the relevant large area polycrystalline photoconductors benefiting from having higher quantum efficiency and a lower $W_{\pm}$ than a-Se, they do not currently have high charge collection efficiency for both charge carriers at an electric field that results in sufficiently low dark current [19]. As a result, the sensitivity of these photoconductors in terms of charge carriers collected per unit exposure may not simply be better.

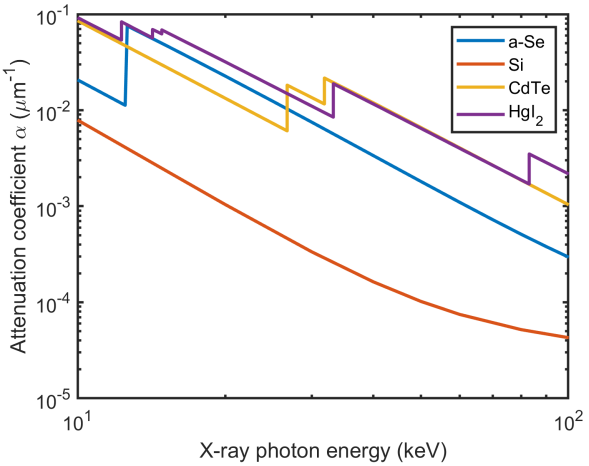

Figure 5.2: Comparison of x-ray attenuation coefficients for Si ($Z = 14$), CdTe ($Z = 48, 52$), HgI_2 ($Z = 80, 53$), and a-Se ($Z = 34$). Calculated using [37].

5.3 Dark current

For direct conversion detectors dark current is typically attributed to: (1) thermal generation of charge carriers, and (2) injection of charge carriers from the biasing electrodes. High dark current is undesirable in a detector, it increases noise and restricts dynamic range by accumulating charge on the pixel storage capacitance. For a-Se, thermally generated charge carriers in the bulk is negligible due to the large mobility gap (2.2 eV) [72]. The dominant source of dark current is then the injection of charge carriers from the electrodes [72, 73]. Unchecked injection dark current is proportional to exposure and may be difficult to correct at the pixel level [19, 74]. The dark current of a-Se may be suppressed significantly using blocking layers added to the detector structure between the photoconductor and the electrodes [75]. Alternatively, the biasing field can be kept below the typical 10-20 V/μm at the cost of lower sensitivity (Sec. 5.2). This approach is used in this work.

5.4 Cascaded systems analysis

The relationship between x-ray interactions with a-Se and the Fourier-based metrics of Sec. 4.2 can be investigated using cascaded-systems analysis, where the detector is modeled as a cascade of elementary physical processes [26, 27]. A series-parallel linear cascade model is typically used to define the signal and noise paths in direct and indirect detectors [29, 30, 76, 77, 78, 79].

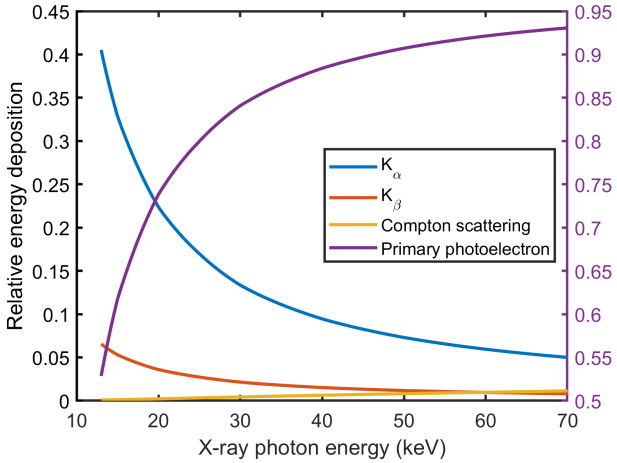

Figure 5.3: The relative energy deposition by the photoelectric effect and Compton scattering. The photoelectric effect includes energy absorbed locally from the primary photoelectron, and non-locally by re-absorbed K-fluorescence. Calculated using [21, 37, 80, 81].

Based on the comparison of relative energy deposition in Fig. 5.3, the majority of energy deposited during the attenuating process in a-Se is due to the K-shell photoelectric effect and associated re-absorption of K-fluorescent photons [21, 80, 81]. The signal and noise paths designed based on the energetic photoelectron and $K_{\alpha,\beta}$ transitions are shown in Fig. 5.4. The input x-ray Poisson statistics can be calculated using a calibrated semi-empirical spectrum model [35, 36, 56, 57, 58]. The first stage of the cascade is a binomial selection attenuation process of incident photons based on the quantum efficiency of the a-Se layer. If a photon is attenuated there are two possible outcomes: (1) Probability $1 - P_K\omega_{KL}$ that no K fluorescence occurs, and all the photon energy is assumed to be

deposited locally by a photoelectron (branch A). (2) Probably $P_K\omega_{KL}$ for a K-shell photoelectric interaction *and* K-fluorescence production. The photoelectron deposits energy locally (branch B) and the K_α or K_β photon has a probability f_k of re-absorption (branch C). The cascade model parameters are found in Table. 5.2. For the path of each branch, signal and noise transfer equations are defined for the gain, deterministic blurring, and stochastic blurring type stages [26, 27]. Gain stages include attenuation, a-Se conversion gain, and charge collection efficiency. The attenuation stage is governed by the quantum efficiency (Eq. 5.1). For each attenuated photon of energy E, the conversion gain g_{branch} for each branch is given by,

$$g_A = \frac{E}{W_\pm}, \quad g_B = \frac{E - E_K}{W_\pm}, \quad \text{and} \quad g_C = \frac{(E_{K\alpha} + E_{K\beta})/2}{W_\pm}, \tag{5.3}$$

for K-shell binding energy E_K and electron-hole pair creation energy $W_\pm$. In re-absorption of K-fluorescent photons the mean energy of the K_α and K_β photons is used. For the subsequent stochastic blurring stages, analytical equations for the MTF in these cases have been developed [21]. Finally, charge collection efficiency under applied bias is governed by the Hecht equation [82],

$$\eta_{collection} = \frac{\mu\tau F}{L}\left[1 - \exp\left(-\frac{L}{\mu\tau F}\right)\right]. \tag{5.4}$$

The stages are combined using their probability of occurrence as weighting factors. K-fluorescence branches B and C are correlated because they originate from the same photon interaction and so an additional cross-correlation term must also be added to the NPS [76]. The readout stages include deterministic blurring from the extent of the pixel aperture, noise aliasing from under-sampling (Sec. 4.2.3), and a final additive white readout noise that is independent of input signal. For noise aliasing, ten Nyquist frequency spans were considered.

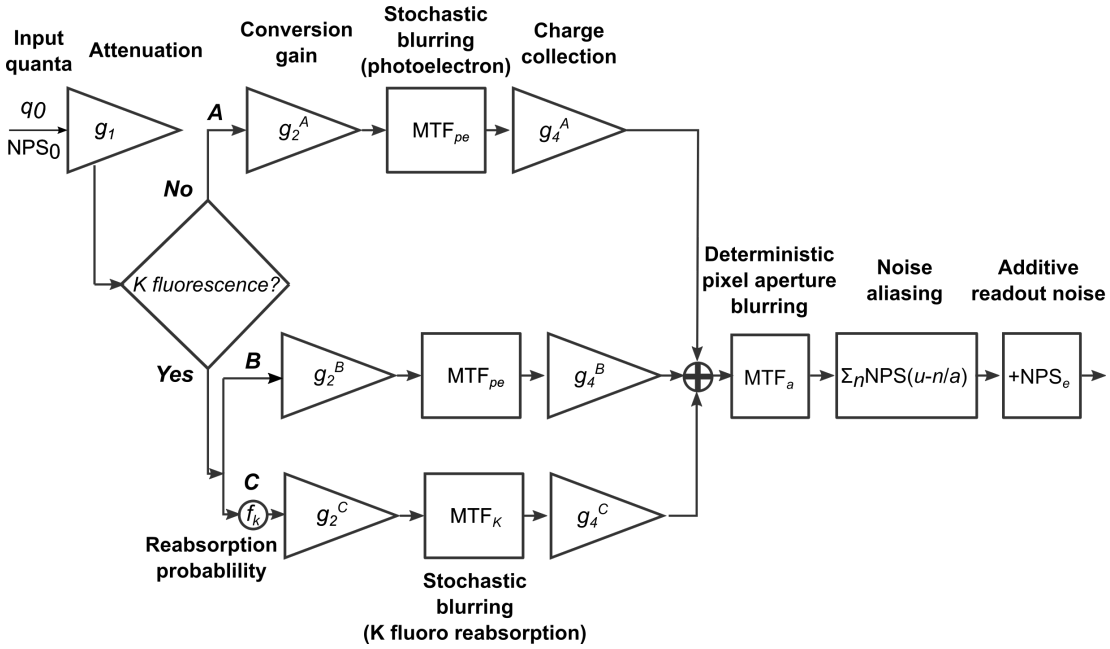

Figure 5.4: A series-parallel cascaded systems model for the a-Se/CMOS detector. The mean input quanta (q_0) and Wiener NPS (NPS_0) are determined from x-ray Poisson statistics. After attenuation, there is a probability of a K-shell photoelectric interaction and K-fluorescent photon production. If it does not occur, it is assumed the x-ray energy is deposited locally by a photoelectron (branch A). If K-fluorescent photon is produced, the incident x-ray energy minus the K-shell binding is deposited locally by a photoelectron (branch B), and there is also a probability for re-absorption of the K-fluorescent photon (branch C).

Table 5.2: K-shell photoelectric effect interaction properties for a-Se.

Parameter	Value
a-Se Density (g/cm^3)	4.4
K-edge energy E_K (keV)	12.66
K_α photon energy $E_{k\alpha}$ (keV)	11.21
K_β photon energy $E_{k\beta}$ (keV)	12.50
K-shell participation fraction P_K	0.864
K-fluorescent yield ω_{KL}	0.596

Chapter 6

PITA Detector Project

The *PITA* project was a collaboration with Teledyne DALSA Inc. to develop a process for integrating a-Se with a CMOS readout integrated circuit (ROIC) for high spatial resolution clinical x-ray imaging in the conventional absorption-contrast paradigm. A 25 μm pixel size was selected based on Monte Carlo studies by Hajdok *et al.* indicating that at the higher x-ray energies of clinical radiography and CT, 20 μm is the pixel size below which no further increase in spatial resolution is achieved [14]. Additionally, it was half the pixel size of the best in class a-Se detector by Varian Medical Systems Inc. [83].

The provided CMOS ROIC was a 3T APS with with 640-pixel $\times$ 640-pixel imaging array at 25 μm pixel pitch. The field of view was 1.6×1.6 cm^2 and the physical die size was 2×2 cm^2. The spatial resolution performance characterization of the detector included measuring the MTF and acquiring conventional absorption-contrast radiography images. This work is summarized in [22].

6.1 Back-end processing of the CMOS ROIC

For integration with the a-Se photoconductor, the scratch protection dielectric and oxide passivation layers on the CMOS surface were specified to be patterned at the foundry to allow direct contact to the aluminum pixel pads. A micrograph of both a partial and

blanket etch of these layers is shown in Fig. 6.1a. The partial etch was chosen to protect the lower CMOS layers. Back-end processing of the CMOS ROIC was implemented at the Giga-to-Nanoelectronics Center at the University of Waterloo. Process stages for vertical integration of the hybrid semiconductor detector are as follows:

1. A 1–2 μm thick polyimide (PI) layer was spin-coated onto the ROIC surface as a mechanical stabilization, or buffer, layer, using HD Microsystems PI-2600 polyimide precursors and VM-651 adhesion promoter. The imidization process and solvent evaporation was completed using a 25–350°C hot-plate temperature ramp without damage to the CMOS.

2. Spin-coating covers the entire ROIC surface, including bond pads used for signals and power. Etching the PI layer to open the bond pads was completed using a chromium etch-stop deposited using e-beam physical vapor deposition and oxygen plasma reactive ion etching.

3. The a-Se layer was deposited using thermal physical vapor deposition. Process detail for a-Se is covered in Sec. 6.1.1.

4. A gold (Au) layer was thermally evaporated as a high voltage biasing electrode for the a-Se photoconductor. The chamber was evacuated to 4×10^{-6} torr and the deposition rate was 0.2 Å/s to not damage the a-Se film.

A cross-section of buffered and un-buffered detector configurations are shown in Fig. 6.1.

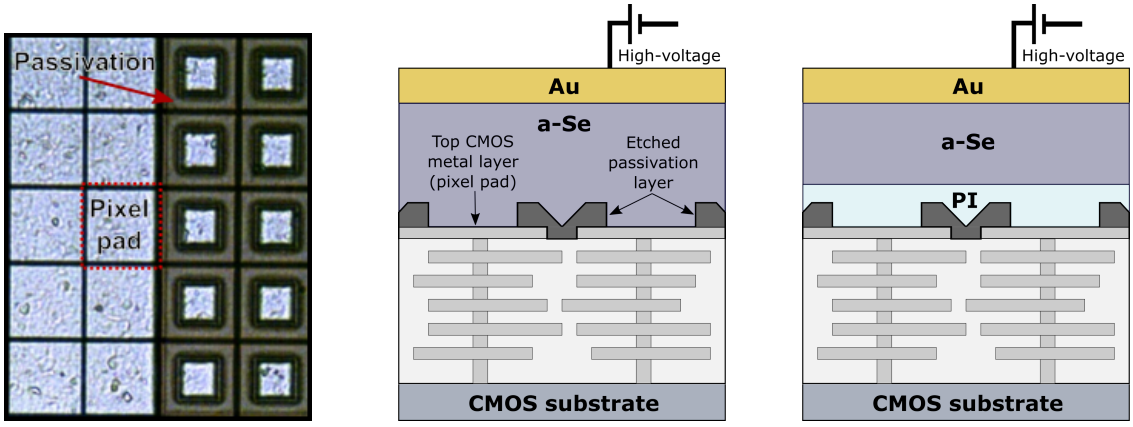

(a) (b) (c)

Figure 6.1: (a) A micrograph of the blanket etched (left), and partially etched (right) passivation layers above the pixel pads on the CMOS surface. (b) A schematic diagram of the a-Se/CMOS detector cross-section. (c) A schematic diagram of the a-Se/PI/CMOS detector cross-section.

6.1.1 Physical vapor deposition of amorphous selenium

The direct deposition of a-Se onto the ROIC surface was performed using thermal evaporation under high vacuum. In this technique the material to be deposited is evaporated from a resistive source boat which is heated using a large current. The vacuum chamber of the dedicated a-Se thermal evaporator at the Giga-to-Nanoelectronics Center, University of Waterloo, is shown in Fig. 6.2a. This system has a rotating platen and chuck to hold the substrate at the top of the chamber, and an evaporation boat located at the bottom of the chamber. The constant rotation during film deposition improves film uniformity. Two shutters, one at the boat and one at the substrate, shield the substrate until the desired deposition rate and rate stability are achieved.

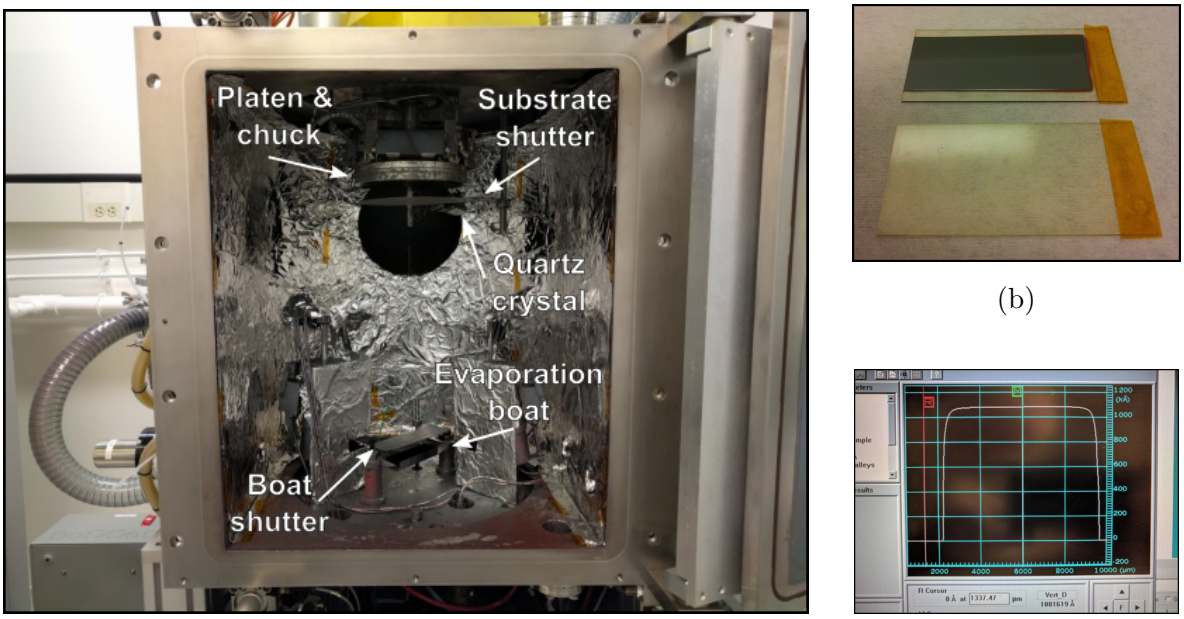

(a)

(b)

(c)

Figure 6.2: (a) The dedicated thermal evaporator for a-Se at the Giga-to-Nanoelectronics center, University of Waterloo. (b) Indium-tin-oxide (ITO) glass before (bottom) and after (top) a-Se deposition (c) An a-Se film profile using a Dektak 8 stylus profilometer.

Electronics-grade a-Se is alloyed with arsenic (order 0.1%) to prevent crystallization. A consequence of alloying a-Se with arsenic (As) is degradation of hole transport. The solution is doping with chlorine (Cl) on the order of parts-per-million (ppm) for enhanced hole transport. The result is an a-Se material with both increased stability and hole transport properties. Such a composition is referred to as *stabilized* a-Se. The source material used in this work was pellets with the composition 99.8% Se, 0.2% As_2Se_3, and 10 ppm Cl.

The chamber was evacuated to 10^{-8} torr before ramping the substrate temperature to 65°C, above the glass transition temperature of pure a-Se. This temperature allows the a-Se material structure to shift into a quasi-stable state, with stable current-voltage characteristics and resilience to thermal degradation [84]. After ramping the boat temperature and achieving the desired stable deposition rate the working pressure was 10^{-6} torr. The

shutters were then opened and film thickness was monitored using a quartz crystal. The carrier transport properties of films prepared using this process have been characterized and meet the standard for electronics-grade a-Se [85]. An example film on a glass substrate is shown in Fig 6.2b. Verification of the film profile and thickness was done using a Dektak 8 stylus profilometer (Fig. 6.2c).

The CMOS was not coated at the wafer-scale but instead the individual ROICs are provided as loose dice, which allows for higher flexibility but increases the difficulty of handling. To pattern the a-Se film a *shadow mask* was designed based on the ROIC mechanical specifications and dicing tolerances. In general, a shadow mask has a windowed area in a desired location so that evaporated material can reach the substrate for film formation, and a shadowed area where the film is undesired. The uncoated PITA ROIC and a corresponding shadow mask is shown in Figure 6.3a and 6.3b, respectively. To provide film alignment and ease of handling of loose dice, the shadow masks where designed with a recess. The ROIC dimensions vary due to dicing tolerances and the recess dimensions must accommodate the largest case, which results in significant alignment error for the smaller ROICs. The mask set was designed to take into account the alignment error and ensure that all films overlap by reducing the windowed area as films are sequentially coated.

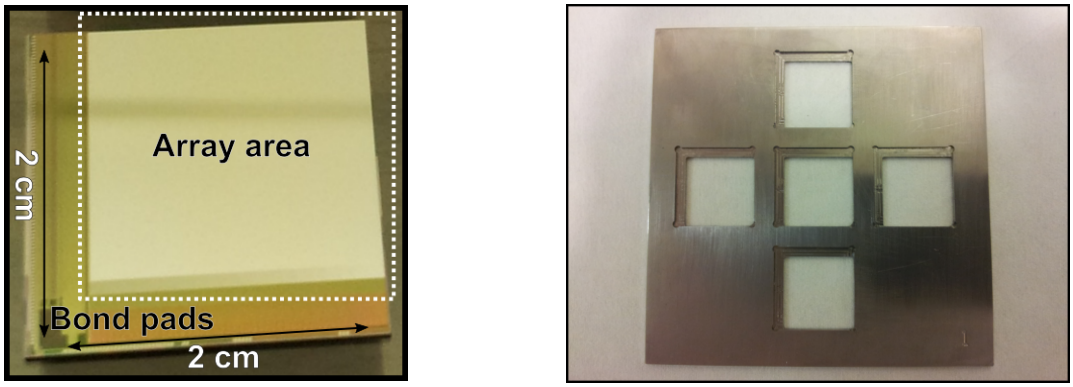

(a) (b)

Figure 6.3: (a) An uncoated PITA ROIC. The die size was 2×2 cm^2. (b) A steel shadow mask example (CNC-machined). There are five recesses, each with a window for coating the pixel array area, and a shadowed area for protecting the bond pads.

6.1.2 A first prototype detector

The prototype detector had a 1.6 μm PI layer, 92 μm a-Se layer, and a 50 nm Au layer. The a-Se layer thickness was limited only by the size of the evaporation boat and corresponding process window. A scanning electron microscopy (SEM) cross-section, shown in Figure 6.4a, was used to verify continuous and conformal CMOS/PI/a-Se interfaces. After packaging and wire bonding, a high voltage connection was made by first creating an ultra-violet-cure insulating epoxy bridge from unused pins in the package to the Au electrode. To create an electrical connection Au epoxy was run along the bridge. Two high voltage connections were made to verify conductivity. The detector was operated in hole collection mode (i.e. a positive voltage on the Au electrode) at electric fields < 10 V/μm to manage dark current and high voltage arcing. The assembled prototype detector is shown in Figure 6.4b.

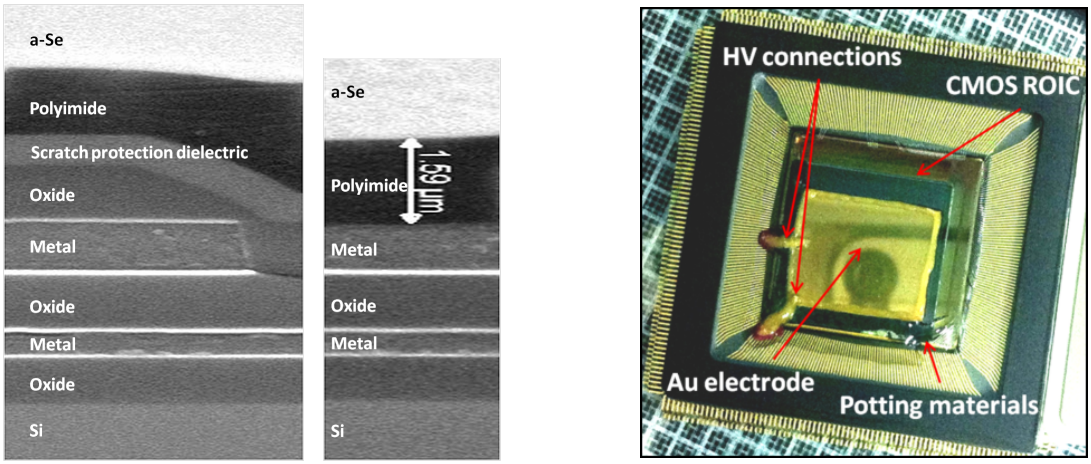

(a) (b)

Figure 6.4: (a) SEM cross-section image of the CMOS/PI/a-Se interfaces at the non-contact pixel region (left) and pixel-contact region (right). (b) The assembled prototype PITA detector. Two high voltage (HV) connections were made from the package to the Au electrode, and potting materials were used to prevent HV arcing/breakdown. What appears to be a surface feature on the Au layer is the reflection of the camera.

6.2 Spatial resolution characterization

6.2.1 Materials and methods

X-ray source

The x-ray source was located at Teledyne DALSA Inc. headquarters. It comprised a Quantum Q-Vision QGV-50 generator, Varian R10-T140V tube, and integrated Progeny MC150 R40-M-P manual collimator. The beam quality used was 40 kV with 2.7 mm Al inherent filtration. X-ray exposure was verified to be linear for a one second exposure in the 100–400 mA tube current range using a Fluke 10110AT dosimeter. Using a linear fit it was found that at a distance of 27 cm form the x-ray source focal spot the exposure obeys, $X = 0.006$ mR mAs^{-1}.

Signal transfer property

The detector was located 75 cm from the focal spot and the frame integration time was a constant 120 μs. The calibrated x-ray exposure from the x-ray source was corrected by the dimensionless factor (27 cm/75 cm)^2 using the inverse-square law for exposure fall-off with distance from the focal spot. Dark- and open-field images were taken at tube currents 100, 200, 320, and 400 mA, corresponding to an 8.96–44.80 mR exposure range. Offset and gain correction was performed and the pixel response was averaged in a 130 $\times$ 350 pixel region-of-interest (ROI). The mean pixel value of the ROI from three frames was averaged for each exposure. The STP measured was performance at two a-Se electric fields, 6.5 V/μm and 8.7 V/μm.

Modulation transfer function

The slanted-edge technique (Sec. 4.3.3) was used to measure the MTF. The edge-image was acquired using 0.5 cm $\times$ 1 cm $\times$ 3 cm machine cut tungsten (provided by Teledyne DALSA Inc.) placed across the detector package surface which lies 1 mm above the detector. To minimize geometric unsharpness the detector was located at a 75 cm distance from the

focal spot. A bin size of $0.2p$ for pixel pitch p was chosen as a balance between noise and sampling frequency followed by fourth-order Savitzky-Golay filtering using gaussian weighting with a window size of 11. No further processing was required after determining the LSF.

To compare the predicted and experimental MTF the x-ray spectrum was modeled using the SpekCalc software package [57, 58]. A 40 kV tube voltage and 2.7 mm Al filtration resulted in a mean spectral energy of approximately $E_m = 28$ keV, which was used as a pseudo-equivalent monoenergetic beam.

In addition to the x-ray processes in a-Se (Sec. 5.1), charge carrier trapping in the a-Se bulk and pixel-side blocking layer are additional sources of blur that have been investigated [17, 86]. The a-Se layer of the detector was relatively thin at $L = 92$ μm, so despite the low 6.5 V/μm biasing field the mean charge carrier schubweg (distance traveled between deep trapping events),

$$s_p = \mu_p \tau_p F = 794 \ \mu\text{m} \gg L, \quad \text{and} \tag{6.1}$$

$$s_n = \mu_n \tau_n F = 288 \ \mu\text{m} \gg L, \tag{6.2}$$

for holes and electrons, respectively (calculated from [85]), was sufficient to avoid significant carrier trapping in the a-Se bulk. Abbasazadeh *et al.* [87] used PI as hole blocking layer at higher electric fields (> 10 V/μm) and demonstrated that electron build-up at the a-Se/PI interface at 35 V/μm is insignificant in that any decrease in photocurrent over time is indistinguishable from that of an a-Se detector lacking a blocking layer [75]. Due to poor charge conduction at the low operating field (6.5 V/μm) used when acquiring the edge-image, hole build-up at the a-Se/polyimide interface was enhanced as possible source of blurring. Hunter *et al.* [88] has previously described the MTF for carrier trapping at interface states between a-Se and blocking layers,

$$\text{MTF}_b(u,v) = \frac{(L+l)^2 \sinh(2\pi u L) \sinh(2\pi v L)}{L^2 \sin[2\pi u(L+l)] \sin[2\pi v(L+l)]}, \tag{6.3}$$

where l is the thickness of the polyimide layer, L is the thickness of a-Se, and (u, v) are the spatial frequencies. The pre-sampling MTF of the detector for a pixel aperture a and is then given by,

$$\mathrm{MTF}_{pre}(u, v; a) = \mathrm{MTF}_{Se}(u, v; E_m, L)\mathrm{MTF}_b(u, v; l, L) \times |\mathrm{sinc}(u, v; a)|, \tag{6.4}$$

where MTF_{Se} is a weighted sum of the a-Se photoelectron MTF and K-fluorescence MTF, based on relative energy deposition. MTF_{Se} could be predicted simply using the methods of Que *et al.* [21] without the need for cascaded systems analysis. Incident x-ray obliquity was determined an insignificant source of blurring in advance, which can be understood by considering the relatively low mean x-ray energy and small 0.6° angle subtended by the detector field of view.

6.2.2 Results

Signal transfer property

Regression analysis showed that for both a-Se electric fields, 6.5 V/μm and 8.7 V/μm, the measured data could be described accurately by a linear fit with a coefficient of determination of 0.9996 and 0.9998, respectively (Fig. 6.5). The change in STP gain with applied electric field was consistent with the electric field dependence of a-Se x-ray conversion gain $W_{\pm}$. From Eq. 5.2, $W_{\pm}$ equals 73.7 eV and 56.6 eV for 6.5 V/μm and 8.7 V/μm, respectively. The ratio of the experimental STP, 48.77/36.09 = 1.35, was within 4% relative error of the ratio of the electron-hole pair creation energy, (73.7 eV)/(56.6 eV) = 1.30.

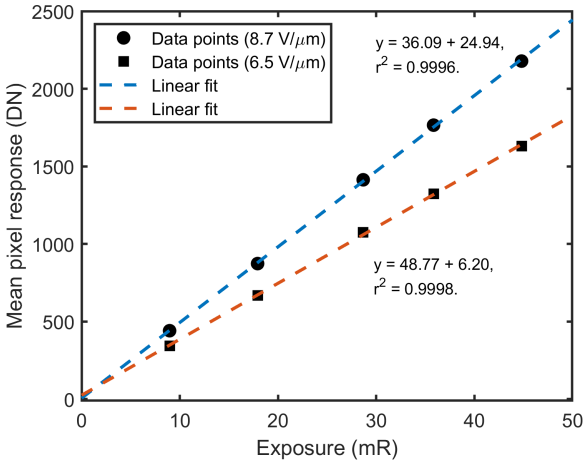

Figure 6.5: The STP measured at two applied biasing voltages. The sensitivity is inversely proportional to the electric field in a-Se.

Modulation transfer function

The acquired edge image cropped to a 256-pixel × 58-pixel ROI is shown in Fig. 6.6a. Following from Sec. 4.3.3, the edge line was isolated using Canny edge detection (Fig. 6.6b) and the Hough transform gave a parametric representation of the edge line with an angle of 6.33°. The projection of pixel positions along the edge gave the ESF shown in Fig. 6.7a. The LSF determined from finite differences (Fig. 6.7b) had a FWHM of 24 μm. After DFT, the resulting MTF is shown in Fig. 6.7c and drops to 40% at the Nyquist frequency $f_N = 20$ cycles/mm.

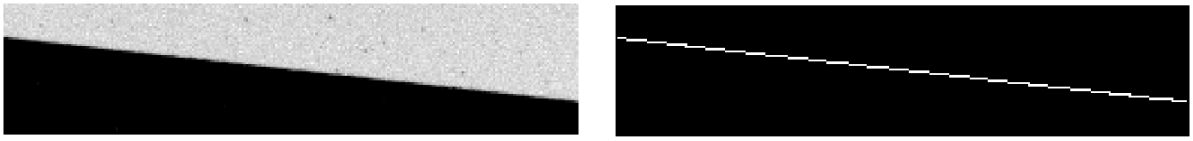

(a) (b)

Figure 6.6: (a) The edge image acquired using a tungsten edge. (b) The edge image processed using Canny edge detection.

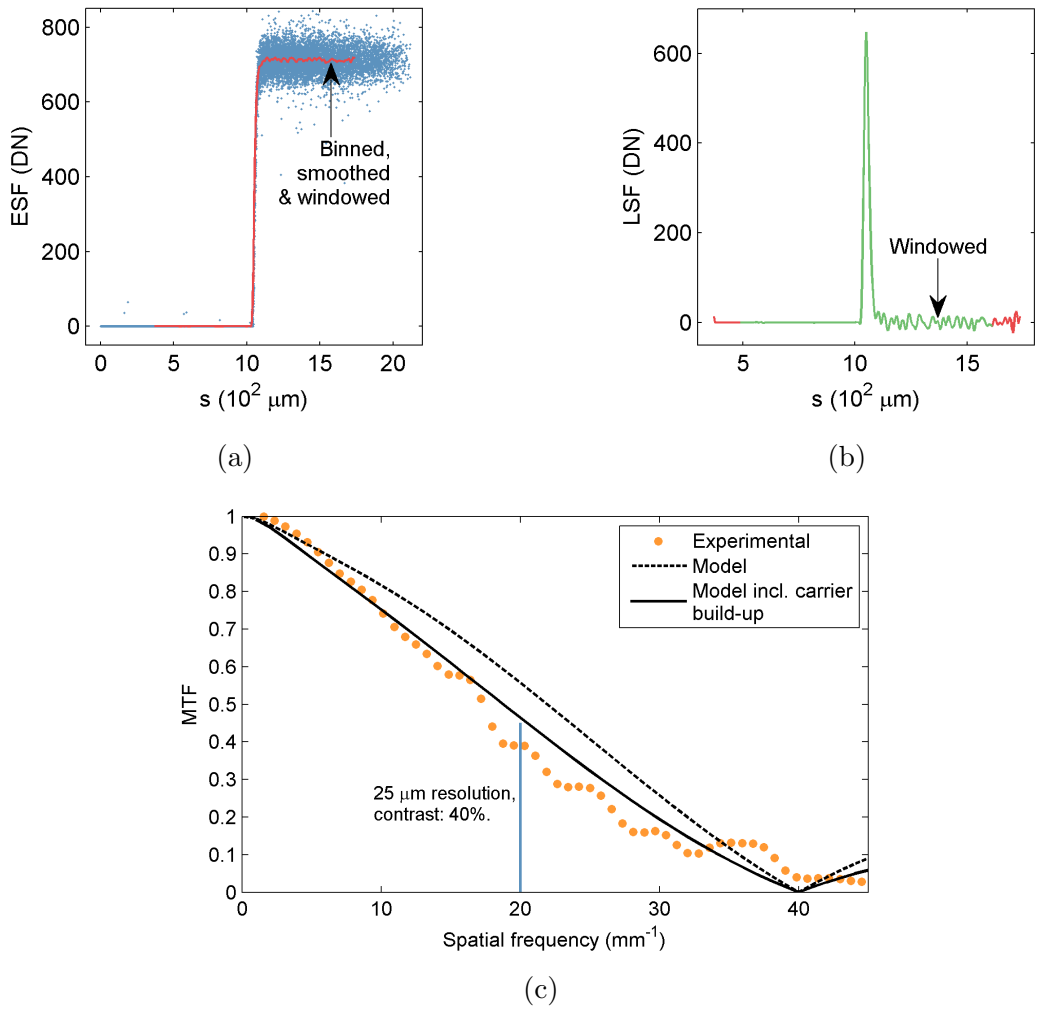

Figure 6.7: (a) The experimental ESF. (b) The experimental LSF with 24 μm FWHM. (c) The experimental MTF and the monoenergetic MTF model with and without blurring due to carrier build-up at the a-Se/PI interface.

It was predicted that at the 28 keV mean spectral energy, 82% of absorbed energy in a-Se was due to the primary photoelectron. However, for this relatively low energy, the MTF associated with the primary photoelectron degrades by 50% only after a large 223 cycles/mm spatial frequency span, well beyond f_N, and is insignificant to the overall

detector MTF. The remaining 18% of absorbed energy is due to the re-absorption of K-fluorescent photons and is the main source blurring due to x-ray interactions (50% MTF at 8 cycles/mm).

Blurring due to x-ray interactions, specifically K-fluorescence re-absorption, and the extent of the pixel aperture are not sufficient to explain the measured MTF, as seen in Fig. 6.7c. Using the assumption of charge trapping at the a-Se/polyimide interface (Eq. 6.3), the experimental and predicted MTF were in closer agreement (Figure 6.7c).

Absorption-contrast imaging

As a qualitative demonstration of spatial resolution performance, images of an aortic stent in a glass vial (Figure 6.8a), and animal jaw (Figure 6.8b) were acquired using the prototype detector. A stent is a medical device, constructed as a small mesh tube, used to treat narrow or weak arteries in interventional radiology. Object features down to 25–50 μm are well defined.

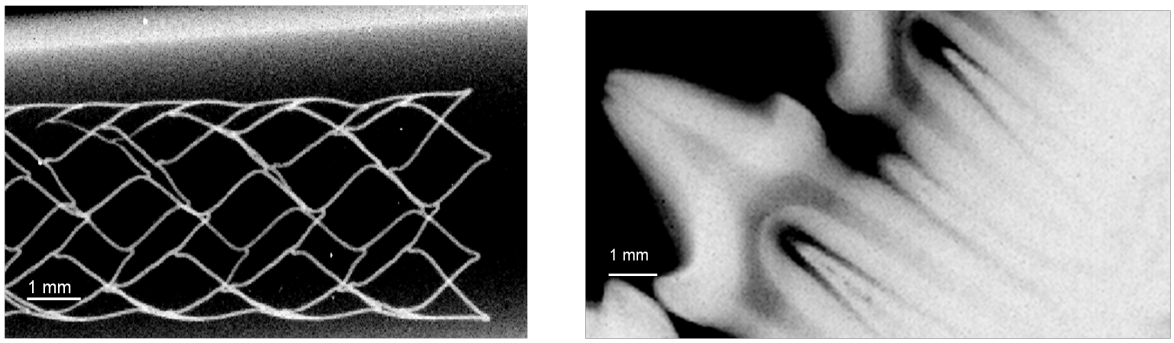

(a) (b)

Figure 6.8: (a) The image of an aortic stent with 25–50 μm wire diameter. (b) The image of animal teeth and jaw bone.

6.2.3 Discussion

The detector STP was shown linear and consistent with change in a-Se electric field over a 8.96–44.80 mR exposure range. Spatial resolution was characterized by a LSF with 24

μm FWHM and 40% MTF at Nyquist frequency. A similar MTF was obtained by Hunter *et al.* [88] for a 200 μm a-Se layer deposited onto a slot-scanning CCD prototype with 1 mm $\times$ 25 μm pixels.

A monoenergetic MTF at the mean spectral energy was used to predict the experimental outcome. The predicted MTF was higher than the measured MTF, something that could be explained by additional blurring due to trapping at interface states between a-Se and PI that was exacerbated by poor conduction at the 6.5 V/μm operating field. PI-buffered versus un-buffered substrate conditions demonstrate a reduction in the onset of photo-crystallization [89] and photo-darkening [90]. Details of detector lifetime on buffered vs. un-buffered substrates was not the primary motivation of this work and will not be discussed further. In fact, the PI layer was omitted in subsequent detectors for reasons specific to those projects.

Finally, conventional absorption-contrast radiography was used to show that object features down to 25–50 μm are well defined.

Chapter 7

AM2 Detector Project

The in-house designed CMOS ROIC designated *AM2* was developed to continue the characterization of hybrid a-Se/CMOS detectors for application to phase-contrast x-ray imaging [23, 24, 91]. The pixel size was reduced to 5.6 μm in order to verify the inherent spatial resolution of a-Se, as well as to compete with the high spatial resolution CCD detectors traditionally used to acquire propagation-based phase-contrast images [32, 92, 93, 94]. In addition to spatial resolution, noise performance was to be analyzed. Finally, a microfocus x-ray source was installed for the necessary spatial resolution and lateral spatial coherence length to visualize propagation-based edge-enhancement.

The ROIC comprised four imaging arrays, including the 5.6 μm $\times$ 6.25 μm 3T APS used in this work. The array size was 32 $\times$ 32 pixels, the physical die size was 1.8 mm $\times$ 3.0 mm, and the readout noise was approximately 100 electrons RMS [23].

7.1 Back-end processing of the CMOS ROIC

Details of the CMOS ROIC back-end processing are described in Sec. 6.1. The AM2 detector omitted the polyimide buffer layer as the spin-coating and etching requirements on such as small 1.8 mm $\times$ 3.0 mm die were beyond our micro-fabrication capability and the overall detector yield was already affected by the additional handling and packaging

challenges. A continuous 56 μm a-Se layer was deposited in a large area over all four arrays to allow shrinking of the gold layer to ensure overlap, as well as provide an area for the high voltage biasing connections. The die after a-Se deposition is shown in Fig. 7.1a. A 30 nm gold layer was deposited as the biasing electrode, also covering all four arrays (Fig. 7.1b). Visible defects at the film edges are due to unavoidable flaws in the shadow masks, and the gold layer can also be affected by asymmetry due to a stationary substrate during deposition.

After the depositions, the die was fixed in a ceramic package using silver paste and aluminum wedge wire-bonding at 30°C was used to prevent a-Se crystallization. High voltage biasing of the a-Se layer was initially provided by two wire bonds which were used to verify conductivity. A packaged die is shown in Fig. 7.1b. The biasing wire bonds were determined unreliable and also damaged the surface of a-Se, so an external probe was used to contact the gold electrode as an alternative (Fig. 7.2b).

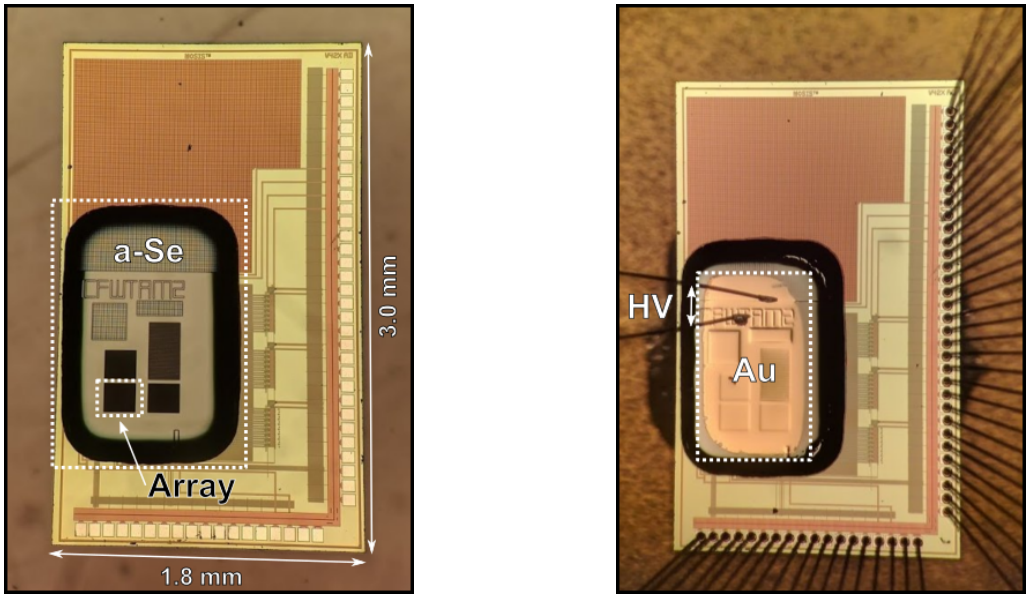

(a) (b)

Figure 7.1: (a) The AM2 die after a-Se deposition. (b) The AM2 die after gold (Au) deposition and packaging. Two wire-bonds to the surface of the Au layer are used to verify conductivity and supply the high voltage (HV) bias.

7.2 Signal and noise performance characterization

7.2.1 Materials and methods

Imaging apparatus

The imaging system is shown in Fig. 7.2b. The detector is fixed at the bottom of a vertical shielded cabinet. X-rays are generated from the top of the cabinet using a SR-115 clinical radiography source (Source-Ray, Inc.). Geometric unsharpness from the cone-beam geometry is shown in Fig. 7.2a. The x-ray tube stationary tungsten anode had a 1 mm focal spot size. Tube potential could vary between 40 and 100 kV. Tube current was a constant 15 mA, and the maximum exposure time was 4 seconds, or 60 mAs.

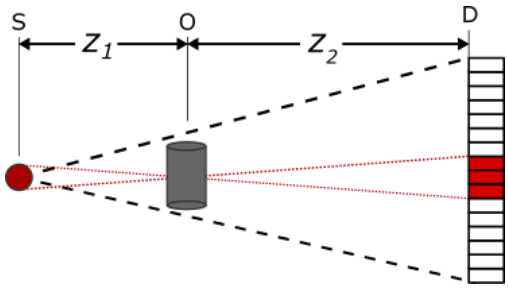

(a)

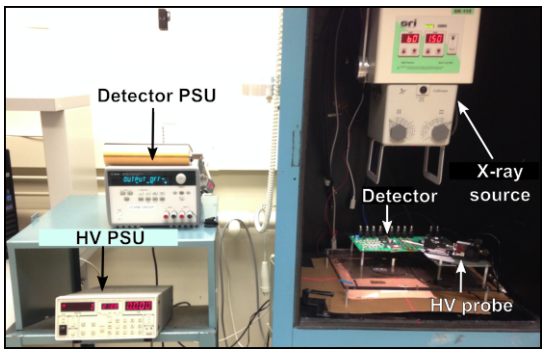

(b)

Figure 7.2: (a) A schematic of the cone-beam imaging geometry (black dashed lines) including the x-ray source focal spot (S), object (O), detector (D), and geometric unsharpness or penumbral blurring (red dashed lines). A large focal spot size can cause penumbral blurring larger than the pixel size, even at low magnification. (b) The imaging system is comprised of the detector power supply unit (PSU), high voltage (HV) PSU, probe for biasing a-Se, radiography source with 1 mm focal spot, and the AM2 detector prototype.

Signal transfer property

The detector was operated with a 313 V bias on the gold electrode resulting in an a-Se electric field of 5.6 V/μm and electron-hole pair creation energy of $W_{\pm} = 84$ eV. Because of the fixed tube current, x-ray exposure could only be increased by either decreasing the source-to-detector distance or increasing the integration time. Because of the delicate placement of the biasing probe tip on the gold electrode (Fig. 7.2b) and lack of vertical adjustment/alignment, a variable integration time was the only option. For each exposure, pixel values are temporally averaged using a series of offset and gain corrected frames. The mean frame value is then determined by spatial averaging, excluding pixels in the first and last row and column, which are used to collect excess signal generated in a-Se beyond the pixel array area.

Modulation transfer function

To verify that the slanted-edge technique (Sec. 4.3.3) could produce an accurate MTF using the 28-pixel $\times$ 28-pixel array, a simulated image was constructed with 12 degree edge angle, 5.6 μm pixel blurring, and Poisson noise. If accurate, the slanted-edge technique should return the corresponding Fourier-domain pixel sinc-function.

The experimental edge image was acquired using a 5.6 V/μm biasing field and a 70 kV tube potential. An x-ray opaque edge of rectangular machine cut lead was aligned at an angle to determine the MTF along the 5.6 μm pixel pitch direction. The lead edge is positioned at the maximum available source-to-object distance of $z_1 = 46$ cm, and the minimum object-to-detector distance of $z_2 = 0.5$ cm by resting it on the detector package just above the wire bonds, in an attempt to minimize geometric unsharpness. The geometric magnification of this configuration is $M = 1.01$, and the MTF of this blurring for a focal spot size σ_f can be modeled using [95],

$$\mathrm{MTF}_f(u) = \exp\left(-\pi\left[\frac{(M-1)}{M}\sigma_f u\right]^2\right). \tag{7.1}$$

Detective quantum efficiency

To characterize beam quality the HVL was measured by adding 0.5 mm and 1 mm high purity Al sheets. The HVL was used to adjust the semi-empirical spectrum model [35] for accurate determination of the number of input quanta per unit exposure. Exposure was measured using a Solidose 300 with R100 solid-state detector. Finally, due to the small size of the pixel array, the NPS was calculated using a single 28-pixel × 28-pixel ROI.

7.2.2 Results

The x-ray source HVL was measured to characterize beam quality. At 70 kV, the x-ray exposure decreased to half with 3.12 mm of added Al (Fig. 7.3a). The slope on a semi-log plot is not linear because of beam hardening. The HVL-adjusted semi-empirical spectrum model [35] had a mean energy of 41.4 keV and fluence per unit exposure of 1.83×10^8 quanta mm^{-2} R^{-1} (Fig. 7.3b). The measured STP at 50 kV is shown in Fig. 7.4 and is linear over two orders of magnitude of exposure, 4.8–120 mR.

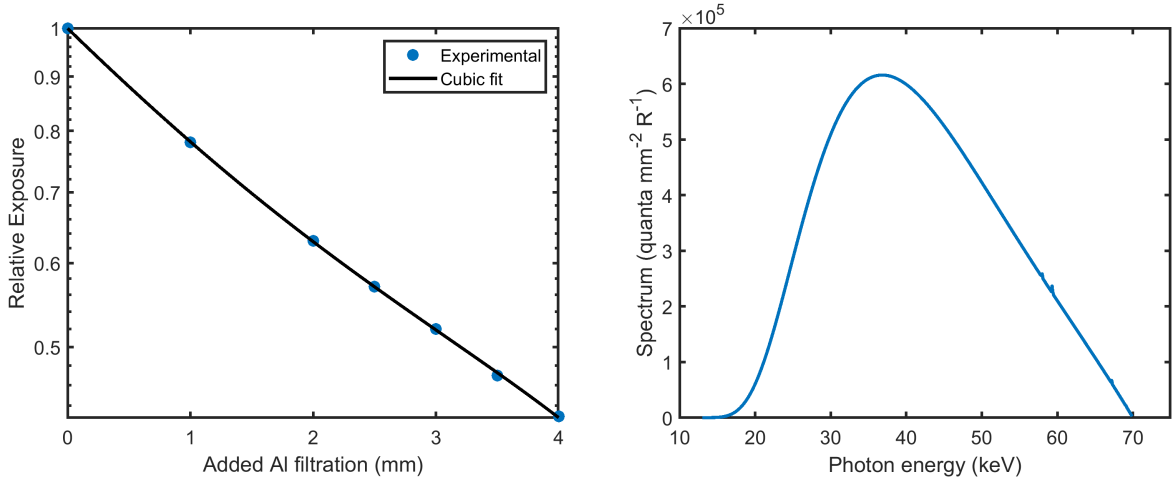

(a) (b)

Figure 7.3: (a) The experimental HVL measured using added aluminum (Al) filtration. (b) The HVL-calibrated semi-empirical spectrum model.

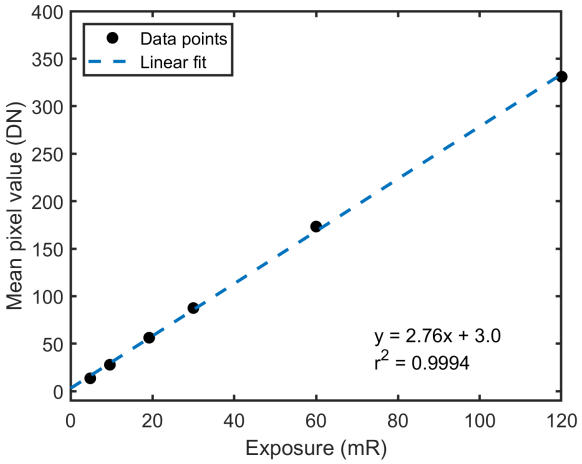

Figure 7.4: (a) The experimental STP measured at 50 kV is linear over two orders of magnitude of exposure.

The slanted-edge technique was verified using a simulated image constructed with 12 degree angle, 5.6 μm pixel blurring, and Poisson noise (Fig. 7.5a). In Fig. 7.5b the slanted-edge MTF is compared to the ideal Fourier-domain pixel sinc-function.

The ESF for the detector prototype (Fig. 7.6b) is generated from an experimental edge image (Fig. 7.6a) with 15.9 degree angle, similar to the angle used in the simulated image. The LSF (Fig. 7.7a) was determined to have a FWHM of 13.4 μm and the MTF (Fig. 7.7b) is demonstrated to degrade by 50% at 32 cycles/mm spatial frequency, corresponding to a 16-μm half-cycle. The experimental MTF does not agree with the theoretical prediction in Fig. 7.7b when photoelectron transport, K-fluorescence re-absorption, and the pixel aperture blurring are taken into account. The relatively large 1 mm focal spot and confined source-to-object distance $z_1 = 46$ cm results in 9.9 μm of penumbral blurring in the object plane. However, with this contribution from geometric unsharpness taken into account, the experimental MTF and adjusted prediction are much closer in agreement.

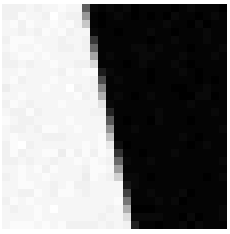

(a)

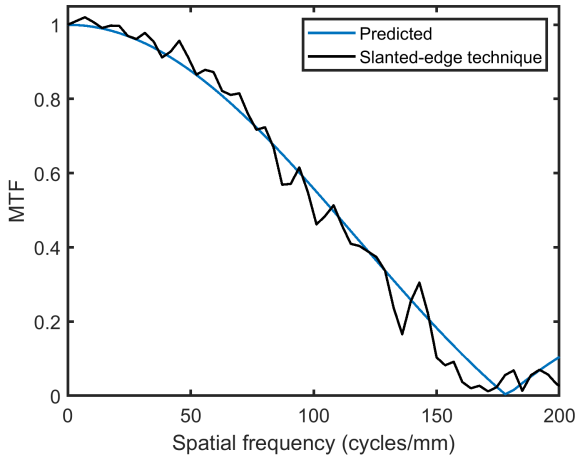

(b)

Figure 7.5: (a) The simulated 28-pixel × 28-pixel edge image. (b) The slanted-edge technique verified using the simulated edge image.

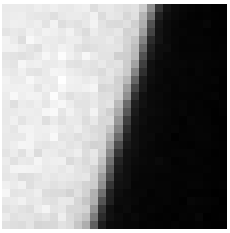

(a)

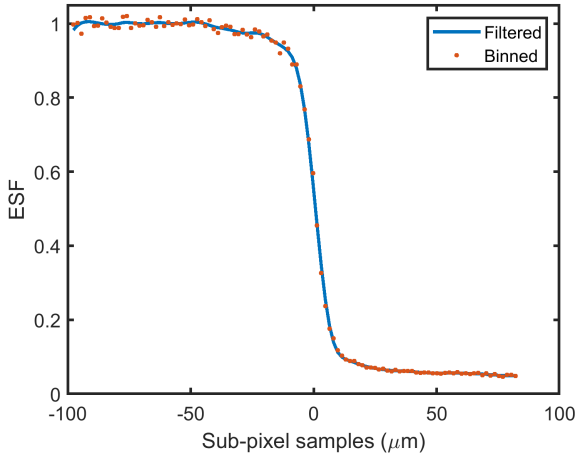

(b)

Figure 7.6: (a) The experimental edge image taken at 70 kV. (b) The experimental ESF normalized to one in the open region.

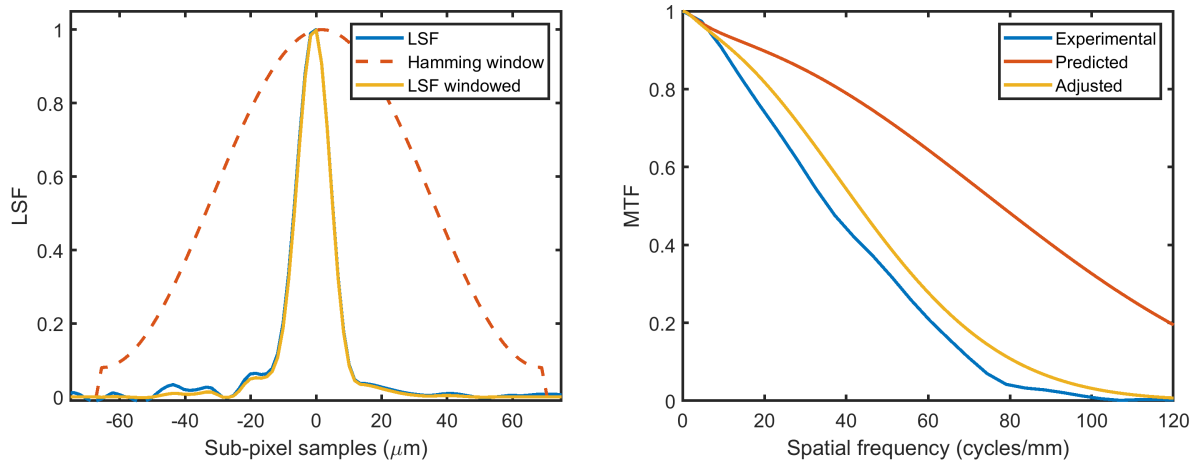

(a) (b)

Figure 7.7: (a) The experimental LSF normalized to one at its peak value. The Hamming window suppresses a small amount of noise. (b) The experimental MTF compared to the prediction with and without adjustment for focal spot blurring.

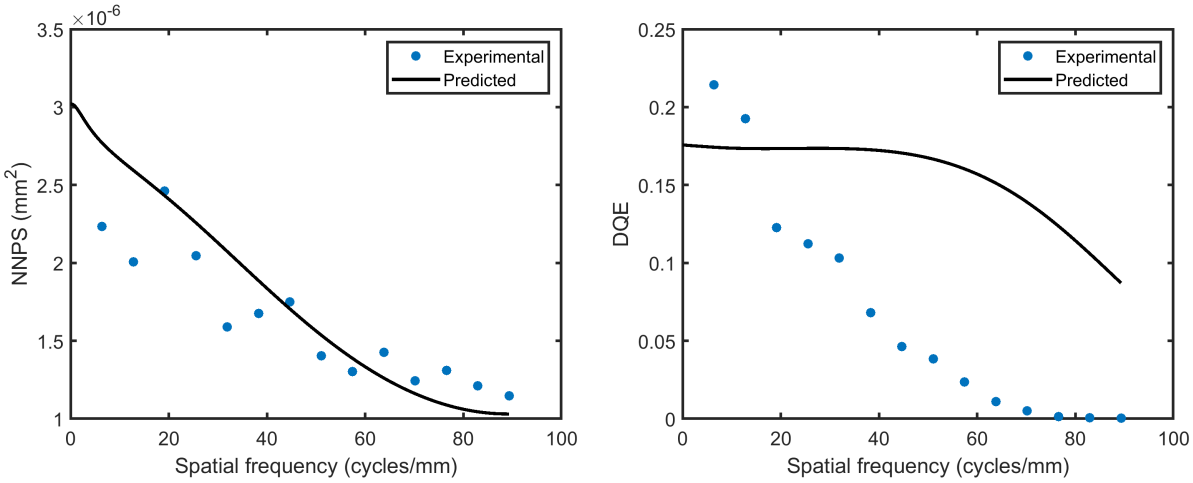

(a) (b)

Figure 7.8: (a) The experimental NNPS at 70 kV. (b) The experimental DQE at 70 kV.

The NNPS for 70 kV is shown in Fig. 7.8a. Agreement with the NNPS prediction using the characterized beam quality was worst at low spatial frequencies. The experimental DQE was lower than predicted at high spatial frequencies due to geometric unsharpness, but it also has significant low spatial frequency error resulting in a DQE values higher than the detector quantum efficiency of 0.20, even when adjusted for Swank noise (Fig. 7.8b).

7.2.3 Discussion

The slanted-edge technique was verified for the 28-pixel × 28-pixel array. Despite this, the experimental MTF was significantly lower than predicted. The discrepancy was determined to be due to the large 9.9 μm penumbral blurring at the object plane. The adjusted prediction using the MTF for geometric unsharpness was much closer in agreement. This suggests an expected improvement in experimental MTF by moving to a small focal spot microfocus source and/or changing the imaging geometry. The remaining deviation in experimental and predicted MTF after adjustment for geometric unsharpness could be from the fact that only the nominal focal spot size is known, the focal spot may not be symmetric, and/or it may not be exactly Gaussian in shape.

The low-frequency error in experimental NNPS is because of the small ROI size. When sampling a limited set of pixels for noise fluctuations there cannot be a good representation of the lowest frequencies, which can only be appreciated with a sufficiently large ROI size. The discrepancy in DQE was then the combination of artificially low measured SNR at low spatial frequencies and the geometric unsharpness at high spatial frequencies, compounded by the fact that the MTF is squared in the DQE calculation.

7.3 Edge-enhancement using simple object geometries

7.3.1 Materials and methods

Imaging apparatus

The imaging system is shown in Fig. 7.9b. The microfocus x-ray source PXS5-927-LV from Thermo Fisher Scientific was operated at 60 kV and 0.134 mA, resulting in a 9 μm focal spot. The source, detector, and linear stage were mounted to an optics rail. The MT1/M-Z8 linear servo stage (Thor Labs Inc.) for lateral object alignment had a minimum 0.05 μm incremental movement, maximum 2.3 mm/s velocity, and 25 mm travel range.

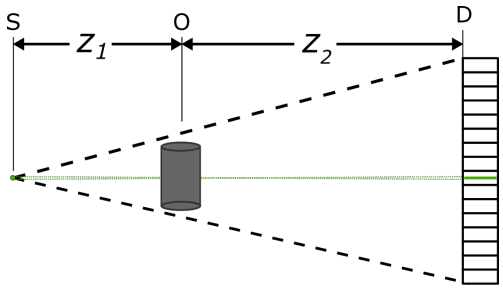

(a)

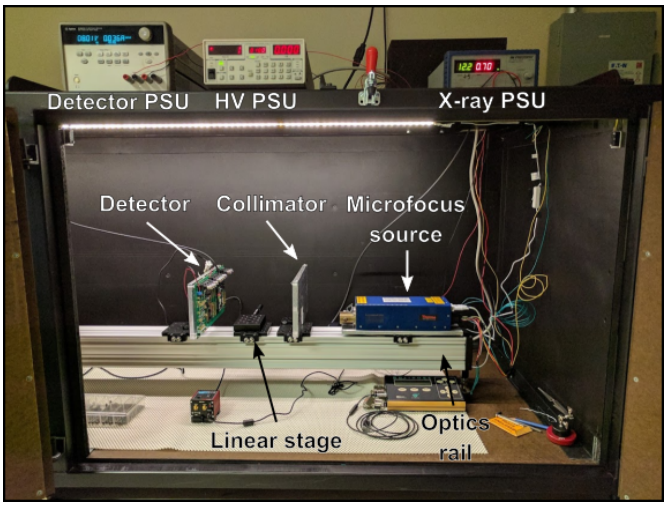

(b)

Figure 7.9: (a) Schematic of the cone-beam imaging geometry (black dashed lines) including the microfocus focal spot (S), object (O), detector (D), and geometric unsharpness or penumbral blurring (green dashed lines). (b) The imaging system comprised detector power supply unit (PSU), high voltage (HV) PSU, X-ray PSU, microfocus source, linear stage, and the AM2 detector prototype.

Phase-contrast imaging

The simple object geometry was a rectangular piece of 3-mm thick Poly(methyl methacrylate), or PMMA. The air-PPMA boundary could be rapidly located using the high frame rate of the CMOS ROIC. The object was scanned laterally at a constant velocity using the linear stage. Frame integration was continuous so motion artifacts occur. However the edge locations and edge-enhancement were clear (Fig. 7.10). Using the edge frame number and the constant stage velocity, the edge was located. The edge itself and surrounding area was imaged by tiling/stitching images together. The source-to-object distance was fixed at $z_1 = 18$ cm to ensure sufficient lateral spatial coherence length for propagation-based edge-enhancement. An integration time of 50 ms and the mean of 100 images were used for each tile.

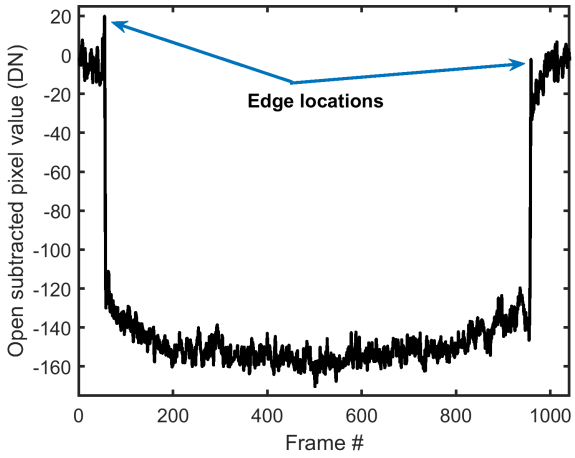

Figure 7.10: Continuous frame integration while the object is scanned laterally to locate the air-PMMA boundary for tiled/stitched imaging.

7.3.2 Results and Discussion

The rectangular geometry PMMA object is shown in Fig. 7.11c. Two magnifications for the tiled images were used: (1) $z_2 = 2$ cm ($M = 1.11$) in Fig. 7.11a, and (2) $z_2 = 8$ cm ($M = 1.44$) in Fig. 7.11b. In both cases edge-enhancement is visible at the air-PMMA

boundary, with a bright/dark fringe width proportional to geometric magnification. The boundary cross-section from summing all image rows is shown in Fig. 7.11d.

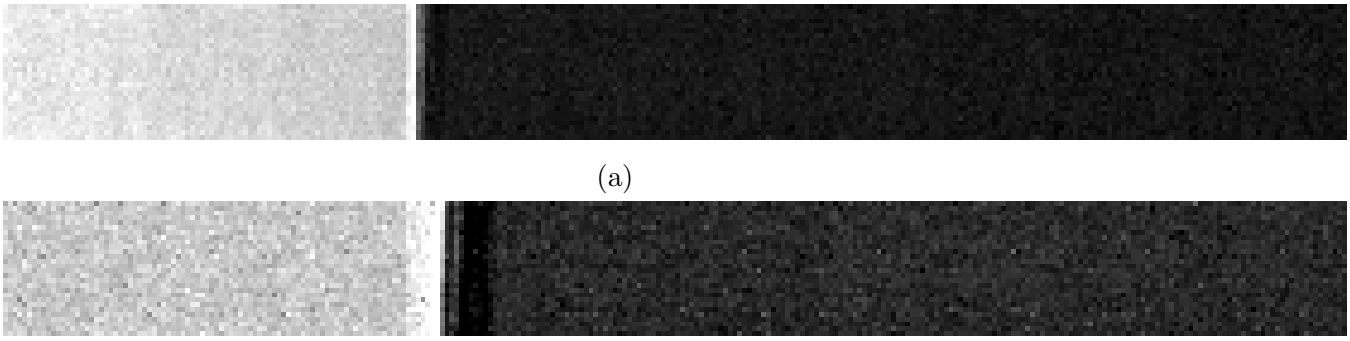

(a)

(b)

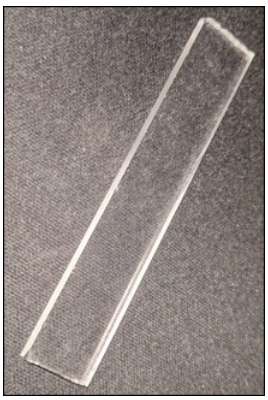

(c)

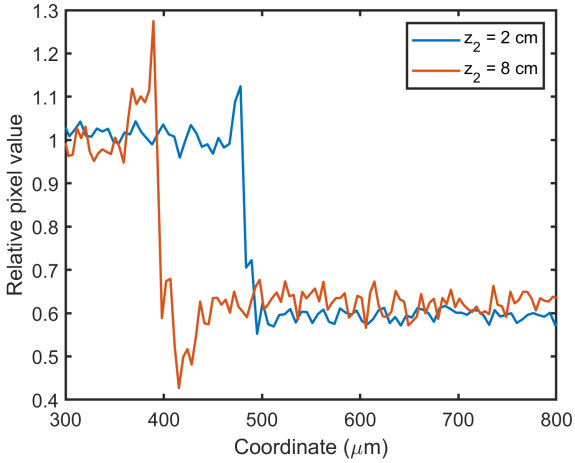

(d)

Figure 7.11: (a) Tiled image of the air-PPMA boundary for $M = 1.11$. (b) Tiled image of the air-PMMA boundary for $M = 1.44$. (c) The 3-mm thick Poly(methyl methacrylate), or PMMA, object. (d) The air-PMMA boundary cross-section.

Chapter 8

LIBRA Detector Project

LIBRA is a distillation of the large imaging area of PITA (Ch. 6), and sub-10 μm pixel pitch of AM2 (Ch. 7). This iteration of hybrid a-Se/CMOS detectors, in collaboration with KA Imaging Inc., uses a one-megapixel array at 7.8 μm pixel pitch. Characterization of signal and noise performance was to be carried out using a microfocus source, facilitated by the scaling to large area. Scaling the imaging area was also, in part, to test the feasibility of commercialization of this technology.

8.1 Back-end processing of the CMOS ROIC

Details of the CMOS ROIC back-end processing are described in Sec. 6.1. The LIBRA detector has the PI layer omitted for simplifying the signal and noise performance characterization. An a-Se layer (Fig. 8.1a) and subsequent gold biasing electrode (Fig. 8.1b) were thermally evaporated with 118 μm and 50 nm layer thicknesses, respectively. The processed CMOS die was then attached and grounded to a ceramic package using silver paste. Taking advantage of the larger array area, the high-voltage connection was provided by a wire suspended from the package to the surface of the gold electrode using silver paste (Fig. 8.1c). Gold-wire (25 μm diameter) ball-bonding was then performed at room temperature, below the glass transition temperature of a-Se, to prevent crystallization. A

maximum biasing voltage of 500 V could be applied to the gold layer, resulting in an a-Se internal electric field in of 4.2 V/μm.

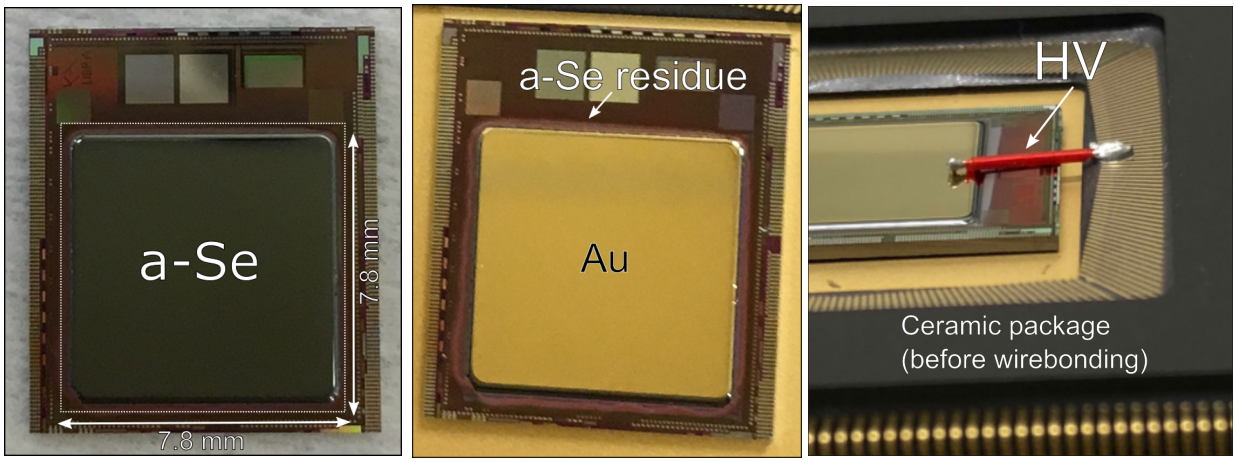

(a) (b) (c)

Figure 8.1: (a) The LIBRA ROIC post a-Se deposition. (b) The LIBRA ROIC post a-Se and gold (Au) deposition. (c) The high voltage (HV) connection attached from pins on the package to the coated die, before wire-bonding.

8.2 Imaging apparatus

The imaging system had a custom horizontal configuration shielded x-ray cabinet with flexible 2 $\times$ 0.86 $\times$ 0.86 m^3 dimensions and was comprised of the microfocus x-ray source, an object holder, the detector prototype, and alignment elements (Fig. 8.2b). The tungsten target PXS5-927-LV microfocus source (Thermo Fisher Scientific) had a variable 20 to 60 kV tube potential, maximum 0.180 mA tube current, and maximum 8 W power output. The focal spot size varies approximately linearly with power from 5 to 9 μm. There was no inherent filtration by the source with the exception of the 254 μm Beryllium window. The optical construction rail supports all elements of the system and allows for easy adjustment of the source-to-object z_1 and object-to-detector z_2 distances in the cone-beam geometry. (Fig. 8.2a). Additions to the system have been made compared to Sec. 7.3.1. Both the

x-ray source and detector have manual lateral and vertical motion control for alignment of the pixel array to the central ray of the source for MTF measurements, and a second linear servo and rotational stage permits vertical and rotational adjustment of the object. Conduit at each end of the cabinet allows for remote computer control of the source, detector, and object alignment during x-ray exposure.

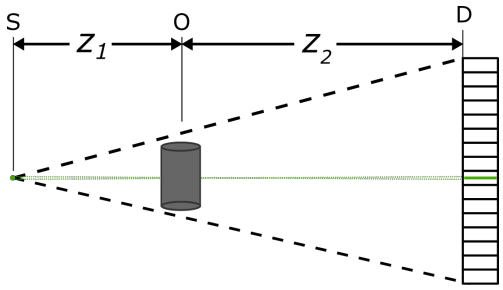

(a)

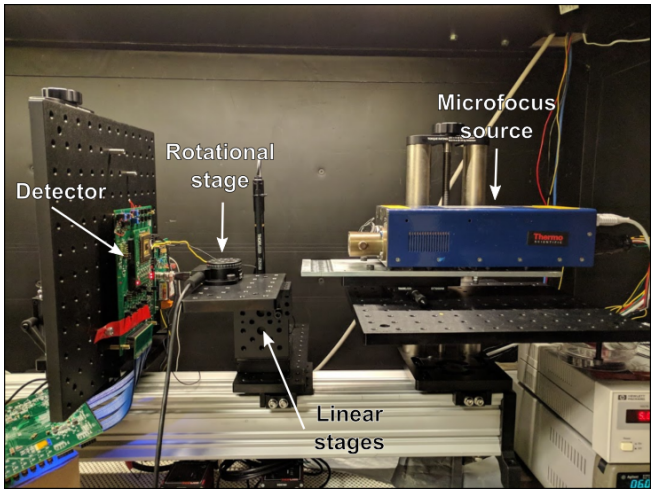

(b)

Figure 8.2: (a) Schematic of the cone-beam imaging geometry (black dashed lines) including the microfocus focal spot (S), object (O), detector (D), and geometric unsharpness or penumbral blurring (green dashed lines). (b) The imaging system is comprised of the microfocus source, alignment stages, and the LIBRA detector prototype.

8.3 Signal and noise performance characterization

8.3.1 Materials and methods

Pixel design

The pixel design features a 61.4 fF integration capacitor with a full-well capacity of 921,000 electrons and a 98 e/DN conversion gain. The dominant readout noise sources include kTC

thermal noise, leakage current shot noise from the pixel electronics, noise from the on-chip buffer, and quantization noise of the off-chip ADC.

X-ray energy spectrum model

During detector characterization measurements a 2 mm Al filter was added to harden the 60 kV beam and remove the tungsten L_α,L_β, and L_γ characteristic lines at 10.2 keV, 11.5 keV, and 12.1 keV, respectively. This permitted modeling the energy spectrum using a semi-empirical model for a the filtered tungsten targets used in radiography [35, 36]. The x-ray intensity aluminum half-value layer (HVL) was measured by adding 0.2 mm Al sheets into the beam and fitting the data of the corresponding drop in intensity. With this estimate of beam quality, the model spectrum was adjusted to match. A photon counter (X-123CdTe Spectrometer, AMPTEK Inc.) was used as a second measurement of the spectral shape.

Signal transfer property

A maximum biasing voltage of 500 V could be applied to the gold layer, resulting in a relatively low a-Se internal electric field of 4.2 V/μm. The detector x-ray sensitivity and linearity was expressed through the signal transfer property (STP). In this way, a selected region-of-interest (ROI) of a number of images were used to determine the mean detector signal at a given exposure. The integration time was held constant and the exposure varied by adjusted the x-ray source tube current.

Modulation transfer function

The pre-sampling MTF was measured using the slanted-edge method. A polished steel edge, shown in Fig. 8.3, was placed at an angle relative to the rows (or columns) to determine an oversampled edge-spread function (ESF). After binning the ESF data to a constant sub-pixel sampling pitch, Savitzky-Golay filtering is used for smoothing. The measured ESF has no imposed function form. The ESF is related to the line-spread function (LSF) using finite differences and subsequently to the MTF by Fourier transform.

Detective quantum efficiency

The spectral decomposition of the noise variance as a function of spatial frequency is given by the Wiener NPS. Images are subdivided into 256-pixel × 256-pixel ROIs with 128 pixel overlap in x and y directions to reduce noise. A total of four million pixels are required by IEC standard to ensure an accuracy of 5%. To determine a one-dimensional cut of the NPS, 7 columns (or rows) on each side of the central axis are averaged. This analysis follows many of the IEC standard guidelines for determining the radiographic DQE [59].

8.3.2 Results

Source characterization

For the purposes of detector characterization, aluminum filter material (2 mm) was added to the intrinsic 60 kV x-ray spectrum in order to be accurately emulated by the semi-empirical spectrum model. The measured half-value-layer (HVL) of the filtered spectrum was 1.69 mm of additional aluminum (Fig. 8.4a) and was used to characterize beam quality and adjust the model to a mean energy of 34.3 keV and a total fluence per unit exposure of 1.28×10^8 mm^{-2} R^{-1}. To supplement this information a photon counter was used to directly measure the energy distribution. The x-ray flux was too high to avoid significant pile-up (30% dead time) and so, because of pile-up rejection, the absolute photon counts were not accurate. However, pile-up rejection minimizes spectral distortion and close agreement in measured spectral shape compared to the model was found (Fig. 8.4b). Using x-ray exposure measurements from a calibrated ionization chamber the entrance SNR of the Poisson distributed x-ray quanta could be determined at the detector plane located 36 cm from the x-ray focal spot.

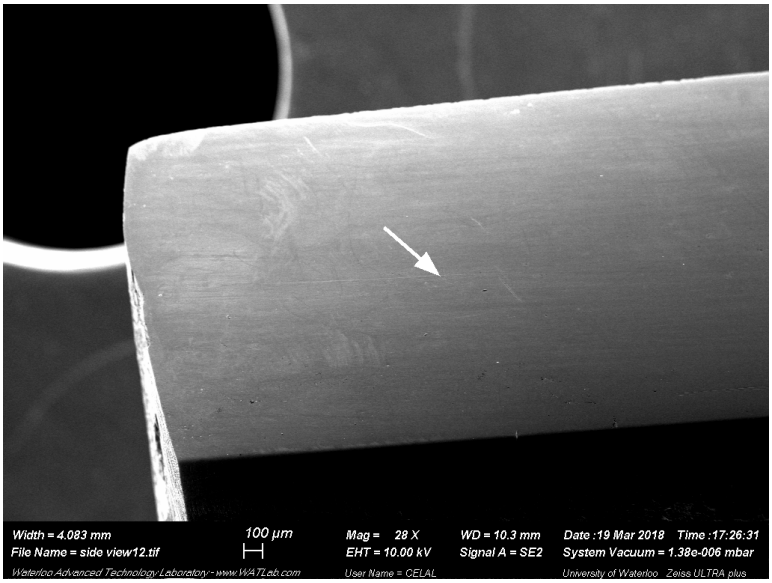

(a)

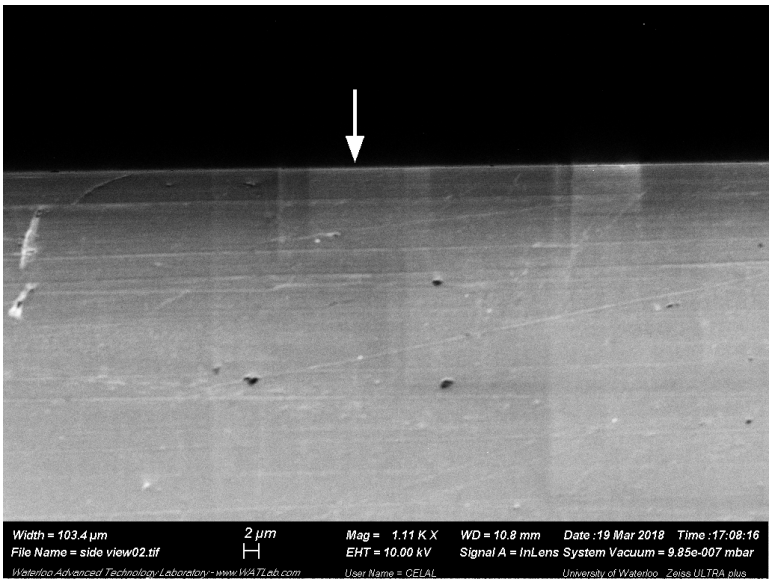

(b)

Figure 8.3: (a) SEM image of the polished steel edge test device. The white arrow indicates the flat edge surface that was used for the slanted-edge technique. (b) SEM showing the edge smoothness. The white arrow indicates the location of the edge line.

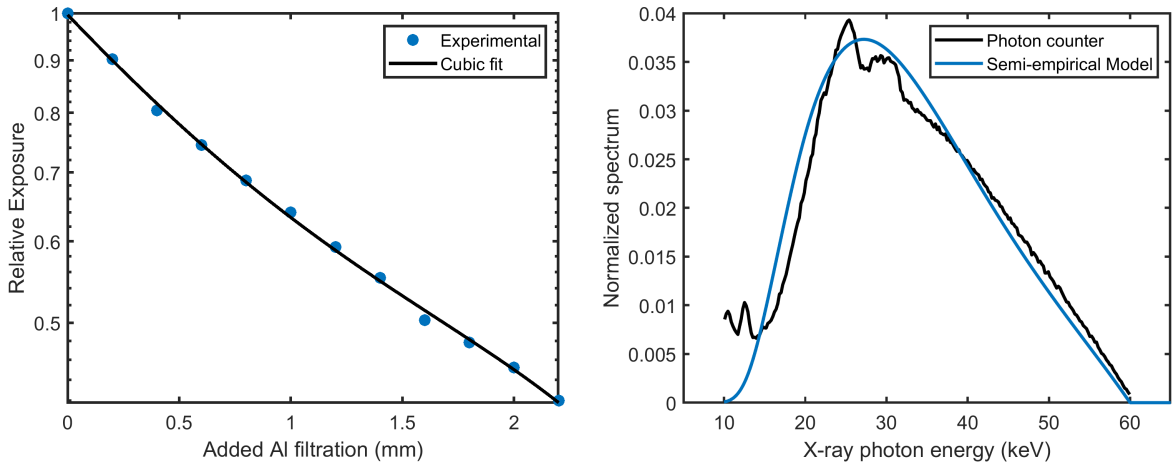

(a) (b)

Figure 8.4: (a) The experimental HVL was 1.69 mm, measured using added aluminum (Al) filtration. (b) The calibrated semi-empirical x-ray energy spectrum model and photon counter data for the 2 mm Al filtered 60 kV beam quality. The mean energy was 34.3 keV, and the total fluence per unit exposure was 1.28×10^8 mm^{-2} R^{-1}.

Detector characterization

The total readout noise was measured to have a standard deviation of approximately 206 electrons for a 2995 ms integration time. The long integration time is used to offset the loss in x-ray intensity from the 2 mm Al filtering. Due to the relatively low electric field the Au/a-Se and Al/a-Se Schottky barrier dark current contributed 50 electrons of noise, 24% of the total readout noise. The attenuated fraction of x-rays by the thickness of a-Se, or quantum efficiency, was calculated to be 0.49. X-ray conversion efficiency was determined by the $W_{\pm}$ of 85 eV per photogenerated electron-hole pair, i.e. 400 electron-hole pairs per 34 keV photon.

The STP was obtained by plotting the mean pixel value in a 500-pixel × 900-pixel ROI from 15 images, against the measured exposure, using the fixed 2995 ms integration time. Fig. 8.5 shows the detector signal transfer was linear over the available x-ray exposure range of 9.4 to 23.7 mR with a coefficient of determination (r^2) of 0.9957.

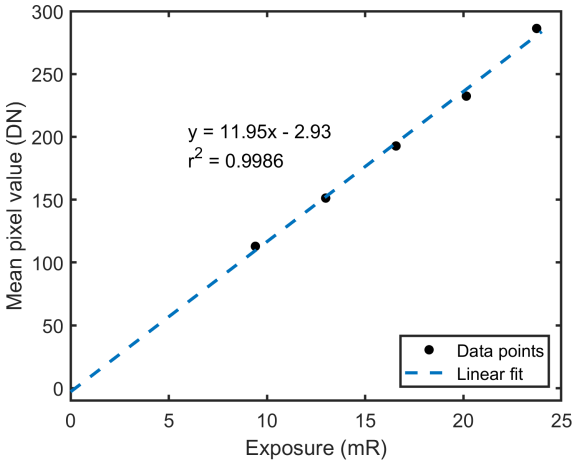

Figure 8.5: The STP measured over exposure range used for the experimental NPS and DQE. The signal transfer linearity is shown by least-squares regression with a coefficient of determination (r^2) of 0.9957.

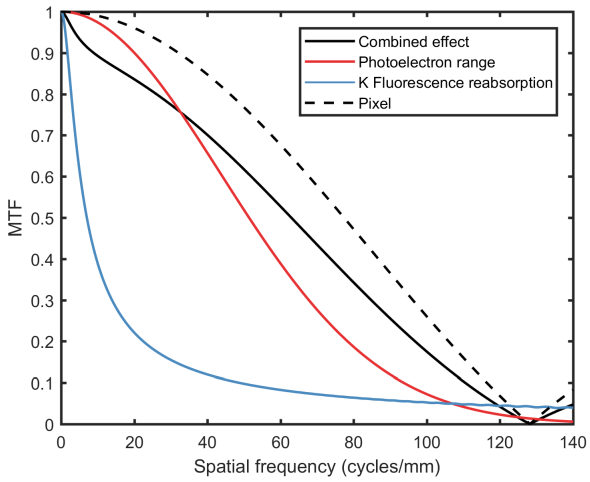

Figure 8.6: The theoretical MTF prediction using the cascaded systems model. The combined MTF is compared to contributions from the pixel, the primary photoelectron range, and K-fluorescence re-absorption.

Based on relative energy deposition, blurring caused by x-ray interactions with a-Se is dominated by the primary photoelectron range and the re-absorption of K-fluorescent photons (Fig. 5.3). In the cascade model the MTF of these two processes are combined as an energy-weighed sum before blurring due to the extent of the pixel aperture. The MTF of the individual processes, and combined effect (Fig. 8.6) show that based on energy deposition we expect a drop in MTF at lower frequencies (<20 cycles/mm) due to K-fluorescence re-absorption and at higher spatial frequencies the overall MTF envelope is governed by the path length of the primary photoelectron and the pixel size.

Using the slanted-edge technique (Fig. 8.7a) the pre-sampling MTF of the detector was measured. The ESF was effectively oversampled (i.e. sub-pixel sampled) by a factor of 3.3 and binned into a regular sampling pitch equal to 10% of the physical pixel pitch (Fig. 8.7b). The oversampling rate is sufficient to avoid aliasing and determine the pre-sampling MTF. The corresponding LSF had a full-width at half-maximum (FWHM) of approximately 8.7 μm (Fig. 8.8a). In the Fourier-domain we see that, as expected, there is a low-frequency drop due to K-fluorescence reabsorption and a zero near the first sinc-function zero at a spatial frequency equal to the inverse of the pixel pitch. The MTF drops to 50% at 45 cycles/mm corresponding to an 11 μm half-cycle and there is close agreement to the theoretical MTF prediction based on relative energy deposition (Fig. 8.8b).

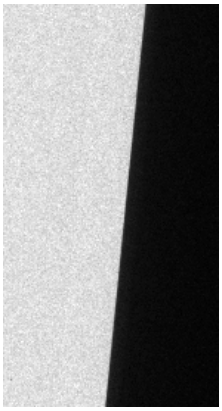

(a)

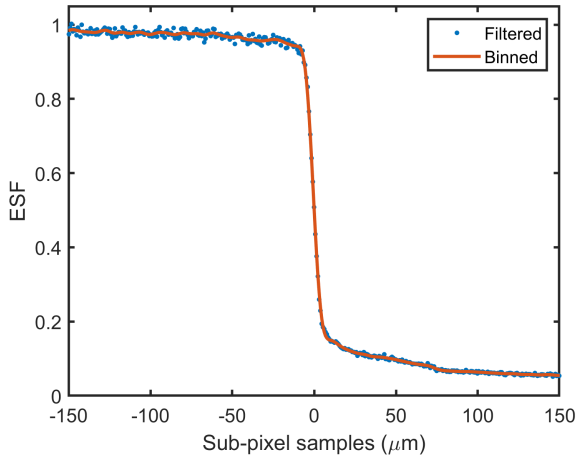

(b)

Figure 8.7: (a) The edge image with 146-pixel $\times$ 274-pixel ROI. (b) The experimental ESF normalized to one in the open region.

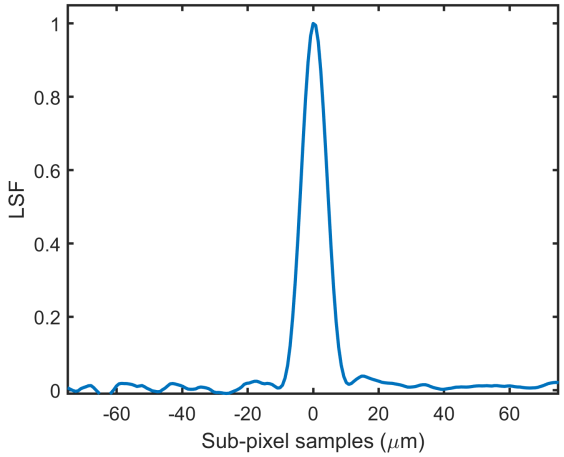

(a)

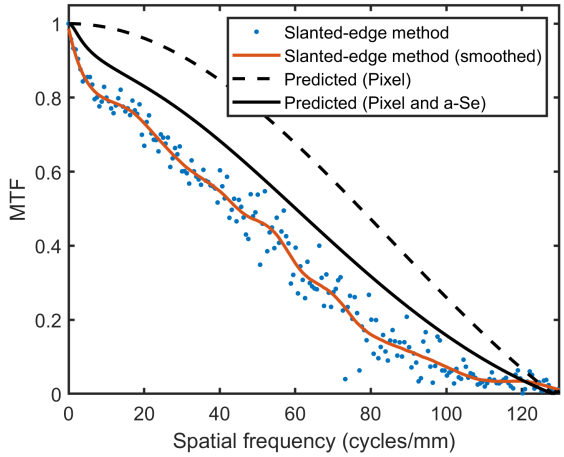

(b)

Figure 8.8: (a) The experimental LSF normalized to one at its peak value. (b) The experimental pre-sampling MTF using the slanted-edge technique compared to the pixel on its own, as well as including all contributions from a-Se.

The NPS was measured using a total of 450 standard 256-pixel × 256-pixel ROIs. One-dimension cuts from the two-dimensional NPS are shown in Fig. 8.9a after normalization by the signal power. A drop in NPS with frequency, approximately 50%, is evident.

Using the measured MTF and NPS results, along with the HVL-calibrated spectrum model and exposure measurements, the DQE was calculated (Fig. 8.9b). The theoretical upper bound on the DQE at zero spatial frequency is equal to the product of the quantum efficiency (0.49) and the Swank factor (approximately 0.9 at 30 keV [48]). Therefore, we then expect a DQE(0) of approximately $0.49 \times 0.9 = 0.45$. The experimental DQE has a DQE(0) of approximately 0.42, lower than the quantum efficiency due to Swank noise and the additional factors from the detection process. This is also the case from the cascaded systems model which predicts a DQE(0) of 0.45. At the pixel sampling Nyquist frequency, the experimental DQE decreases to 0.1.

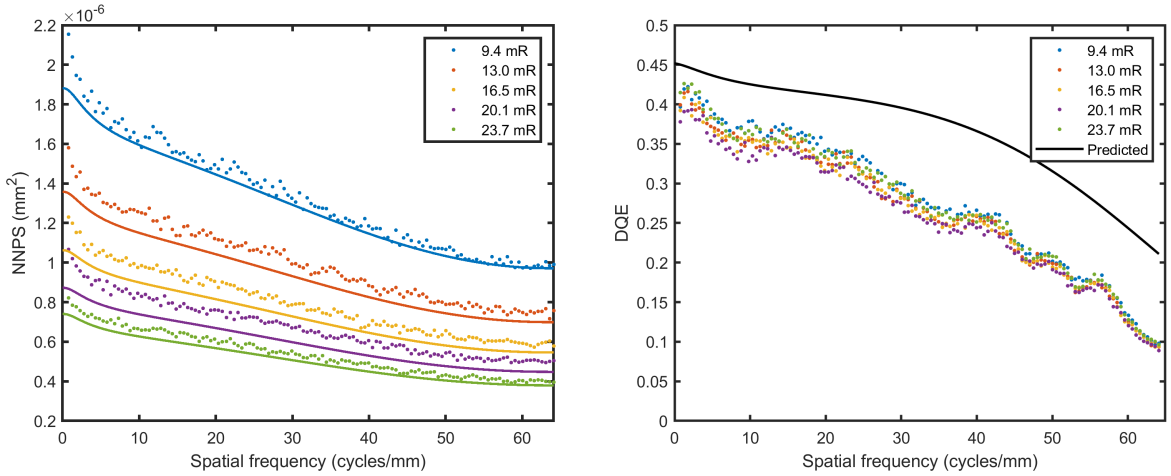

(a) (b)

Figure 8.9: (a) One-dimensional cuts of the experimental NNPS (dots) and predicted NNPS (lines) from the cascaded systems model. (b) The experimental DQE (dots) and predicted DQE (black line) from the cascaded systems model .

8.3.3 Discussion

The measured DQE indicates that the fraction of photons used effectively by the detector, i.e. the equivalent quantum efficiency, was 0.42. That is, under the same beam quality an ideal detector with 42% quantum efficiency would produce identical image SNR. The DQE was essentially unchanged with exposure between 9.4 to 23.7 mR which means the detector was photon quantum noise limited with the CMOS readout noise being negligible. The discrepancy of the experimental DQE compared to the cascaded systems model is potentially due alignment error of the detector, or yet to be understood losses in charge collection efficiency.

The detector spatial resolution was characterized both by an 8.7 μm FWHM of the LSF, and by a 50% MTF at an 11 μm half-cycle (45 cycles/mm) in the Fourier-domain. These dimensions are on the order of the pixel pitch. This suggests that the primary photoelectron and reabsorbed K-fluorescent photons do not generate charge carriers in a volume with a spread in the pixel plane much greater than a single pixel. This is further indicated by the measured NPS showing non-white, correlated noise.

The combination of spatial resolution and detection efficiency demonstrated by the a-Se/CMOS prototype is unique compared to conventional high resolution scintillator-based detectors. For example, thin Gd_2O_2S:Tb scintillators (15 μm) have a quantum efficiency of only 0.13 at the same beam quality and coupling to a CMOS ROIC with a similar pixel pitch as LIBRA results in a more broad LSF, 27 μm FWHM [96, 97, 98]. Another example is YAG:Ce scintillator-based detectors. Mittone *et al.* demonstrated a 350 μm thick YAG:Ce scintillator coupled to 6.5 μm pixel pitch, and for 35 keV the performance was 50% MTF at 25 cycles/mm, and a DQE(0) of 0.32 [99].

The signal and noise performance of the a-Se/CMOS detector, compared to state-of-the art high resolution scintillated-based detectors, suggests the possibility to further extend application of phase-contrast imaging for radiation sensitive life science and biomedical applications by rapid and efficient acquisition of high spatial resolution phase-contrast data.

The a-Se/CMOS detector DQE can be optimized by adjusting the thickness of the a-Se photoconductor to satisfy a range imaging tasks. While the spread of absorbed energy in

a-Se has little dependence on the photoconductor thickness, incident x-ray obliquity from beam divergence, similarly for scintillators, is an additional source of blurring that does depend on indirect/direct converter thickness. Thus, depending the desired beam quality and angle subtended by the detector, the a-Se layer can be optimized in terms of MTF and DQE.

8.4 Phase-contrast imaging

To observe the impact of edge-enhancement from propagation-based phase-contrast, a sample bell pepper seed was imaged using a source-to-object distance $z_1 = 18$ cm to ensure sufficient transverse spatial coherence length using a 9 μm focal spot size. In order to minimize phase-contrast the propagation distance was first limited to $z_2 = 1$ cm, the practical lower limit for the detector. The propagation distance was then increased to $z_2 = 8$ cm. The geometric magnification was $M = 1.05$, and $M = 1.44$, respectively. Some detail may improve from the increased magnification, however feature detectability due to edge-enhancement is clear from Fig. 8.10. Images are displayed as a "negative" (i.e. brighter regions correspond to lower object x-ray transmission). No source filtration was used.

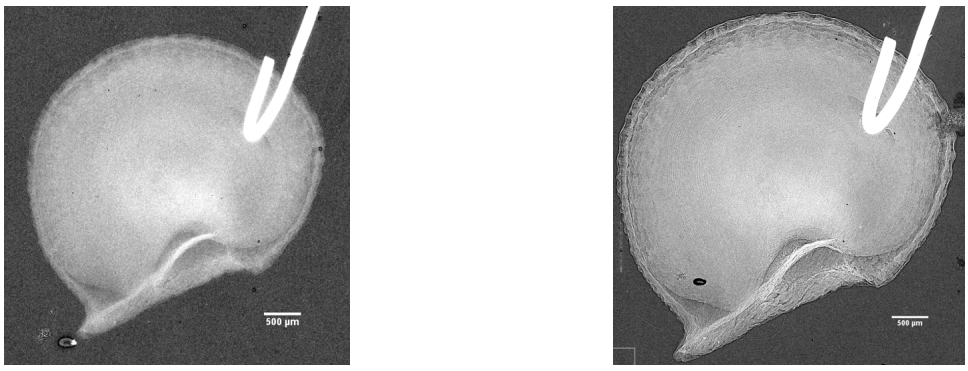

(a) (b)

Figure 8.10: (a) A sample bell pepper seed with minimized edge-enhancement by limiting the propagation distance to $z_2 = 1$ cm. (b) Edge-enhancement emphasized by increasing the propagation distance to $z_2 = 8$ cm.

The very bright wire hook in the image was used to suspend the sample. Image artifacts present are due to back-end processing defects. Some radiation damage may also be present as the CMOS was not radiation hardened, and the a-Se layer was not sufficiently thick to attenuate all x-rays. The edge-enhancement detail is showcased more clearly in Fig. 8.11 using another bell pepper seed sample.

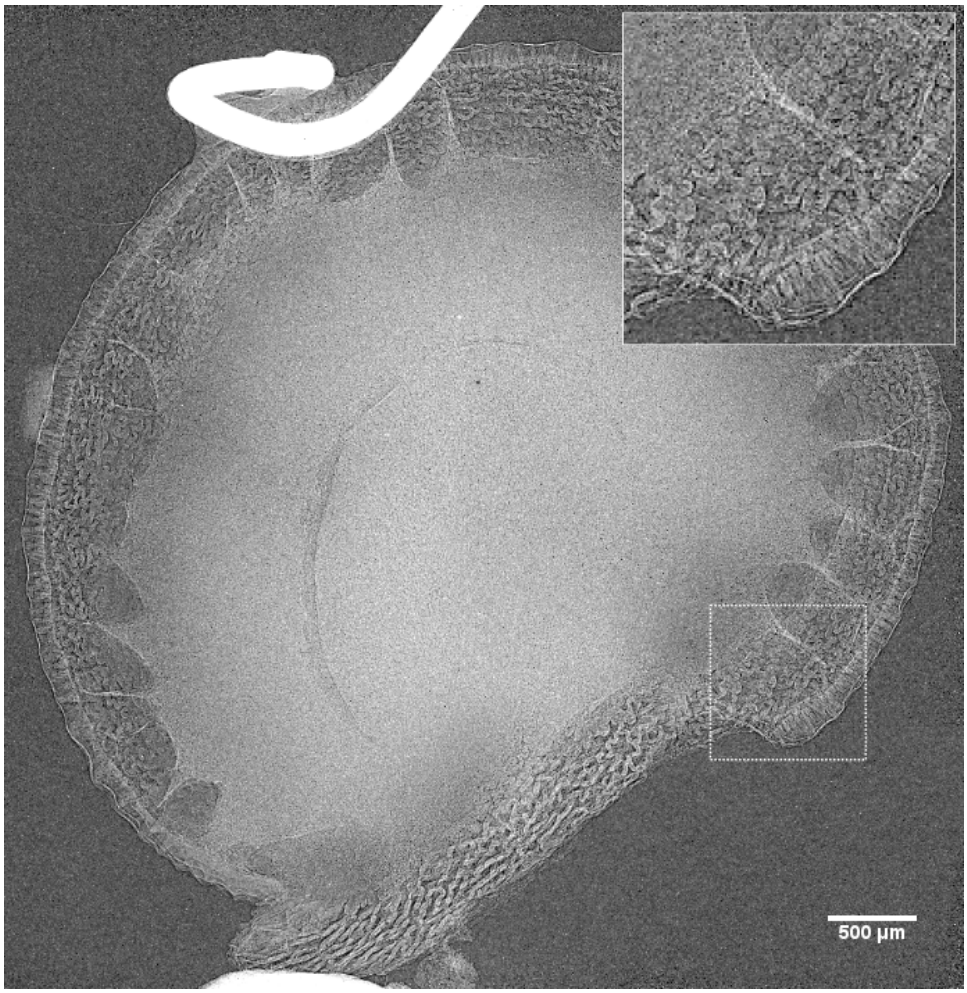

Figure 8.11: A sample bell pepper seed image taken at 60 kV using 0.076 mAs ($z_1 = 18$ cm, $z_2 = 8$ cm, $M = 1.44$). The region inside the dashed line is shown magnified at the top right.

This phase-contrast imaging was applied to an excised mouse stifle joint (equivalent to the knee joint in humans) with the intention of visualizing articular cartilage using edge-enhancement. Because articular cartilage is the low coefficient of friction thin layer coating the ends of bones where they come together as joints, the ability to make quantitative assessments using animal models (i.e. a non-human species studied to understand biological phenomenon that may also provide insight for humans) is extremely important for investigating the progression of diseases such as osteoarthritis [100]. Cartilage notoriously lacks absorption-contrast and is therefore conventionally "x-ray transparent," and magnetic resonance imaging (MRI) does not possess sufficient spatial resolution to assess a mouse model.

The imaging parameters were set as 60 kV, 0.21 mAs, and $z_1 = z_2 = 18$ cm ($M = 2$). An off-angle (i.e. not a typical lateral or posterior/anterior) view of the femur and patella is shown in Fig. 8.13, and the articular cartilage is visible. Trabecular bone detail and the patellar ligament can also be seen. For reference, refer to Fig. 8.12. The image scale indicates an articular cartilage thickness less than 100 μm, consistent with measurements using an x-ray opaque contrast agent and a commercial micro computed tomography system [101]. A pseudo posterior/anterior view is shown in Fig. 8.14. In this case the meniscus (i.e the "shock-absorber" of the stifle joint) is visible.

The results from the hybrid a-Se/CMOS detector prototype demonstrate rapid, high spatial resolution phase-contrast imaging in compact geometries using high DQE. The images exhibit intrinsic propagation-based edge-enhancement, i.e. there is sufficient transverse spatial coherence and propagation distance that Fresnel diffraction is observed. No optical elements are used. The visualization of articular cartilage in the mouse stifle joint is particularly promising.

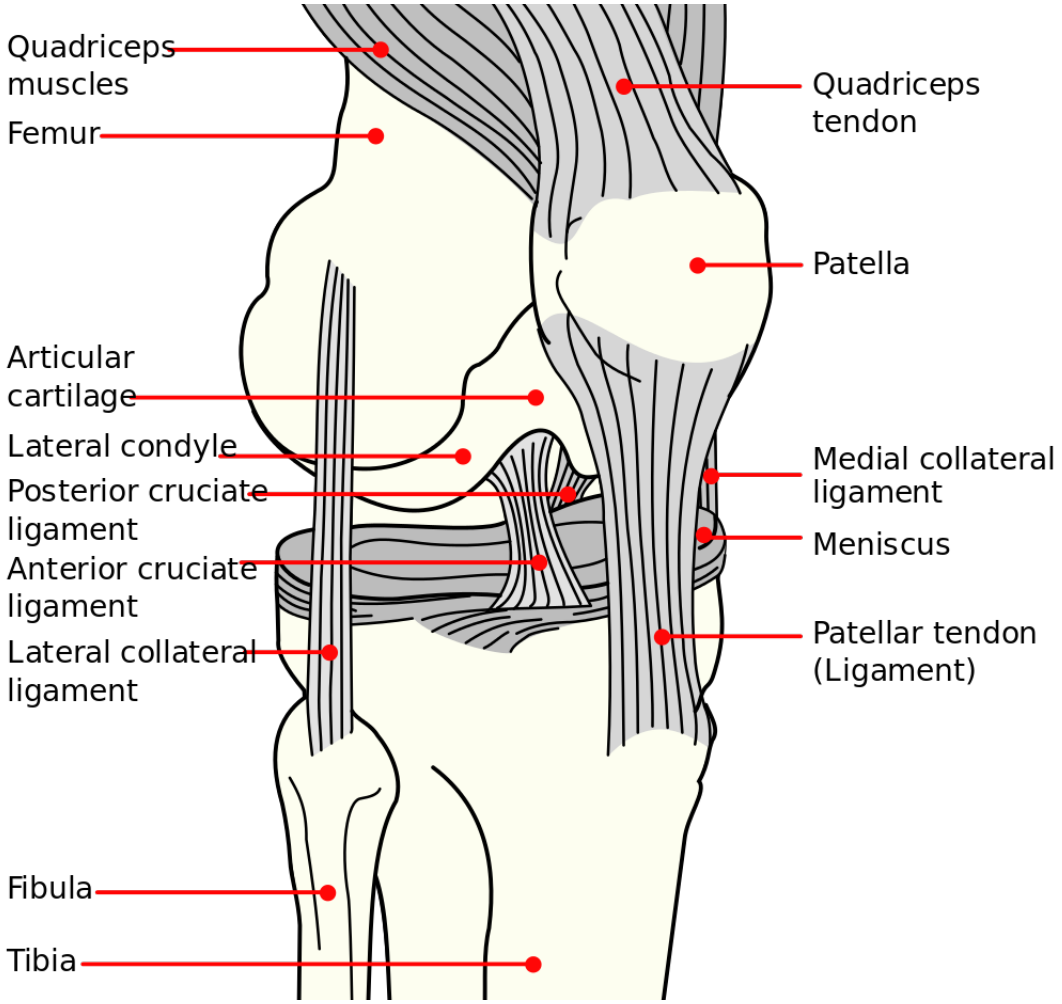

Figure 8.12: A reference knee joint for aid in interpreting the phase-contrast images of the mouse stifle joint (equivalent to the knee joint in humans). From [102].

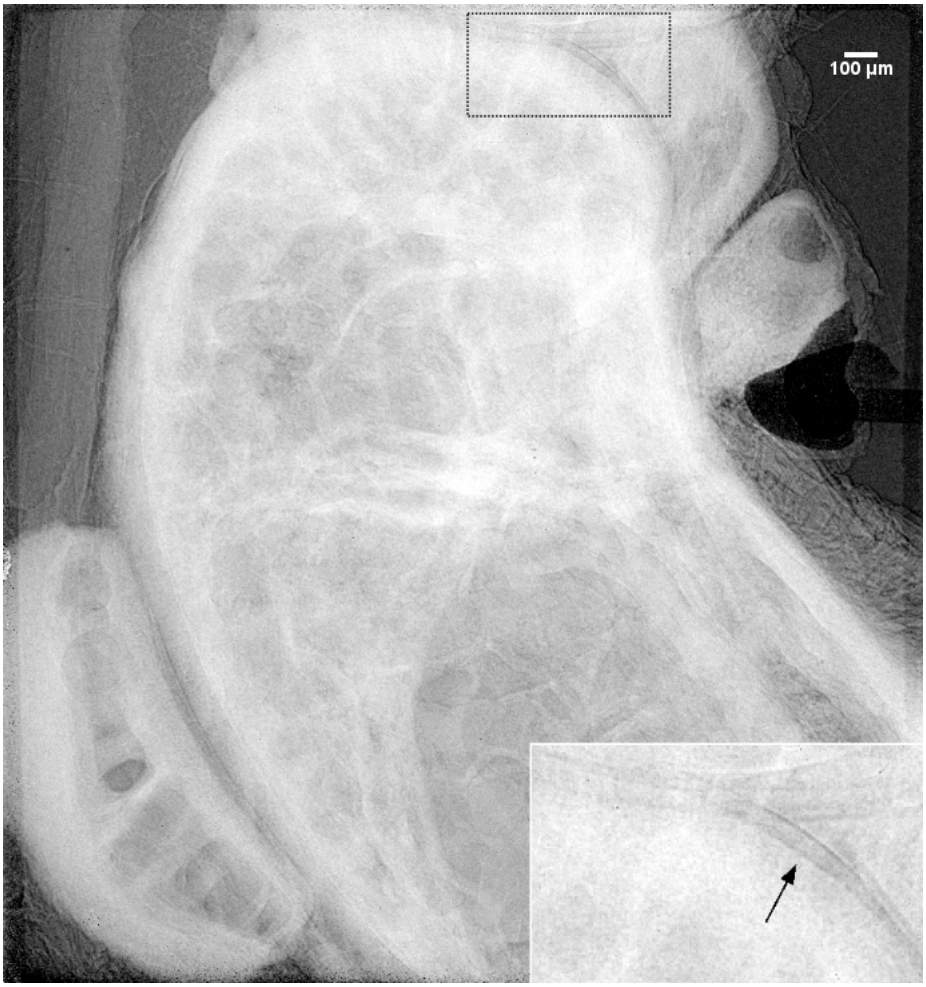

Figure 8.13: Articular cartilage, patellar tendon, and trabecular bone detail of the mouse stifle joint. The region inside the dashed line is shown magnified at the bottom right. Articular cartilage, delineated by edge-enhancement, is indicated by the black arrow. The image was taken at 60 kV using 0.21 mAs.

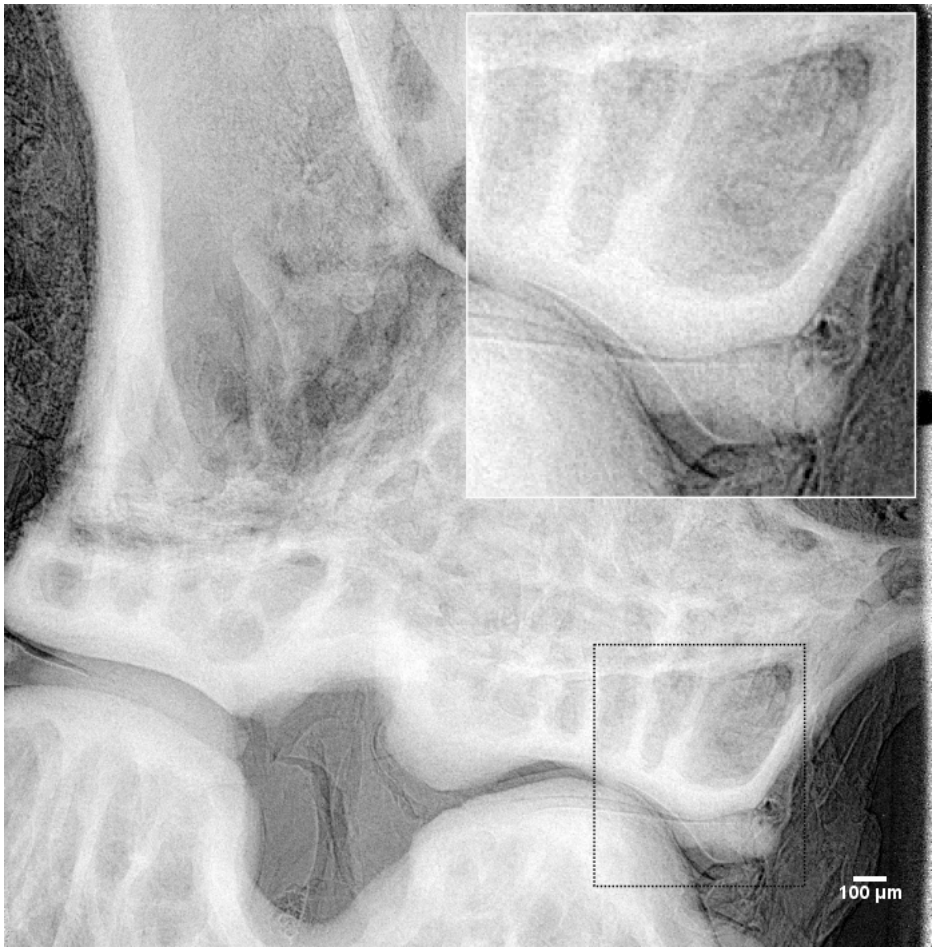

Figure 8.14: Meniscus and trabecular bone detail of a mouse stifle joint. The region inside the dashed line is shown magnified at the top right. The image was taken at 60 kV using 0.21 mAs.

Chapter 9

Conclusions, Contributions, and Future Work

9.1 Conclusions

This thesis has developed hybrid semiconductor x-ray detectors using a direct-conversion approach with photoconductive amorphous selenium (a-Se) and complementary metal-oxide-semiconductor (CMOS) readout integrated circuits. Three unique prototypes employing the a-Se/CMOS detector technology were fabricated and characterized. The first prototype, with 1.6×1.6 cm^2 field-of-view (FOV) and 25 μm pixel pitch, was an initial validation of the fabrication process and high spatial resolution absorption-contrast imaging. The second prototype, with 0.18×0.20 cm^2 FOV and 5.6 μm pixel pitch, demonstrated edge-enhancement for simple objects in compact geometries using a microfocus source. The third and current generation prototype, with 7.8×7.8 cm^2 FOV and 7.8 μm pixel pitch, was the culmination of large imaging area and small pixel pitch, permitting complete characterization by Fourier-based metrics of performance, including the modulation transfer function, noise power spectrum, and detective quantum efficiency (DQE), using a microfocus source.

The a-Se/CMOS detector prototypes demonstrated a unique combination of high spa-

tial resolution and high detection efficiency for hard x-rays. In fact, the measured spatial resolution in each case was one of the highest, if not *the* highest reported, including the first physical demonstration of an a-Se detector with charge carrier spreading larger than the pixel size. The experimental results were successfully compared to predictions using cascaded systems theory, and the resulting theoretical model can be applied to further optimize a-Se/CMOS detectors for specific imaging tasks.

Employing the third generation prototype, fast biomedical phase-contrast x-ray imaging in compact geometries was demonstrated using a microfocus source. The articular cartilage in a mouse stifle joint was delineated using edge-enhancement, offering the possibility to study diseases such as osteoarthritis. This implementation of the propagation-based phase-contrast technique suggests that high DQE hybrid semiconductor technology offers the potential to fill the large performance deficit in high spatial resolution scintillator-based detectors for phase-contrast x-ray imaging.

9.2 Contributions

The original contributions of this work to the development of x-ray detectors and phase-contrast x-ray imaging are summarized below:

- Development of a hybrid semiconductor detector fabrication process for large-area compatible vertical integration of a-Se with CMOS by back-end processing.
- Characterization of a-Se/CMOS detector performance by measuring the modulation transfer function, noise power spectrum, and detective quantum efficiency using a microfocus source.
- Development of the highest spatial resolution x-ray detector for hard x-rays.
- The first physical demonstration of an a-Se direct-conversion detector with charge carrier spreading larger than the pixel pitch.
- Demonstration of propagation-based phase-contrast x-ray imaging in compact geometries using a direct-conversion detector.

- Demonstration of propagation-based phase-contrast x-ray imaging in the inverse geometry, where the object-to-detector distance is smaller than the source-to-object distance, using a direct-conversion detector and microfocus source.

- Commercialization, in collaboration with KA Imaging Inc., of an x-ray micro computed tomography system based on the a-Se/CMOS detector technology developed in this work.

Journal publications

- Michal J. Wesolowski, Christopher C. Scott, Benjamin Wales, Ali Ramadhan, Sahr Al-Tuairqi, Surajith N. Wanasundara, Karim S. Karim, Joseph H. Sanderson, Carl A. Wesolowski, and Paul S. Babyn. "X-Ray Dosimetry During Low-Intensity Femtosecond Laser Ablation of Molybdenum in Ambient Conditions." IEEE Transactions on Nuclear Science 64, no. 9 (2017).

- Alireza Parsafar, Christopher C. Scott, Abdallah El-Falou, Peter M. Levine, and Karim S. Karim. "Direct-Conversion CMOS X-Ray Imager with 5.6 μm $\times$ 6.25 μm Pixels." IEEE Electron Device Letters 36, no. 5 (2015).

- Shiva Abbaszadeh, Christopher C. Scott, Oleksandr Bubon, Alla Reznik, and Karim S. Karim. "Enhanced detection efficiency of direct conversion X-ray detector using polyimide as hole-blocking layer." Scientific Reports 3 (2013).

- Nicholas Allec, Shiva Abbaszadeh, Chris C. Scott, Karim S. Karim, and John M. Lewin. "Evaluating noise reduction techniques while considering anatomical noise in dual-energy contrast-enhanced mammography." Medical Physics 40, no. 5 (2013).

- N. Allec, S. Abbaszadeh, C. C. Scott, J. M. Lewin, and K. S. Karim. "Including the effect of motion artifacts in noise and performance analysis of dual-energy contrast-enhanced mammography." Physics in Medicine & Biology 57, no. 24 (2012).

Conference publications

- Tomi F. Nano, Christopher C. Scott , Yunzhe Li, Celal Con, Karim S. Karim, Ian A. Cunningham. "Performance evaluation of a Se/CMOS prototype x-ray detector with the apodized aperture pixel (AAP) design." In Medical Imaging: Physics of Medical Imaging. International Society for Optics and Photonics, 2019.

- M. Russ, Alok Shankar, Amit Jain, Swetadri V. S. Nagesh, Ciprian N. Ionita, Christopher C. Scott, Karim S. Karim, Daniel R. Bednarek, and Stephen Rudin. "Quantitative comparison using Generalized Relative Object Detectability (G-ROD) metrics of an amorphous selenium detector with high resolution Microangiographic Fluoroscopes (MAF) and standard flat panel detectors (FPD)." In Medical Imaging: Physics of Medical Imaging, vol. 9783. International Society for Optics and Photonics, 2016.

- Christopher C. Scott, Alireza Parsafar, Abdollah El-Falou, Peter M. Levine, and Karim S. Karim. "High dose efficiency, ultra-high resolution amorphous selenium/CMOS hybrid digital X-ray imager." In Electron Devices Meeting (IEDM), 2015 IEEE International. IEEE, 2015.

- Christopher C. Scott, Shiva Abbaszadeh, Sina Ghanbarzadeh, Gary Allan, Michael Farrier, Ian A. Cunningham, and Karim S. Karim. "Amorphous selenium direct detection CMOS digital x-ray imager with 25 micron pixel pitch." In Medical Imaging 2014: Physics of Medical Imaging, vol. 9033. International Society for Optics and Photonics, 2014.

- Chris C. Scott, Nicholas Allec, and Karim S. Karim. "A study of factors limiting spatial resolution using a 25 micron pixel pitch direct-detection amorphous selenium imaging system." In Medical Imaging: Physics of Medical Imaging, vol. 8313. International Society for Optics and Photonics, 2012.

9.3 Future work

The natural extension of this thesis is application of the developed hybrid semiconductor x-ray detector technology to three-dimensional imaging via slices by tomographic reconstruction [103]. Referred to as *micro* computed tomography (μCT), the object is rotated about a single axis and a number of projection images are acquired in the cone-beam geometry [104, 105]. The speed and total length of the acquisition means the detector temporal performance is critical and the detective quantum efficiency is no longer the sole metric of interest. In terms of temporal performance, image lag refers to the influence of residual signals from previous images on the current image. Divided into two components [59], additive lag (i.e. change in detector offset), and multiplicative lag or ghosting (i.e. change in detector sensitivity), can be problematic for μCT reconstruction [106]. Investigation and implementation of detector blocking layers [75, 87, 107] and other techniques [108] to control lag is necessary.

Compared to absorption-contrast, x-ray imaging using propagation-based phase-contrast can enable higher contrast from poorly absorbing objects due edge enhancement. However, the tomographic reconstruction of such edge enhanced image data can result in artifacts [98]. Flexible and efficient methods of phase-retrieval [93, 109] from polychromatic microfocus sources must be investigated to, when necessary, separate the phase and amplitude information prior to reconstruction.

References

[1] T. J. Davis, D. Gao, T. E. Gureyev, A. W. Stevenson, and S. W. Wilkins. Phase-contrast imaging of weakly absorbing materials using hard x-rays. *Nature*, 373(6515):595, 1995.

[2] David Paganin. *Coherent X-ray optics*. Number 6. Oxford University Press on Demand, 2006.

[3] V. N. Ingal and E. A. Beliaevskaya. X-ray plane-wave topography observation of the phase contrast from a non-crystalline object. *Journal of Physics D: Applied Physics*, 28(11):2314, 1995.

[4] U. Bonse and M. Hart. An x-ray interferometer. *Applied Physics Letters*, 6(8):155–156, 1965.

[5] Atsushi Momose, Tohoru Takeda, Yuji Itai, and Keiichi Hirano. Phase–contrast x–ray computed tomography for observing biological soft tissues. *Nature medicine*, 2(4):473–475, 1996.

[6] Franz Pfeiffer, Timm Weitkamp, Oliver Bunk, and Christian David. Phase retrieval and differential phase-contrast imaging with low-brilliance x-ray sources. *Nature physics*, 2(4):258, 2006.

[7] Alessandro Olivo and Robert Speller. A coded-aperture technique allowing x-ray phase contrast imaging with conventional sources. *Applied Physics Letters*, 91(7):074106, 2007.

[8] S. W. Wilkins, T. E. Gureyev, D. Gao, A. Pogany, and A. W. Stevenson. Phase-contrast imaging using polychromatic hard x-rays. *Nature*, 384(6607):335, 1996.

[9] A. Snigirev, I. Snigireva, V. Kohn, S. Kuznetsov, and I. Schelokov. On the possibilities of x-ray phase contrast microimaging by coherent high-energy synchrotron radiation. *Review of scientific instruments*, 66(12):5486–5492, 1995.

[10] Peter Cloetens, Raymond Barrett, José Baruchel, Jean-Pierre Guigay, and Michel Schlenker. Phase objects in synchrotron radiation hard x-ray imaging. *Journal of Physics D: Applied Physics*, 29(1):133, 1996.

[11] Tomi Tuohimaa, Mikael Otendal, and Hans M. Hertz. Phase-contrast x-ray imaging with a liquid-metal-jet-anode microfocus source. *Applied Physics Letters*, 91(7):074104, 2007.

[12] Johannes Wenz, S. Schleede, Konstantin Khrennikov, Martin Bech, Pierre Thibault, Matthias Heigoldt, F. Pfeiffer, and Stefan Karsch. Quantitative x-ray phase-contrast microtomography from a compact laser-driven betatron source. *Nature communications*, 6:7568, 2015.

[13] T. E. Gureyev, S. C. Mayo, D. E. Myers, Ya. Nesterets, D. M. Paganin, A. Pogany, A. W. Stevenson, and S. W. Wilkins. Refracting Röntgen's rays: propagation-based x-ray phase contrast for biomedical imaging. *Journal of Applied Physics*, 105(10):102005, 2009.

[14] G. Hajdok, J. J. Battista, and I. A. Cunningham. Fundamental x-ray interaction limits in diagnostic imaging detectors: Spatial resolution. *Medical physics*, 35(7):3180–3193, 2008.

[15] M. D. Tabak, S. W. Ing, and M. E. Scharfe. Operation and performance of amorphous selenium-based photoreceptors. *IEEE Transactions on Electron Devices*, 20(2):132–139, 1973.

[16] J. W. Boag. Xeroradiography. *Physics in Medicine & Biology*, 18(1):3, 1973.

[17] Wei Zhao, W. G. Ji, Anne Debrie, and J. A. Rowlands. Imaging performance of amorphous selenium based flat-panel detectors for digital mammography: Characterization of a small area prototype detector. *Medical physics*, 30(2):254–263, 2003.

[18] John A. Rowlands, Wei Zhao, Ira M. Blevis, David F. Waechter, and Zhongshou Huang. Flat-panel digital radiology with amorphous selenium and active-matrix readout. *RadioGraphics*, 17(3):753–760, 1997.

[19] Safa Kasap, Joel B. Frey, George Belev, Olivier Tousignant, Habib Mani, Jonathan Greenspan, Luc Laperriere, Oleksandr Bubon, Alla Reznik, Giovanni DeCrescenzo, et al. Amorphous and polycrystalline photoconductors for direct conversion flat panel x-ray image sensors. *Sensors*, 11(5):5112–5157, 2011.

[20] Karim S. Karim, Arokia Nathan, and John Alan Rowlands. Amorphous silicon active pixel sensor readout circuit for digital imaging. *IEEE transactions on electron devices*, 50(1):200–208, 2003.

[21] W. Que and J. A. Rowlands. X-ray imaging using amorphous selenium: Inherent spatial resolution. *Medical physics*, 22(4):365–374, 1995.

[22] Christopher C. Scott, Shiva Abbaszadeh, Sina Ghanbarzadeh, Gary Allan, Michael Farrier, Ian A. Cunningham, and Karim S Karim. Amorphous selenium direct detection CMOS digital x-ray imager with 25 micron pixel pitch. In *Medical Imaging 2014: Physics of Medical Imaging*, volume 9033, page 90331G. International Society for Optics and Photonics, 2014.

[23] Alireza Parsafar, Christopher C. Scott, Abdallah El-Falou, Peter M. Levine, and Karim S. Karim. Direct-conversion CMOS x-ray imager with 5.6 μm $\times$ 6.25 μm pixels. *IEEE Electron Device Letters*, 36(5):481–483, 2015.

[24] Christopher C. Scott, Alireza Parsafar, Aabdollah El-Falou, Peter M. Levine, and Karim S. Karim. High dose efficiency, ultra-high resolution amorphous selenium/CMOS hybrid digital x-ray imager. In *Electron Devices Meeting (IEDM), 2015 IEEE International*, pages 30–6. IEEE, 2015.

[25] Rodney Shaw. The equivalent quantum efficiency of the photographic process. *The Journal of Photographic Science*, 11(4):199–204, 1963.

[26] Majid Rabbani, Rodney Shaw, and Richard Van Metter. Detective quantum efficiency of imaging systems with amplifying and scattering mechanisms. *Journal of the Optical Society of America A*, 4(5):895–901, 1987.

[27] Ian A. Cunningham and Rodney Shaw. Signal-to-noise optimization of medical imaging systems. *Journal of the Optical Society of America A*, 16(3):621–632, 1999.

[28] John Boone, Ian Cunningham, James Dobbins, John Yorkston, John Rowlands, Martin Yaffe, David Pickens, Aaron Fenster, Donal Downey, and David Goodenough. *Handbook of Medical Imaging: Volume 1. Physics and Psychophysics*. SPIE press, Bellingham, 2000.

[29] Wei Zhao and J. A. Rowlands. Digital radiology using active matrix readout of amorphous selenium: Theoretical analysis of detective quantum efficiency. *Medical Physics*, 24(12):1819–1833, 1997.

[30] G. Hajdok, J. Yao, J. J. Battista, and I. A. Cunningham. Signal and noise transfer properties of photoelectric interactions in diagnostic x-ray imaging detectors. *Medical physics*, 33(10):3601–3620, 2006.

[31] Alberto Bravin, Paola Coan, and Pekka Suortti. X-ray phase-contrast imaging: from pre-clinical applications towards clinics. *Physics in Medicine & Biology*, 58(1):R1, 2012.

[32] Sheridan C. Mayo, Andrew W. Stevenson, and Stephen W. Wilkins. In-line phase-contrast x-ray imaging and tomography for materials science. *Materials*, 5(5):937–965, 2012.

[33] Jens Als-Nielsen and Des McMorrow. *Elements of modern X-ray physics*. John Wiley & Sons, 2011.

[34] Joseph W Goodman. *Introduction to Fourier optics*. Roberts and Company Publishers, 2005.

[35] Ian A. Cunningham and Tomi F. Nano. A toolkit to manipulate x-ray spectra in medical imaging. In Johan Sjoberg, editor, *Clinical Diagnostic and Interventional Radiology Physics with MATLAB: A problem-solving approach*, chapter 16. CRC Press Taylor and Francis Group.

[36] Douglas M. Tucker, Gary T. Barnes, and Dev P. Chakraborty. Semiempirical model for generating tungsten target x-ray spectra. *Medical physics*, 18(2):211–218, 1991.

[37] J. H. Hubbell and S. M. Seltzer. X-ray mass attenuation coefficients. NIST standard reference database 126. [https://dx.doi.org/10.18434/t4d01f]. Technical report, Radiation Physics Division, PML, NIST, 2004.

[38] Godfrey N. Hounsfield. Computerized transverse axial scanning (tomography): Part 1. Description of system. *The British journal of radiology*, 46(552):1016–1022, 1973.

[39] Willard S. Boyle and George E. Smith. Charge coupled semiconductor devices. *Bell System Technical Journal*, 49(4):587–593, 1970.

[40] Wei Zhao and John A. Rowlands. X-ray imaging using amorphous selenium: Feasibility of a flat panel self-scanned detector for digital radiology. *Medical physics*, 22(10):1595–1604, 1995.

[41] C. D. Arvanitis, S. E. Bohndiek, G. Royle, A. Blue, H. X. Liang, A. Clark, M. Prydderch, R. Turchetta, and R. Speller. Empirical electro-optical and x-ray performance evaluation of CMOS active pixels sensor for low dose, high resolution x-ray medical imaging. *Medical Physics*, 34(12):4612–4625, 2007.

[42] Karim Sallaudin Karim. *Pixel architectures for digital imaging using amorphous silicon technology*. PhD thesis, University of Waterloo, 2002.

[43] Albert Rose. The sensitivity performance of the human eye on an absolute scale. *Journal of the Optical Society of America*, 38(2):196–208, 1948.

[44] Albert Rose. Television pickup tubes and the problem of vision. In *Advances in Electronics and Electron Physics*, volume 1, pages 131–166. Elsevier, 1948.

[45] Nicholas Allec. Multilayer energy discriminating detector for medical x-ray imaging applications. 2012.

[46] Athanasios Papoulis. *Probability, random variables, and stochastic processes*. McGraw-Hill, 1965.

[47] Robert K. Swank. Absorption and noise in x-ray phosphors. *Journal of Applied Physics*, 44(9):4199–4203, 1973.

[48] G. Hajdok, J. J. Battista, and I. A. Cunningham. Fundamental x-ray interaction limits in diagnostic imaging detectors: Frequency-dependent Swank noise. *Medical physics*, 35(7Part1):3194–3204, 2008.

[49] Ehsan Samei, Egbert Buhr, Paul Granfors, Dirk Vandenbroucke, and Xiaohui Wang. Comparison of edge analysis techniques for the determination of the MTF of digital radiographic systems. *Physics in Medicine & Biology*, 50(15):3613, 2005.

[50] Junji Morishita, Kunio Doi, Romain Bollen, Philip C. Bunch, Dietmar Hoeschen, Gerard Sirand-rey, and Yoshiharu Sukenobu. Comparison of two methods for accurate measurement of modulation transfer functions of screen-film systems. *Medical Physics*, 22(2):193–200, 1995.

[51] Maryellen Lissak Giger and Kunio Doi. Investigation of basic imaging properties in digital radiography. I. Modulation transfer function. *Medical Physics*, 11(3):287–295, 1984.

[52] Hiroshi Fujita, D.-Y. Tsai, Takumi Itoh, Kunio Doi, Junji Morishita, Katsuhiko Ueda, and Akiyoshi Ohtsuka. A simple method for determining the modulation transfer function in digital radiography. *IEEE Transactions on medical imaging*, 11(1):34–39, 1992.

[53] I. A. Cunningham and B. K. Reid. Signal and noise in modulation transfer function determinations using the slit, wire, and edge techniques. *Medical physics*, 19(4):1037–1044, 1992.

[54] Ehsan Samei, Michael J. Flynn, and David A. Reimann. A method for measuring the presampled MTF of digital radiographic systems using an edge test device. *Medical physics*, 25(1):102–113, 1998.

[55] I. A. Cunningham and A. Fenster. A method for modulation transfer function determination from edge profiles with correction for finite-element differentiation. *Medical physics*, 14(4):533–537, 1987.

[56] J. H. Siewerdsen, A. M. Waese, D. J. Moseley, S. Richard, and D. A. Jaffray. Spektr: A computational tool for x-ray spectral analysis and imaging system optimization. *Medical physics*, 31(11):3057–3067, 2004.

[57] Gavin G. Poludniowski and Philip M. Evans. Calculation of x-ray spectra emerging from an x-ray tube. Part I. Electron penetration characteristics in x-ray targets. *Medical physics*, 34(6):2164–2174, 2007.

[58] Gavin G. Poludniowski. Calculation of x-ray spectra emerging from an x-ray tube. Part II. X-ray production and filtration in x-ray targets. *Medical physics*, 34(6):2175–2186, 2007.

[59] Medical electrical equipment — Characteristics of digital x-ray imaging devices — Part 1-1: Determination of the detective quantum efficiency — Detectors used in radiographic imaging. Standard, International Electrotechnical Commission, Geneva, CH, 2015.

[60] Safa Kasap, Joel B. Frey, George Belev, Olivier Tousignant, Habib Mani, Luc Laperriere, Alla Reznik, and John A. Rowlands. Amorphous selenium and its alloys from early xeroradiography to high resolution x-ray image detectors and ultrasensitive imaging tubes. *Physica status solidi (b)*, 246(8):1794–1805, 2009.

[61] S. O. Kasap, M. Zahangir Kabir, and J. A. Rowlands. Recent advances in x-ray photoconductors for direct conversion x-ray image detectors. *Current Applied Physics*, 6(3):288–292, 2006.

[62] Satoshi Tokuda, Hiroyuki Kishihara, Susumu Adachi, and Toshiyuki Sato. Preparation and characterization of polycrystalline CdZnTe films for large-area, high-sensitivity x-ray detectors. *Journal of Materials Science: Materials in Electronics*, 15(1):1–8, 2004.

[63] K. S. Shah, R. A. Street, Y. Dmitriyev, P. Bennett, L. Cirignano, M. Klugerman, M. R. Squillante, and G. Entine. X-ray imaging with PbI_2-based a-Si:H flat panel detectors. *Nuclear Instruments and Methods in Physics Research Section A: Accelerators, Spectrometers, Detectors and Associated Equipment*, 458(1-2):140–147, 2001.

[64] Hong Du, Larry E. Antonuk, Youcef El-Mohri, Qihua Zhao, Zhong Su, Jin Yamamoto, and Yi Wang. Investigation of the signal behavior at diagnostic energies of prototype, direct detection, active matrix, flat-panel imagers incorporating polycrystalline HgI_2. *Physics in Medicine & Biology*, 53(5):1325, 2008.

[65] R. A. Street, S. E. Ready, K. Van Schuylenbergh, J. Ho, J. B. Boyce, P. Nylen, K. Shah, L. Melekhov, and H. Hermon. Comparison of PbI_2 and HgI_2 for direct detection active matrix x-ray image sensors. *Journal of Applied Physics*, 91(5):3345–3355, 2002.

[66] M. Schieber, H. Hermon, A. Zuck, A. Vilensky, L. Melekhov, R. Shatunovsky, E. Meerson, Y. Saado, M. Lukach, E. Pinkhasy, et al. Thick films of x-ray polycrystalline mercuric iodide detectors. *Journal of Crystal Growth*, 225(2-4):118–123, 2001.

[67] Mohammad Zahangir Kabir. *Modeling of x-ray photoconductors for x-ray image detectors*. PhD thesis, University of Saskatchewan, 2005.

[68] M. J. Berger, J. H. Hubbell, S. M. Seltzer, J. Chang, J. S. Coursey, R. Sukumar, D. S. Zucker, and K. Olsen. XCOM: Photon cross sections database. NIST standard reference database 8 (XGAM). [https://dx.doi.org/10.18434/t48g6x]. Technical report, Radiation Physics Division, PML, NIST, 2010.

[69] W. Que and J. A. Rowlands. X-ray photogeneration in amorphous selenium: Geminate versus columnar recombination. *Physical review. B, Condensed matter*, 51(16):10500, 1995.

[70] C. Haugen, S. O. Kasap, and J. Rowlands. Charge transport and electron-hole-pair creation energy in stabilized a-se x-ray photoconductors. *Journal of Physics D: Applied Physics*, 32(3):200, 1999.

[71] George Belev and Safa O. Kasap. Amorphous selenium as an x-ray photoconductor. *Journal of non-crystalline solids*, 345:484–488, 2004.

[72] S. A. Mahmood, M. Z. Kabir, O. Tousignant, H. Mani, J. Greenspan, and P. Botka. Dark current in multilayer amorphous selenium x-ray imaging detectors. *Applied Physics Letters*, 92(22):223506, 2008.

[73] Robert E. Johanson, S. O. Kasap, J. Rowlands, and B. Polischuk. Metallic electrical contacts to stabilized amorphous selenium for use in x-ray image detectors. *Journal of non-crystalline solids*, 227:1359–1362, 1998.

[74] Bo Zhao and Wei Zhao. Temporal performance of amorphous selenium mammography detectors. *Medical physics*, 32(1):128–136, 2005.

[75] Shiva Abbaszadeh, Nicholas Allec, Sina Ghanbarzadeh, Umar Shafique, and Karim S. Karim. Investigation of hole-blocking contacts for high-conversion-gain amorphous selenium detectors for x-ray imaging. *IEEE transactions on Electron devices*, 59(9):2403–2409, 2012.

[76] Ian A. Cunningham. Linear-systems modeling of parallel cascaded stochastic processes: the NPS of radiographic screens with reabsorption of characteristic x-radiation. In *Medical Imaging 1998: Physics of Medical Imaging*, volume 3336, pages 220–231. International Society for Optics and Photonics, 1998.

[77] M. Zahangir Kabir, Mahmudur W. Rahman, and W. Y. Shen. Modelling of detective quantum efficiency of direct conversion x-ray imaging detectors incorporating charge carrier trapping and K-fluorescence. *IET circuits, devices & systems*, 5(3):222–231, 2011.

[78] J. H. Siewerdsen, L. E. Antonuk, Y. El-Mohri, J. Yorkston, W. Huang, J. M. Boudry, and I. A. Cunningham. Empirical and theoretical investigation of the noise performance of indirect detection, active matrix flat-panel imagers (AMFPIs) for diagnostic radiology. *Medical physics*, 24(1):71–89, 1997.

[79] Amit Jain, D. R. Bednarek, Ciprian Ionita, and S. Rudin. A theoretical and experimental evaluation of the microangiographic fluoroscope: A high-resolution region-of-interest x-ray imager. *Medical physics*, 38(7):4112–4126, 2011.

[80] Heang-Ping Chan and Kunio Doi. Energy and angular dependence of x-ray absorption and its effect on radiographic response in screen-film systems. *Physics in Medicine & Biology*, 28(5):565, 1983.

[81] D. R. Dance and G. J. Day. Escape probabilities for fluorescent x-rays. *Physics in Medicine & Biology*, 30(3):259, 1985.

[82] Safa O. Kasap and John A. Rowlands. Review x-ray photoconductors and stabilized a-se for direct conversion digital flat-panel x-ray image-detectors. *Journal of materials science: materials in electronics*, 11(3):179–198, 2000.

[83] G. Zentai, L. Partain, M. Richmond, K. Ogusu, and S. Yamada. 50 μm pixel size a-Se mammography imager with high DQE and increased temperature resistance. In *Medical Imaging 2010: Physics of Medical Imaging*, volume 7622, page 762215. International Society for Optics and Photonics, 2010.

[84] Tomoaki Masuzawa, Ichitaro Saito, Takatoshi Yamada, Masanori Onishi, Hisato Yamaguchi, Yu Suzuki, Kousuke Oonuki, Nanako Kato, Shuichi Ogawa, Yuji Takakuwa, et al. Development of an amorphous selenium-based photodetector driven by a diamond cold cathode. *Sensors*, 13(10):13744–13778, 2013.

[85] Shiva Abbaszadeh. *Indirect conversion amorphous selenium photodetectors for medical imaging applications*. PhD thesis, University of Waterloo, 2014.

[86] M. Zahangir Kabir and S. O. Kasap. Modulation transfer function of photoconductive x-ray image detectors: effects of charge carrier trapping. *Journal of Physics D: Applied Physics*, 36(19):2352, 2003.

[87] Shiva Abbaszadeh, Christopher C. Scott, Oleksandr Bubon, Alla Reznik, and Karim S. Karim. Enhanced detection efficiency of direct conversion x-ray detector using polyimide as hole-blocking layer. *Scientific reports*, 3:3360, 2013.

[88] David M. Hunter, Gueorgi Belev, Giovanni DeCrescenzo, Safa O. Kasap, James G. Mainprize, J. A. Rowlands, Charles Smith, Tümay Tümer, Vladimir Verpakhovski, Shi Yin, et al. The dependence of the modulation transfer function on the blocking layer thickness in amorphous selenium x-ray detectors. *Medical physics*, 34(8):3358–3373, 2007.

[89] G. P. Lindberg, R. E. Tallman, S. Abbaszadeh, K. S. Karim, J. A. Rowlands, A. Reznik, and B. A. Weinstein. Frustration of photocrystallization in amorphous selenium films and film-polymer structures near the glass transition. In *AIP Conference Proceedings*, volume 1566, pages 19–20. AIP, 2013.

[90] Shiva Abbaszadeh, K. Rom, O. Bubon, B. A. Weinstein, K. S. Karim, J. A. Rowlands, and A. Reznik. The effect of the substrate on transient photodarkening in stabilized amorphous selenium. *Journal of Non-Crystalline Solids*, 358(17):2389–2392, 2012.

[91] Alireza Parsafar. Design and implementation of a high resolution CMOS x-ray imager with amorphous selenium sensor. Master's thesis, University of Waterloo, 2015.

[92] P. Spanne, C. Raven, I. Snigireva, and A. Snigirev. In-line holography and phase-contrast microtomography with high energy x-rays. *Physics in Medicine & Biology*, 44(3):741, 1999.

[93] David Paganin, S. C. Mayo, Tim E. Gureyev, Peter R. Miller, and Steve W. Wilkins. Simultaneous phase and amplitude extraction from a single defocused image of a homogeneous object. *Journal of microscopy*, 206(1):33–40, 2002.

[94] B. D. Arhatari and A. G. Peele. Optimisation of phase imaging geometry. *Optics express*, 18(23):23727–23739, 2010.

[95] Jeffrey H. Siewerdsen and David A. Jaffray. Optimization of x-ray imaging geometry (with specific application to flat-panel cone-beam computed tomography). *Medical physics*, 27(8):1903–1914, 2000.

[96] Martin Krenkel, Mareike Töpperwien, Christian Dullin, Frauke Alves, and Tim Salditt. Propagation-based phase-contrast tomography for high-resolution lung imaging with laboratory sources. *AIP Advances*, 6(3):035007, 2016.

[97] Daniel H. Larsson, William Vågberg, Andre Yaroshenko, Ali Önder Yildirim, and Hans M. Hertz. High-resolution short-exposure small-animal laboratory x-ray phase-contrast tomography. *Scientific reports*, 6:39074, 2016.

[98] Matthias Bartels, Victor H. Hernandez, Martin Krenkel, Tobias Moser, and Tim Salditt. Phase contrast tomography of the mouse cochlea at microfocus x-ray sources. *Applied Physics Letters*, 103(8):083703, 2013.

[99] Alberto Mittone, Ilja Manakov, Ludovic Broche, Christophe Jarnias, Paola Coan, and Alberto Bravin. Characterization of a sCMOS-based high-resolution imaging system. *Journal of synchrotron radiation*, 24(6):1226–1236, 2017.

[100] Massimo Marenzana, Charlotte K. Hagen, Patricia Das Neves Borges, Marco Endrizzi, Magdalena B. Szafraniec, Konstantin Ignatyev, and Alessandro Olivo. Visualization of small lesions in rat cartilage by means of laboratory-based x-ray phase contrast imaging. *Physics in Medicine & Biology*, 57(24):8173, 2012.

[101] P. Das Neves Borges, A. E. Forte, T. L. Vincent, D. Dini, and M. Marenzana. Rapid, automated imaging of mouse articular cartilage by microCT for early detection of osteoarthritis and finite element modelling of joint mechanics. *Osteoarthritis and cartilage*, 22(10):1419–1428, 2014.

[102] Anterolateral aspect of right knee. [https://en.wikipedia.org/wiki/knee]. Technical report, Wikipedia, 2019.

[103] Rodney A. Brooks and Giovanni Di Chiro. Theory of image reconstruction in computed tomography. *Radiology*, 117(3):561–572, 1975.

[104] C. T. Badea, M. Drangova, David W. Holdsworth, and G. A. Johnson. In vivo small-animal imaging using micro-CT and digital subtraction angiography. *Physics in Medicine & Biology*, 53(19):R319, 2008.

[105] David W. Holdsworth and Michael M. Thornton. Micro-CT in small animal and specimen imaging. *Trends in Biotechnology*, 20(8):S34–S39, 2002.

[106] Andrew L. Goertzen, Vivek Nagarkar, Robert A. Street, Michael J. Paulus, John M. Boone, and Simon R. Cherry. A comparison of x-ray detectors for mouse CT imaging. *Physics in Medicine & Biology*, 49(23):5251, 2004.

[107] Wei Zhao, Giovanni DeCrescenzo, and John A Rowlands. Investigation of lag and ghosting in amorphous selenium flat-panel x-ray detectors. In *Medical Imaging 2002: Physics of Medical Imaging*, volume 4682, pages 9–21. International Society for Optics and Photonics, 2002.

[108] A. H. Goldan, O Tousignant, L. Laperrière, and K. S. Karim. Reduced photocurrent lag using unipolar solid-state photoconductive detector structures: Application to stabilized n-i-p amorphous selenium. *Applied Physics Letters*, 96(5):053507, 2010.

[109] Anna Burvall, Ulf Lundström, Per A. C. Takman, Daniel H. Larsson, and Hans M. Hertz. Phase retrieval in x-ray phase-contrast imaging suitable for tomography. *Optics express*, 19(11):10359–10376, 2011.